Tungsten (2024) 6:77–113
https://doi.org/10.1007/s42864-023-00229-x

Tungsten
www.springer.com/42864

REVIEW PAPER

Photocatalytic applications and modification methods of two-dimensional nanomaterials: a review

Fan Yang[1,2] · **Ping Hu**[1,2] · **Fan Yang**[1,2] · **Xing-Jiang Hua**[1,2] · **Bo Chen**[1,2] · **Lili Gao**[1] · **Kuai-She Wang**[1,2]

Received: 7 February 2023 / Revised: 7 April 2023 / Accepted: 18 April 2023 / Published online: 1 July 2023

Abstract

Due to its unique electronic structure and special size effect, two-dimensional (2D) nanomaterials have shown great potential far beyond bulk materials in the field of photocatalysis. How to deeply explore the photocatalytic mechanism of 2D nanomaterials and design more efficient 2D semiconductor photocatalysts are research hotspots. This review provides a comprehensive introduction to typical 2D nanomaterials and discusses their current application status in the field of photocatalysis. The effects of material properties such as band structure, morphology, crystal face structure, crystal structure and surface defects on the photocatalytic process are discussed. The main modification methods are highlighted, including doping, noble metal deposition, heterojunction, thickness adjustment, defect engineering, and dye sensitization in 2D material systems. Finally, the future development of 2D nanomaterials is prospected. It is hoped that this paper can provide systematic and useful information for researchers engaged in the field of photocatalysis.

Keywords Photocatalysis · Two-dimensional · Nanomaterials · Bandgap · Modification strategy

1 Introduction

With the development of science and technology, environmental pollution and energy shortage have become two major concerns of human beings. As a mild reaction, nontoxic, and reusable technology, photocatalysis can efficiently convert solar energy into chemical energy, and is considered to be one of the most forward-looking long-term solutions to global energy and environmental problems [1, 2].

As a promising technology, photocatalysis has been widely used in water treatment [3–5], hydrogen production by water splitting [6–8], CO_2 reduction [9, 10], nitrogen fixation [11, 12], and organic synthesis [13, 14] (Fig. 1). Fujishima and Honda published a paper on TiO_2 photoelectrochemical cells in 1972, showing that water can be decomposed into oxygen and hydrogen by visible light without any external voltage [15]. Since then, photocatalytic has come into public attention. In 1976, Carey et al. found that in the photocatalytic process of TiO_2, polychlorinated biphenyl, haloalkane, etc. can be effectively photocatalytically degraded [16]. This has led to the realization that photocatalysis can provide new approaches for environmental governance. Schrauzer and Guth determined that water splitting does not require external energy except for light energy in 1977, and demonstrated that TiO_2 can split water to generate H_2 under ultraviolet (UV) light irradiation [17]. Nearly, 50 years of researches have also proved that photocatalytic technology can be effectively applied in environmental governance and energy conversion and has great development potential. Even studies have shown that photocatalysis can degrade almost all organic pollutants in water [18].

The principle of semiconductor photocatalyst is shown in Fig. 2: the energy band structure of semiconductor materials consists of a low-level valence band (VB) filled with electrons and a high-level conduction band (CB) that is not filled with electrons, and a gap called the forbidden band is

---

Author 1: Yang Fan is currently studying for a master's degree in Xi'an University of Architecture and Technology; Author 3: Yang Fan is currently working as a postdoctoral researcher in Xi'an University of Architecture and Technology.

✉ Ping Hu
huping@xauat.edu.cn

✉ Fan Yang
yangfan1990@xauat.edu.cn

[1] School of Metallurgy Engineering, Xi'an University of Architecture and Technology, Xi'an 710055, China

[2] National and Local Joint Engineering Research Center for Functional Materials Processing, Xi'an University of Architecture and Technology, Xi'an 710055, China

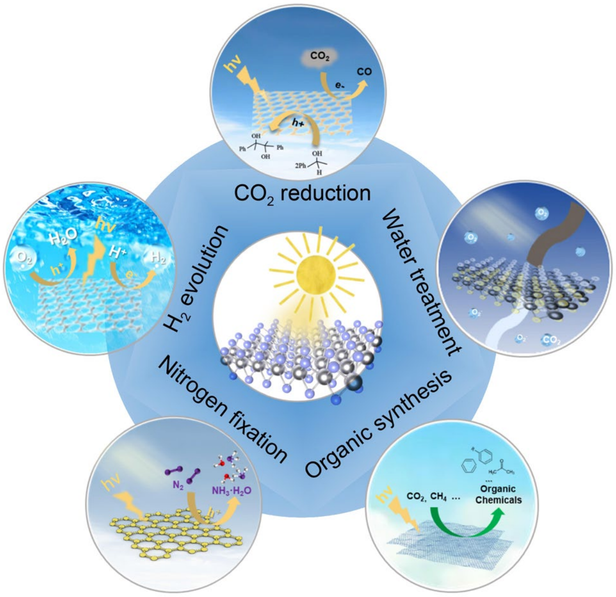

Fig. 1 Application areas of photocatalytic technology

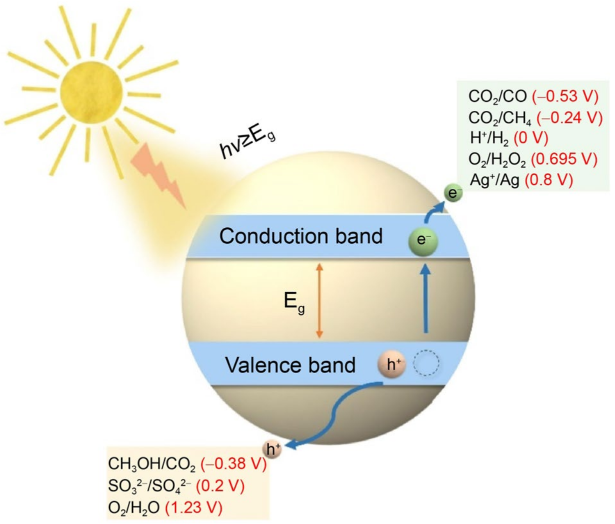

Fig. 2 Schematic diagram of photocatalytic schematic

located between the conduction band minimum (CBM) and valence band maximum (VBM). When the photocatalyst is irradiated by light with energy greater than or equal to the forbidden band width, the electrons in the VB absorb energy and transition to the CB, leaving holes in the VB, eventually forming "electron–hole pairs", also known as "carriers". Under the action of the space electric field, the electron–hole pairs partially migrate to the particle surface and participate in further catalytic reactions [19].

As the first semiconductor material to be applied to photocatalysis, TiO_2 is a wide-bandgap semiconductor (3–3.2 eV), which can only absorb UV light with a wavelength less than 387 nm. UV light only accounts for 5% of sunlight, making TiO_2 less efficient for sunlight. This makes TiO_2 less than ideal in practice. At the same time, in the photocatalytic process, the high electron–hole pair recombination rate and low quantum efficiency also limit the photocatalytic activity of TiO_2 [20]. Hoffmann et al. studied TiO_2 in depth, and found that four processes are very important in the photocatalytic process: first, the spectral response range; second, whether the photogenerated electron holes can be effectively separated; the third is the speed at which electrons are transferred from the interior of an atom to the surface; the fourth is the strength of redox activity [21]. In order to better participate in the above four processes, the selection of semiconductor photocatalysts is the key to photocatalytic applications. High-efficiency photocatalysts must have a suitable bandgap to provide sufficient redox activity, excellent electron–hole separation ability, and visible-light response characteristics.

Aiming at these four key steps to improve the photocatalytic efficiency, two-dimensional (2D) nanomaterials have entered people's field of vision as new photocatalysts. As shown in Fig. 3, carbon materials are used as an example to show different material structures from zero-dimensional (0D) to three-dimensional (3D) [22–25]. 2D nanomaterials refer to materials in which electrons can only move freely (plane movement) on the nano scale (1–100 nm) in two dimensions. Because of its unique thickness size and 2D structure characteristics, the intrinsic properties of the materials can be enhanced, resulting in many different properties from their corresponding 3D structures. For example, large specific surface area, porous surface with abundant reactive sites, good carrier mobility, good Young's modulus, excellent electrical and thermal conductivity, and the advantages of easily forming new composite structures with other materials [26]. Meanwhile, this 2D structure can be assembled through spin processes or layer-by-layer, and layered artificial structures are created and designed on demand, with high flexibility in material design [27].

However, the practical application of 2D nanomaterials is still limited due to the easy agglomeration of powders, the small scale of preparation, and the uncontrollability. At the same time, too narrow or too wide bandgap of a single 2D nanomaterials will lead to problems such as insufficient redox capacity, narrow photoresponse range, and fast recombination of electron–hole pairs, resulting in poor photocatalytic performance. On this basis, scientists have further researched, proposed a variety of modification methods to improve the photocatalytic efficiency of 2D nanomaterials, and revealed their mechanisms. Due to the important position of 2D materials in the field of photocatalysis, some researchers have reviewed in detail the basic properties of

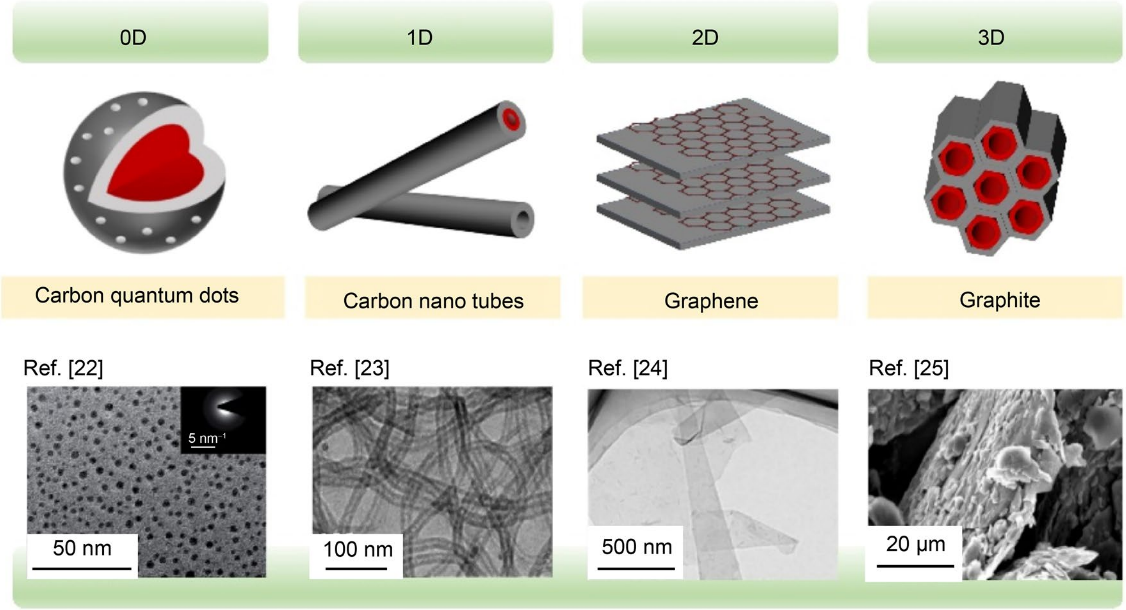

Fig. 3 Schematic diagram of material dimensions. Reproduced with permission from Ref. [22]. Copyright 2018, Royal Society of Chemistry. Reproduced with permission from Ref. [23]. Copyright 2020, Elsevier. Reproduced with permission from Ref. [24]. Copyright 2017, ACS Publications. Reproduced with permission from Ref. [25]. Copyright 2020, Elsevier

2D materials, the synthesis strategies of 2D materials, and the surface modification of 2D materials in recent years, providing many interesting perspectives [28–33].

Compared with previous reviews [28–33], in this review, we introduce the progress of various typical 2D materials in the field of photocatalysis in a more comprehensive and detailed manner. Unlike other reviews, which often explore the advantages of 2D materials in the field of photocatalysis from the perspective of photocatalytic processes such as light absorption, charge separation and transfer, this review discusses the influence of intrinsic characteristics of 2D materials (bandgap, morphology, facet structure, crystal structure and defects) on the photocatalytic process, revealing the advantages of 2D systems in photocatalysis. Afterwards, various modification methods (element doping, noble metal deposition, heterojunction, thickness tuning, defect engineering, and dye sensitization) are further discussed on the basis of the above-mentioned influencing factors. Finally, this review summarizes and looks forward to the main difficulties and potential solutions in the current 2D materials research, looking forward to helping readers think about the ideas of photocatalyst design.

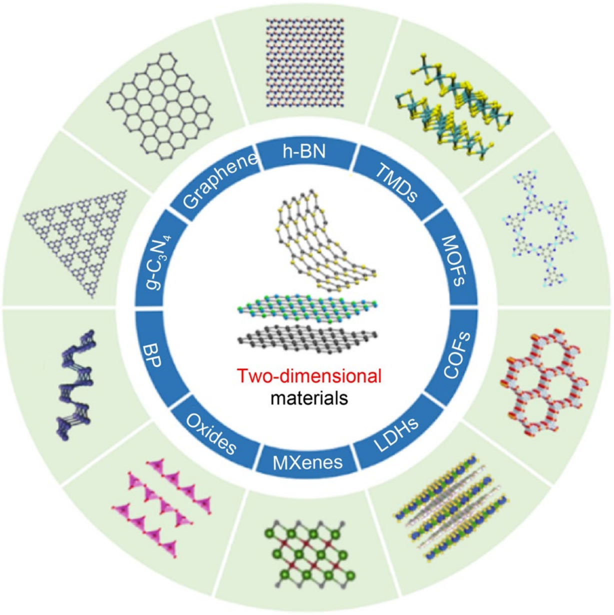

Fig. 4 Common 2D materials and their structures (COFs: covalent organic frameworks)

2 Typical 2D nanomaterials

Typical 2D nanomaterials are shown in Fig. 4, which can be mainly divided into two aspects. One is graphene and its derivatives, the other is graphene-like 2D materials, such as 2D metal oxides [34, 35], hexagonal boron nitride (h-BN) [36, 37], transition metal dichalcogenides (TMDs) [38], carbonitrides [39, 40], black phosphorus (BP) [41], layered double hydroxides (LDHs) [42], 2D metal organic frameworks (MOFs) [43] and other layered materials with unique physical and chemical properties. In this section, we introduce the structure, properties, synthesis process and research progress of these materials, in order to help readers better understand the 2D material system.

2.1 Graphene and its derivatives

Since graphene was prepared by micromechanical exfoliation method [44] in 2004, it has attracted wide attention in the field of photocatalysis due to its outstanding mechanical, thermal, optical properties and appearance characteristics [45]. With the deepening of research, some new methods for preparing graphene have been proposed, such as mechanical exfoliation method, liquid phase exfoliation method (LPE), redox method, chemical vapor deposition method (CVD), and electrochemical exfoliation method. Among them, the exfoliation preparation process represented by the mechanical exfoliation method can obtain high-quality graphene, but it also has the disadvantages of small area and low yield. Although the synthesis process represented by CVD method can prepare large-area graphene, the defects generated during the growth process reduce the performance of graphene. How to combine the advantages of CVD and mechanical exfoliation is the main idea for large-scale preparation of high-quality, large-area graphene [46].

The basic structure of graphene is a honeycomb-shaped planar film formed by sp^2 hybridization of carbon atoms, and its derivatives are graphene oxide (GO) and reduced graphene oxide (rGO). Due to its zero bandgap, graphene has excellent electrical conductivity, and has a wide spectral absorption range, including visible light and long-wave infrared, even to terahertz frequencies. At the same time, the special single-atom-layer planar structure enables it to have a high light transmittance (~97.7%), which can be combined with other catalysts without affecting the light absorption capacity of the photocatalyst. The theoretical specific surface area of graphene is as high as 2,630 $m^2 \cdot g^{-1}$, which can provide more redox active sites [47]. However, the zero bandgap of graphene also makes its redox reaction ability poor, which is not conducive to the photocatalytic reaction. Therefore, researchers often combine it with other wide-bandgap photocatalytic materials to form composites with excellent photocatalytic properties, thereby exerting the excellent optoelectronic properties of graphene. Zhang et al. prepared graphene/ZnO composites (GR/ZnO) by ball milling and LPE [48]. The bandgap test results show that the bandgap of the GR/ZnO is narrowed to 3.10 eV compared with pure ZnO. Under simulated sunlight irradiation, GR/ZnO exhibited significantly enhanced photocatalytic activity, which was 6 times higher than that of pure ZnO (Fig. 5). This study shows that the addition of graphene can effectively narrow the bandgap and improve the photocatalytic performance. Huang et al. composited flake $BiFeO_3$ with graphene via a simple hydrothermal method. The composite material has excellent visible-light response, and the photocatalytic performance is greatly improved [49]. Zhang et al. prepared MoS_2/N-doped graphene composites, which constituted a Z-scheme photocatalytic system composed by two narrow-bandgap semiconductors [50]. Its transformed bandgap extends the photoresponse to 1,550 nm, enabling

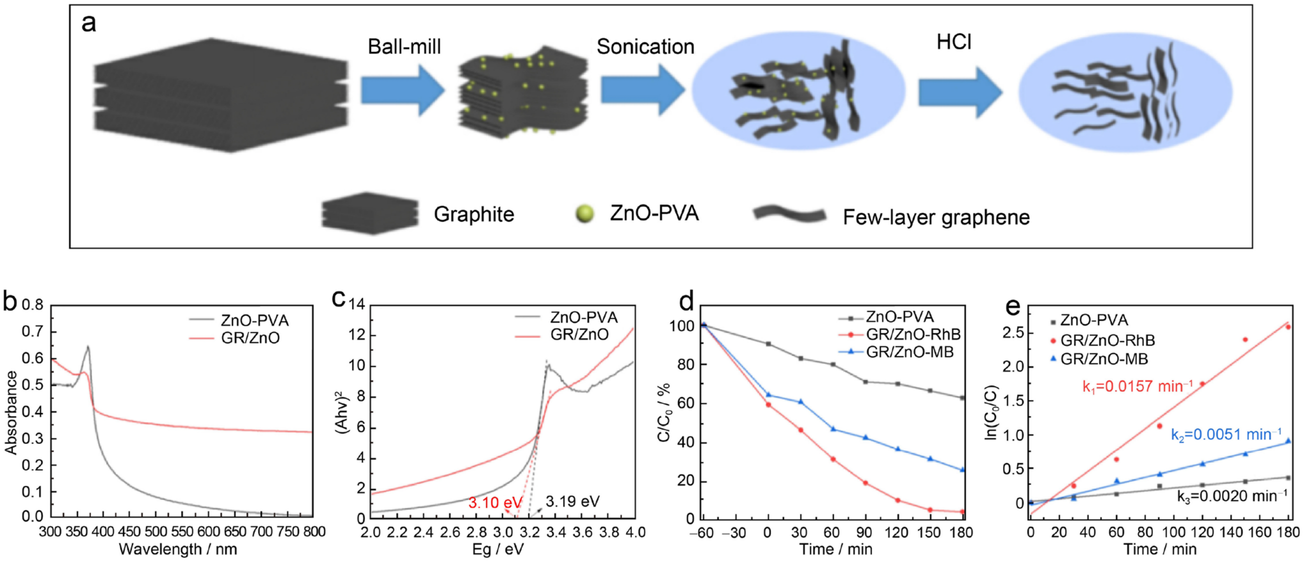

Fig. 5 **a** Schematic diagram of the preparation of GR/ZnO. **b** Ultraviolet–visible absorption spectra (UV–Vis absorption spectra) of ZnO–Polyvinyl alcohol (PVA) and GR/ZnO. **c** Light energy relationship diagram of ZnO–PVA and GR/ZnO. **d** Rate diagram of degradation of methylene blue (MB) and rhodamine B (RhB) by GR/ZnO under simulated sunlight, and **e** pseudo-first order kinetic curve. Reproduced with permission from Ref. [48].Copyright 2021, Elsevier

the composite to effectively degrade NH_3 under near-infrared irradiation. Although graphene can hardly be applied to photocatalysis independently due to the zero bandgap, Yang et al. found that coating a single layer of graphene on a metal co-catalyst can form a photocatalyst that can be applied to photocatalytic overall water splitting (POWS) [51]. Studies have shown that graphene plays an important role in suppressing the reverse action of H_2 and O_2. Importantly, among various types of graphene, γ-graphene (GY) is regarded as the graphene with the highest stability and semiconducting properties. It has a suitable optical bandgap (2.3 eV) and can be well applied in the field of photocatalysis [52]. Wu et al. prepared $TiO_2/MoSe_2$/GY ternary nanocomposites. GY acts as an electron collector and hole transfer channel, effectively separating photogenerated carriers [53].

More studies have shown that functionalized graphene-based analogs, such as GO, may be potential materials for photocatalysts, because the band structure of GO is related to its oxidation degree, its bandgap can be regulated during the preparation process [54, 55]. Yeh et al. used the modified Hummers method to prepare GO with a bandgap of 2.4–4.3 eV, and the results showed that it can be used as a photocatalytic catalyst for water splitting [56]. Under ultraviolet or visible-light irradiation, 20% Methanol aqueous solution and pure water can stably generate H_2.

2.2 Graphene-like 2D materials

Graphene-like 2D materials are a general term for 2D single-layer or few-layer structural materials. There are many types of graphene-like materials, which exhibit superior surface properties compared with bulk materials due to their unique layered structure.

2.2.1 Metal oxides

In the past 4 decades, many metal oxides such as TiO_2 [57, 58], ZnO [59, 60], SnO_2 [61, 62], WO_3 [63, 64], and Fe_2O_3 [65, 66] have been extensively studied as photocatalysts. Due to the obvious advantages of 2D materials in the field of photocatalysis compared with bulk materials, the research of metal oxide nanosheets is also widely carried out. Taking TiO_2 as an example, the preparation methods of metal oxide nanomaterials mainly include CVD, sol–gel method, hydrothermal method, pulse laser deposition method (PLD) and sputtering method. Among them, the hydrothermal method is the most common method for preparing 2D TiO_2 nanosheets, and PLD and laser sputtering method are commonly used to prepare thinner TiO_2 films. Other methods are commonly used to prepare lower dimensional forms such as TiO_2 nanorods and nanospheres. It is notable that by controlling the reaction temperature during CVD, different states of TiO_2 from nanotubes to thin films can be obtained [67].

The 2D nanosheets of TiO_2 are exfoliated from layered titanates and exhibit similar semiconductor properties to rutile and anatase TiO_2. However, due to the reduced grain size, the bandgap of TiO_2 nanosheets is slightly larger (~ 3.8 eV), which is larger than that of anatase TiO_2 (~ 3.2 eV). This will lead to a decrease in the photoresponse range, which is not conducive to the photocatalytic reaction [68]. Studies have shown that photocatalytic performance of TiO_2 nanosheets can be further improved by modifying it by doping or carrying a narrow-bandgap photocatalyst. Such as Liu et al. prepared transition metal modified TiO_2 nanosheets by microwave-assisted hydrothermal method [69]. It is revealed that the addition of transition metals effectively narrows the bandgap of TiO_2 (Fig. 6a). Through UV–Vis absorption spectra, it can be seen that TiO_2 with transition metals has better visible-light absorption than pure TiO_2 (Fig. 6b). The results of photoluminescence spectra (PL spectra) (Fig. 6c) show that the addition of transition metals reduces the intensity of TiO_2, especially Cu/TiO_2. The decrease in intensity indicates faster carrier transfer, which corresponds to the optimal photocatalytic nitrogen fixation performance of Cu/TiO_2. Chen et al. prepared TiO_2 nanosheets/NiO nanorods composites by a hydrothermal method (Fig. 6d) [58]. TiO_2/NiO photocatalyst showed good MB degradation activity and hydrogen production efficiency under visible light, which were 12 times and 10 times that of TiO_2 nanosheets. This is due to the construction of its p–n heterojunctions, which enhances interfacial charge transfer and light absorption (Fig. 6e). At present, TiO_2-based nanocomposites have been studied in many fields such as sewage treatment, medical treatment, hydrogen energy, and CO_2 reduction. It is worth pointing out that in the field of anti-cancer, TiO_2 will have great potential due to its good biocompatibility and low toxicity.

In addition to TiO_2, the nanoscale research on other traditional metal oxide catalysts has also achieved success. Wang et al. prepared oxygen-rich vacancy-defective ZnO nanosheets with tunable Brunauer–Emmett–Teller (BET) surface area [70]. The analysis showed that the oxygen-rich vacancies enhanced the visible-light absorption of the ZnO nanosheets, and the increase in the surface oxygen vacancy concentration was positively correlated with the BET surface area. Compared with ZnO with fewer oxygen defects, the rate of RhB degradation by oxygen-enriched ZnO under visible light is increased by about 11 times. Zhang et al. prepared MnO_2/Fe_3O_4 nanocomposites [71]. The results show that the MnO_2/Fe_3O_4 nanocomposite exhibits excellent photocatalytic performance and high stability when degrading MB under UV–Vis light (Fig. 6f, g). In addition to the light factor, the photocatalytic performance of MnO_2/Fe_3O_4 also varied with pH, which was due to the different surface charge states at different pH

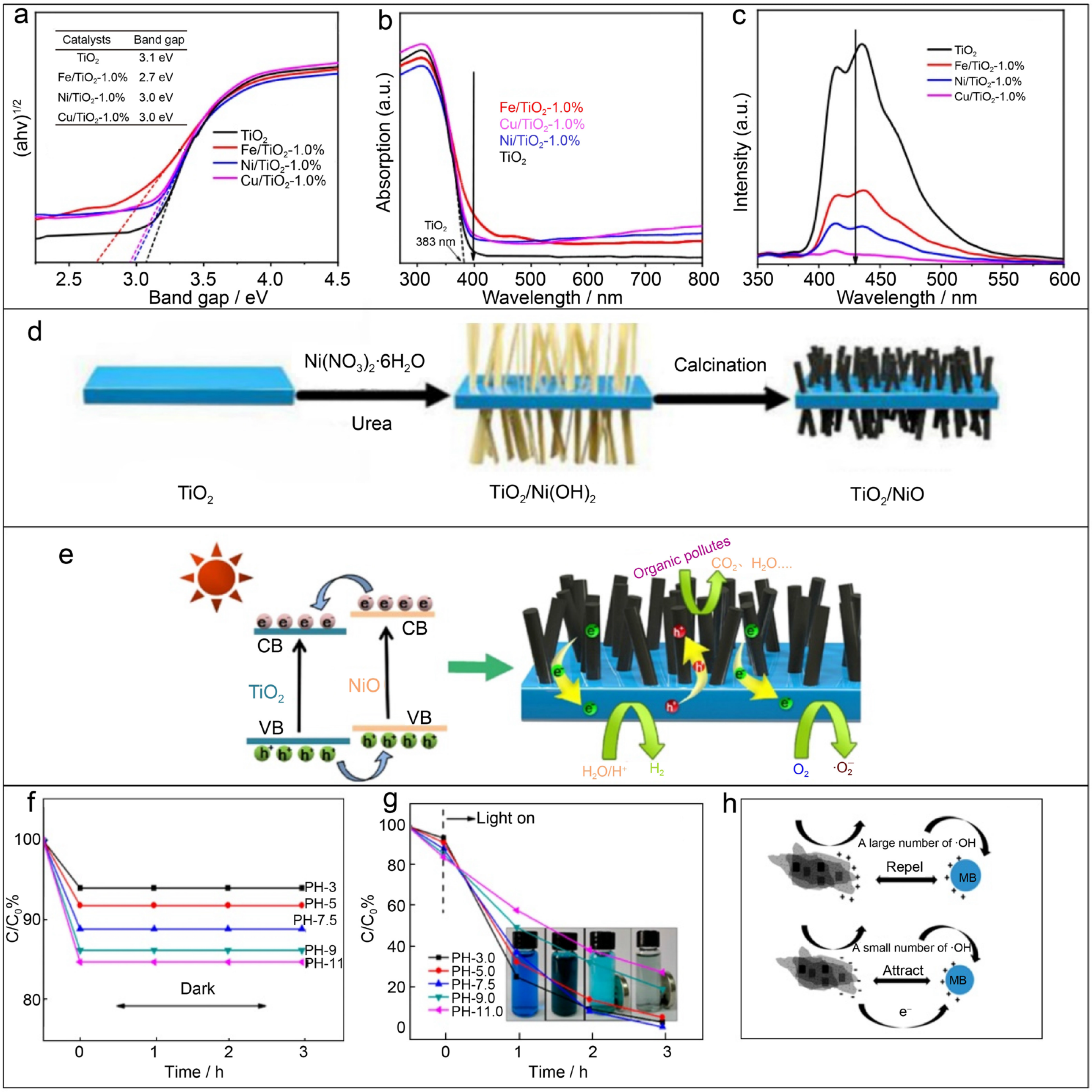

Fig. 6 **a** UV–Vis absorption spectra of transition metal modified TiO_2 nanosheets. **b** The bandgap evaluation of transition metal modified TiO_2 nanosheets. **c** PL spectra of transition metal modified TiO_2 nanosheets. Reproduced with permission from Ref. [69]. Copyright 2020, Royal Society of Chemistry. **d** The schematic diagram of the synthesis processes of TiO_2/NiO. **e** The schematic diagram of the photocatalytic mechanism of TiO_2/NiO. Reproduced with permission from Ref. [58] Copyright 2020, Elsevier. Degradation curves of MB by MnO_2/Fe_3O_4 at different pH values **f** in the dark and **g** with UV–Vis light, **h** the speculated reaction principle of MnO_2/Fe_3O_4 and MB under different pH values. Reproduced with permission from Ref. [71]. Copyright 2014, ACS Publications

(Fig. 6h). In addition, tests have shown that the MnO_2/Fe_3O_4 nanocomposite is ferromagnetic and can be effectively separated by an external magnetic field, enabling reuse and being more environmentally friendly.

2.2.2 h-BN

h-BN is a graphene-like hexagonal structure formed by covalently connecting N atoms and B atoms in equal proportions. It has a honeycomb lattice structure similar to graphene, so it is called “white graphite” and has excellent physical properties and surface atomic flatness [72, 73]. Since h-BN is an insulator with a bandgap of 6 eV and lacks dangling bonds on the surface, h-BN was studied as an ideal substrate and insulating layer for other 2D materials in the early stages of research [74]. As the research progressed, it was found that the bandgap of h-BN is very sensitive to size, thickness and defects. Meanwhile, h-BN has a high specific surface area and excellent conductivity [75]. Moreover, although h-BN is an insulator, its (002) crystal plane has abundant active sites, which can effectively participate in the photocatalytic process [76]. The above advantages have led researchers to explore the application of h-BN in photocatalysis. Currently, the mainstream methods for preparing h-BN include mechanical exfoliation, solvothermal, CVD, and molecular beam epitaxy (MBE). Due to the advantages of high quality and large scale, CVD has become the main preparation method of h-BN. At the same time, CVD also has excellent performance for the preparation of h-BN heterostructures [77].

In practical photocatalytic applications, due to the wide bandgap of h-BN, it is necessary to modify h-BN by defect engineering, doping or building a heterojunction structure to realize its application in the field of catalysis [78–80]. It is found that combining wide-bandgap h-BN with zero-bandgap graphene into an in-plane heterostructure is an effective approach to design efficient photocatalysts. Bevilacqua et al. used density functional theory (DFT) to study the stability and optical properties of monolayer h-BN when doped with graphene [81]. The results show that graphene (h-BNC) doped with wide-bandgap h-BN nanodomains exhibits a non-zero gap, and the width of its bandgap is related to the number of BN nanodomains. Therefore, by doping h-BN with graphene, the h-BNC that can respond to visible light can be obtained, which is a promising photocatalytic material. Besides graphene, h-BN can also be combined with other 2D materials to form photocatalysts. Li et al. constructed TiO_2/h-BN composite photocatalysts with TiO_2 nanosheets and h-BN nanosheets by a solvothermal method. The photocatalyst has greatly improved the degradation efficiency of rhodamine B, which is 6.9 times that of commercial TiO_2 [82]. Wang et al. prepared a composite photocatalyst of h-BN and g-C_3N_4 quantum dots. Due to the large specific surface area and good electron-harvesting properties of h-BN, h-BN/g-C_3N_4 has excellent photocatalytic performance [83].

2.2.3 Transitional metal dichalcogenides (TMDs)

TMDs are compounds composed of transition metal elements and chalcogen elements (S, Se or Te). The basic expression of TMDs is MX_2, where M is a transition metal and X is a chalcogen (Fig. 7a). The layers of TMDs are connected by weak van der Waals forces, which can be easily peeled from the bulk phase to a single sheet [38]. As Fig. 7b shows, depending on the coordination of elements and the stacking order of the lamellae, TMDs can form a variety of crystalline polytypes: 1T, 2H, and 1T’ [84], exhibiting different electronic properties from metals to semiconductors [85, 86]. TMDs exhibit excellent electronic, optical, and physicochemical properties, which mainly have the advantages of high electrical conductivity, narrow bandgap, abundant active sites, abundant earth reserves, and low cost [87–89]. At the same time, it is found that the theoretical catalytic performance of TMDs is second only to the noble metal Pt and some transition metals, which has great research value [90, 91].

Most TMDs materials have typical bandgap tunable properties, such as MoS_2 [92], $MoSe_2$ [93], WSe_2 [94] and WS_2 [95]. According to DFT, as shown in Fig. 7c, the band structure of 2H-MoS_2 will evolve as it decreases from bulk layer to monolayer [96]. As the thickness decreases, the positions of VB and CB change, from an indirect bandgap semiconductor to a direct bandgap semiconductor. The difference between the two bandgaps is shown in Fig. 7d [97]. At present, the main methods for preparing 2D TMDs include mechanical exfoliation, LPE, CVD, and wet chemical synthesis. The above traditional methods have been widely used in the preparation of various TMDs materials. Yang et al. reviewed the preparation methods of TMDs materials in detail [84]. It is noteworthy that the electrochemical Li-ion intercalation method has been creatively proposed in recent years. This method can produce atomically thin TMDs nanosheets on a large scale and with high yield, and has been widely applied to the preparation of various TMDs materials [98].

As the most representative material among TMDs materials, MoS_2 is a hexagonal layered crystal structure, and each unit is a “sandwich” structure of S-Mo-S. The common crystal forms are 1T, 2H and 3R, of which the 2H crystal form is the most stable. Although some studies have revealed that the metal phase 1T-MoS_2 exhibits better photocatalytic performance, the research on 2H-MoS_2 catalysts is still the mainstream due to the requirement of stability in practical applications [99–101]. The bandgap of bulk MoS_2 is too small, only 1.2 eV, which cannot provide sufficient oxidation/reduction potential to activate the photocatalytic process. The single-layer MoS_2, due to the conversion of indirect bandgap to direct bandgap, has an increased forbidden band width to about 1.96 eV, which can be used as a photocatalyst [102, 103]. However, due to its still narrow bandgap, the oxidizing ability is weaker when used alone. The edge potentials of the CB and VB of MoS_2 are higher than those of most photosensitive semiconductors, and the potential difference between the CB of MoS_2 and other semiconductor materials can promote the transfer of

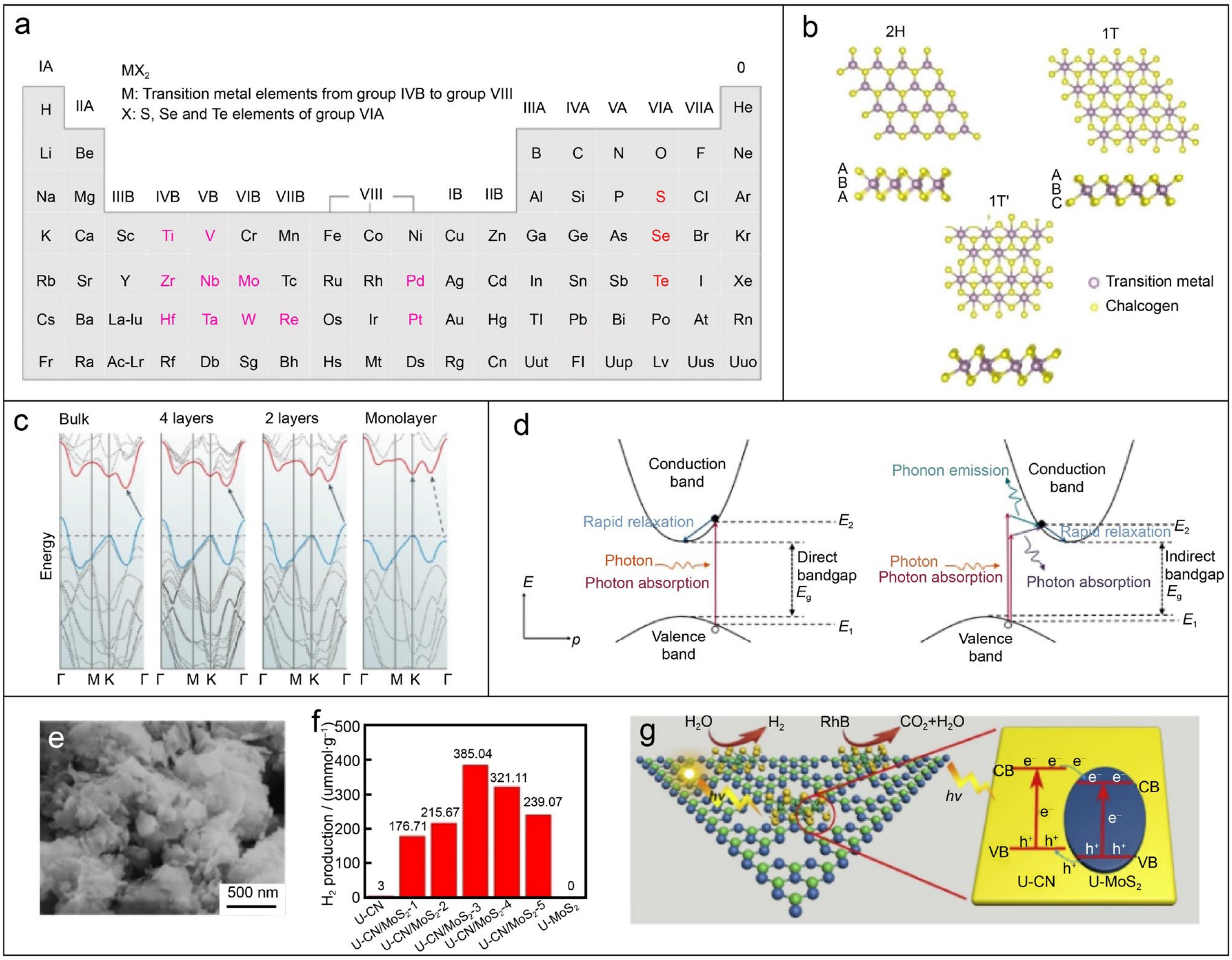

Fig. 7 **a** Composition of TMDs. **b** Schematic models of different phases of TMDs. Reproduced with permission from Ref. [84]. Copyright 2023, John Wiley and Sons. **c** Evolution of the band structure of 2H-MoS_2 calculated for samples of decreasing thickness. Reproduced with permission from Ref. [96]. Copyright 2017, Springer Nature. **d** Schematic diagram of direct band gap and indirect band gap. Reproduced with permission from Ref. [97]. Copyright 2020, ACS Publications. **e** Scanning electron microscope image of U-CN/MoS_2-3. **f** Histograms of hydrogen production for different ratios of U-CN/MoS_2. **g** Heterojunction mechanism of U-CN/MoS_2 photocatalyst. Reproduced with permission from Ref. [106]. Copyright 2019, Elsevier

electrons to MoS_2, thereby effectively separating the carriers. At the same time, MoS_2 can be used as a substitute for noble metals in the hydrogen evolution reaction and become a co-catalyst for the hydrogen evolution reaction [104, 105]. Therefore, MoS_2 is generally used as a co-catalyst or carrying other semiconductor photocatalytic materials to form a heterojunction to improve the photocatalytic performance. Li et al. prepared ultrathin C_3N_4/MoS_2 heterojunction photocatalysts (U-CN/MoS_2) [106]. The results show that the photocatalyst activity is significantly improved after MoS_2 is supported on C_3N_4 to form a heterojunction (Fig. 7e). The best photocatalytic hydrogen production efficiency can reach 385.04 μmol·h^{-1}·g^{-1} (Fig. 7f). The photocatalytic mechanism of U-CN/MoS_2 is shown in Fig. 7g. When U-CN/MoS_2 is illuminated, the electrons on VB of both materials are excited to CB. Under the action of the heterojunction, the electrons on the CB of U-CN are transferred to the CB of MoS_2, and the holes on the VB of MoS_2 are transferred to the VB of U-CN at the same time. This process realizes the effective separation of electrons and holes, which promotes the improvement of photocatalytic activity.

In addition to MoS_2, other TMDs materials have also shown excellent performance in the field of photocatalysis. Kou et al. grew TiO_2 on $MoSe_2$ nanosheets [107]. Under visible light, the hydrogen production rate of $MoSe_2$/TiO_2 is much higher than that of pure $MoSe_2$ and TiO_2. The study shows that the increase in the hydrogen production rate is attributed to the $MoSe_2$ promoting the absorption of visible light and the high charge separation efficiency of the $MoSe_2$/TiO_2 interface. Zhang et al. synthesized WSe_2 nanosheets with a thickness of 0.7 nm by a colloidal method [108]. The results show that the synthesized WSe_2 nanosheets can efficiently catalyze the aerobic coupling reaction of amines and imines under visible-light irradiation, verifying the possibility of TMDs being applied in various catalytic processes.

2.2.4 Graphitic carbon nitride (g-C_3N_4)

As a semiconductor material, the catalytic hydrogen evolution performance of g-C_3N_4 was not discovered until 2008 by Wang et al. and it is the first non-metal organic semiconductor photocatalytic material with visible-light response in the field of photocatalysis with a suitable bandgap (2.7 eV) [109]. Since bulk g-C_3N_4 is formed by stacking 2D structures, g-C_3N_4 nanosheets can be obtained by exfoliating bulk g-C_3N_4. Studies have shown that the photocatalytic performance of g-C_3N_4 nanosheets is significantly improved compared with that of bulk g-C_3N_4, and are only composed of C and N elements, which will not cause metal pollution and are environmentally friendly [110]. The main methods for preparing bulk g-C_3N_4 include thermal polycondensation, hydrothermal method, template method and ball milling method. Among them, the preparation of g-C_3N_4 by thermal polycondensation of nitrogen-rich precursors is the most commonly used [111]. However, g-C_3N_4 prepared by this method is rich in defects due to incomplete deamination during calcination. Relatively speaking, the template method can effectively regulate the structural characteristics such as porosity and specific surface area of g-C_3N_4 through appropriate templates. However, the residual template will have a great impact on the photocatalytic performance of g-C_3N_4, and it also has a more cumbersome process. In response to the above problems, the researchers considered improving the structural defects by pretreatment of the nitrogen-rich precursor before calcination. If the precursor is treated with acid, the van der Waals force between the layers is weakened, which is beneficial to obtain thinner g-C_3N_4 sheets [112].

The photocatalytic activity of pure-phase g-C_3N_4 still needs to be improved due to the limitations of low quantum rate, fast recombination of photogenerated carriers, and insufficient response to visible light above 460 nm [113]. Generally, the photocatalytic activity of g-C_3N_4 can be enhanced by modification methods such as doping, noble metal deposition, and construction of heterojunctions. Peng et al. synthesized a ternary composite photocatalyst CdS/Au/g-C_3N_4 [114]. Due to the deposition of CdS and Au on the surface of g-C_3N_4, two different structures, CdS–g-C_3N_4 and CdS@Au-g-C_3N_4, were formed (Fig. 8a, b). Meanwhile, there is a strong interaction between the three components, so compared with the binary composites CdS/g-C_3N_4, Au/g-C_3N_4 and pure g-C_3N_4, the photocatalytic activity of CdS/Au/g-C_3N_4 for RhB degradation was significantly enhanced under visible-light irradiation. Zhang et al. prepared Mn-adsorbed g-C_3N_4 [115]. The change in electronic structure caused by the stable bond between Mn and N atoms makes the photocatalytic performance of Mn-adsorbed g-C_3N_4 three times that of pristine g-C_3N_4. Cao et al. introduced nitrogen vacancies (NVs) into n-type g-C_3N_4 to construct a p-n heterojunction, which significantly improved the photocatalytic degradation activity of g-C_3N_4 [116]. Introducing appropriate functional groups into the g-C_3N_4 framework is also an effective strategy to enhance the photocatalytic activity. Wang et al. designed a simple KOH-assisted sealing heating process to tune the electronic structure of g-C_3N_4 [117]. The introduction of cyano groups increases the charge carrier density of g-C_3N_4, reduces the surface transfer resistance, promotes charge separation and transfer, and improves the photocatalytic hydrogen production performance.

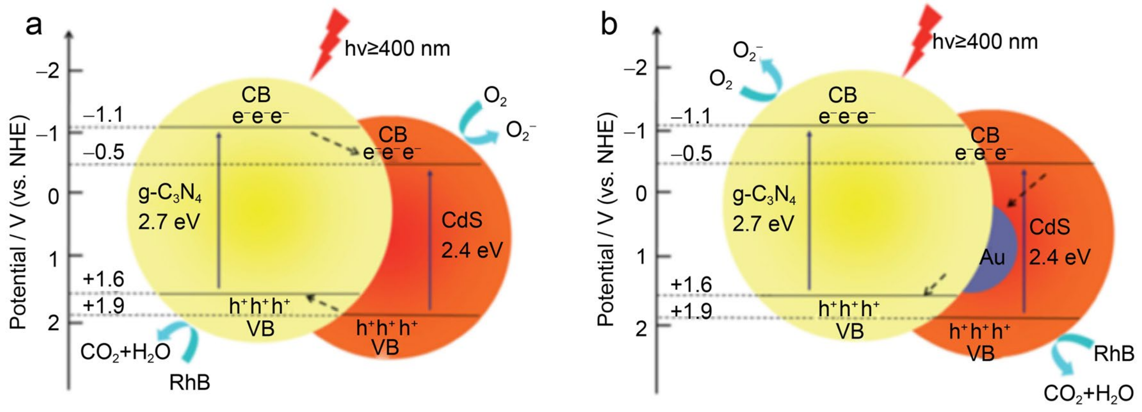

Fig. 8 **a** CdS–g-C_3N_4 heterojunction. **b** CdS@Au–g-C_3N_4 heterojunction. Reproduced with permission from Ref. [114]. Copyright 2016, Royal Society of Chemistry

2.2.5 2D elemental material

2D elemental materials include 2D main group elements and 2D transition metals. In the field of catalysis, BP is one of the most concerned 2D elemental materials. BP is an allotrope of phosphorus with a monolayer pleated honeycomb structure. It was first extracted from white phosphorus in 1,914 under high pressure and moderate temperature (200 ℃), showing high density and good conductivity [118]. However, the high-pressure conditions of this method limit the development of this method. In 2007, a simple method for preparing BP by catalyzing red phosphorus was proposed, which further promoted the practical application of BP [119]. The current mainstream methods for preparing BP mainly include "top-down" methods such as mechanical exfoliation, LPE, and electrochemical exfoliation. BP is highly sensitive to substrates, so the "bottom-up" preparation of BP remains a challenge [120]. BP nanosheets have a flexible and tunable bandgap (0.3–2.0 eV), which increases with the decrease of the number of layers, 2D ultrathin structure and large specific surface area. These features can enhance the adsorption of photocatalysts, increase the number of active sites, and effectively improve the catalytic performance [121, 122]. At present, the latest research published in Nature has revealed a significant change in the shape of the VB of BP when it receives light radiation, which will provide a solid theoretical basis for its further application in many fields such as catalysis [123]. The narrow bandgap of BP enables it to absorb a large amount of visible light and even near-infrared light, but at the same time, it does not have enough driving force to participate in the photoreaction. Another limitation of BP is that it is unstable in the atmospheric environment, and usually requires the deposition of a coating on the surface to improve its stability [124]. Although monolayer BP has excellent theoretical photocatalytic activity, few experiments have proved the photocatalytic performance of pure BP, and researchers often combine it with other materials. It was not until 2017 that Zhu et al. prepared BP nanosheets with a size of 300–500 nm by ball milling [125]. The hydrogen evolution rate was 512 $\mu mol \cdot h^{-1} \cdot g^{-1}$, which was superior to g-C_3N_4.

In addition to BP, bismuth (Bi), a group V element, is also a popular element 2D material, which has the characteristics of metal and semiconductor. Bi-based semiconductor photocatalysts have been widely used in the field of catalysis due to their unique electronic, optical, magnetic, and structural properties. Unlike metal oxides such as TiO_2, the VB of Bi is formed by the hybridization of Bi 6*s* and O 2*p* orbitals, which effectively shortens the semiconductor band gap and is more conducive to the absorption of visible light [28]. At present, researchers have synthesized many Bi-based photocatalysts, such as bismuth oxide (Bi_2O_3), bismuth oxyhalide ($Bi_aO_bX_c$, where X = Cl, Br or I), and Bi-based polymetallic salts ($BiVO_4$, Bi_2WO_6, and Bi_2MoO_6, etc.). By adjusting the parameters to prepare Bi-based photocatalysts with ultrathin structures, materials with more excellent photocatalytic properties will be obtained. Its main preparation methods include exfoliation, solvothermal, colloidal synthesis, and CVD growth [126].

In addition to 2D Bi-based materials, the bismuthene exfoliated from bulk bismuth also has excellent 2D ultrathin structures. However, due to the diamond structure of bulk Bi, the layers may not be completely connected by weak van der Waals force, so it is difficult to prepare bismuthene by traditional mechanical exfoliation and ultrasonic exfoliation. Generally, it is prepared by other methods such as high-temperature hydrothermal and LPE [127]. Yu et al. successfully prepared Bi-nanobelts (~ 20 nm) through high-temperature hydrothermal synthesis [128]. Yang et al. designed a method for preparing bismuthene by sulfuric acid intercalation exfoliation, and finally successfully exfoliated bulk Bi into thin bismuthene materials [129]. Hussain et al. used a simple mechanical route to successfully prepare Bi-nanosheets (~ 2 nm) on highly polished silicon substrates by hot pressing [130]. Sun et al. prepared bismuthene nanosheets by LPE. They ground crystalline Bi for 5 h, then dispersed and centrifuged, and finally successfully prepared bismuthene nanosheets with a thickness of about 4 nm [131].

2.2.6 MOFs and covalent organic frameworks (COFs)

MOFs are a class of 2D materials composed of metal ions or metal clusters and organic ligand molecules. Due to their tunable metal centers and functionalizable ligands, MOFs can have diverse basic building blocks, monodisperse metal sites and organic ligands, and thus can form crystal structures with different space groups. At the same time, MOFs also have a periodic arrangement structure, a precisely controlled pore structure, and a high specific surface area. Compared with bulk materials, 2D MOFs nanosheets have more unsaturated coordination bonds and active centers, and have better catalytic performance [132, 133]. Due to the variability of the crystal structure of 2D MOFs, the electronic structure of MOFs can be adjusted by the construction of vacancies, which can cause atomic arrangement distortion, charge density redistribution, and generate a large number of active sites. Zou et al. constructed MOFs with abundant vacancies by pyrolyzing specific functional groups [134]. The results showed that the MOFs maintained the framework structure and more active sites were exposed. The electronic structure is optimized to facilitate the uniform formation of site angles along the defect interface. After fusion of metal phosphides with defective MOFs, they exhibit low overpotentials and long-term oxygen evolution reaction (OER) stability. The excellent electrochemical performance is mainly attributed to vacancies, which enlarge the electrochemically active surface area and accelerate the charge-transfer rate. On the other hand, due to their functionalizable ligands, MOFs can also improve light absorption properties by introducing large conjugated ligands, dual ligands and other ligand engineering methods. Degaga et al. investigated the structure–property relationship of pristine and functionalized zinc benzene-1,3,5-tricarboxylate (Zn-BTC) MOFs using DFT [135]. Figure 9a shows different Zn-BTC MOFs unit-cells constituted from the coordinatively saturated and unsaturated secondary building unit (SBU) and the organic linker BTC for pristine, amino-functionalized (–NH_2), and cyano-functionalized (–CN) MOFs. Density of state (DOS) calculations revealed the variation of VBM and CBM of the Zn-BTC constituted from the coordinatively unsaturated SBU（Zn-BTCU）and their relative relationship with the Fermi level (Fig. 9b). Figure 9c shows the relative positions of VBM and CBM of pristine and functionalized Zn-BTCU MOFs. It is not difficult to see, the –NH_2 can lead to an upward shift of the band edge, and the –CN leads to a shift of the band edge in the opposite direction, which narrows the bandgap and tunes the light absorption properties. This variation is due to the inhomogeneous distribution of N 2*p* and C 2*p* states at the band edge introduced by functionalizations.

Notably, not all MOFs are suitable for photocatalytic water splitting. MOFs suitable for photocatalytic decomposition should satisfy three requirements: (1) low bandgap energy and suitable band edges, (2) water-stability, and (3) high conjugation backbone [136]. Meanwhile, the stability

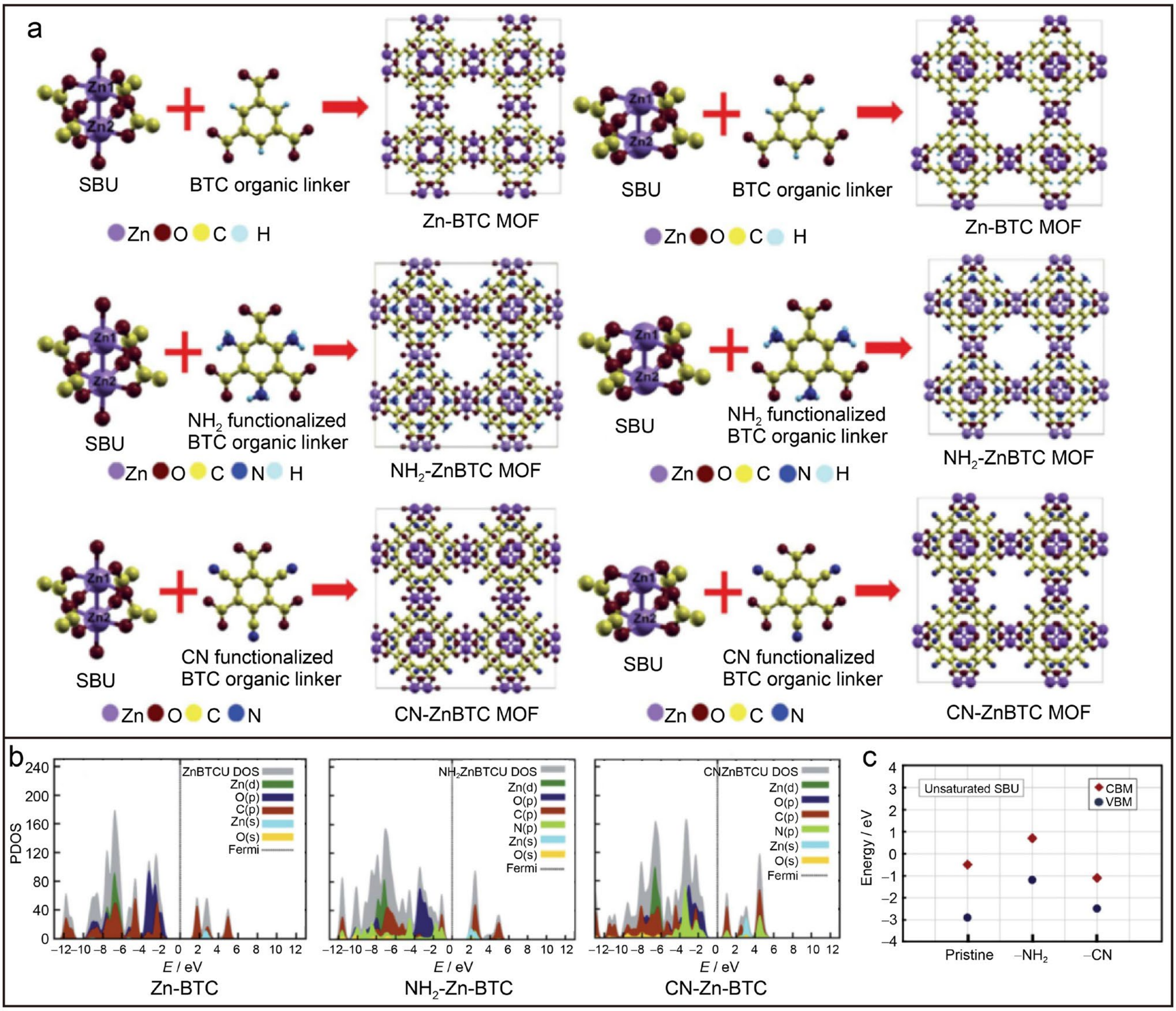

Fig. 9 **a** Multiple structures of Zn-BTC ($Zn_3(BTC)_2$) MOFs combined with different ligands. **b** DOS calculation of Zn-BTCU MOFs with unsaturated SBU. **c** Relative positions of the VBM and CBM of pristine and functionalized Zn-BTCU MOFs. (PDOS: partial density of states) Reproduced with permission from Ref. [135]. Copyright 2019, Royal Society of Chemistry

of MOFs in practical applications is related to the bonding strength between metal clusters and organic ligands. At present, the mainstream MOFs materials used in the field of photocatalysis are: Zeolitic imidazolate framework -67 (ZIF-67) [137, 138], Materials of Institut Lavoisier -125 (MIL-125) [139, 140], University of Oslo -66 (UIO-66) [141, 142], etc.

Since MOFs have strict requirements on the reaction environment, COFs have been proposed as their alternative materials. COFs are porous crystalline materials composed of organic units composed of light elements (C, N, B, etc.) covalently linked. They have the same low density and high specific surface area and are easy to functionalize as MOFs [143]. The design principle of COFs is to use covalent or non-covalent bonds to integrate structural units to form an extended structure in the internal space of the material. Since covalent bonds can be designed in advance, COFs have the conditions for directional design of pore structures, and various functional groups such as alkyl, phenyl, fullerene, acid, amine, organic groups can be integrated into the pore structure of COFs, thereby realizing rich functional applications [144]. Fuerte-Diez et al. prepared novel covalent triazine frameworks (CTFs) containing phenyl-extended naphthalene units [145]. This metal-free heterogeneous photocatalyst exhibits high chemical stability for selective aerobic oxidation and dehydrogenation cross-coupling reactions of sulfides under visible-light irradiation.

2.2.7 LDHs

LDHs, also known as hydrotalcite-like compounds, are a kind of 2D nanomaterials with a chemical composition of $[\mathrm{M}^{2}_{1-x}\mathrm{M}^{3+}_{x}(\mathrm{OH})_2]^{x+}(\mathrm{A}^{n-})_{x/n}\cdot m\mathrm{H_2O}$, where M^{2+} and M^{3+} represent divalent and trivalent metal cations, respectively (such as Mg^{2+} and Al^{3+} and transition metal elements, Fe^{2+}, Co^{2+}, Ni^{2+}, Zn^{2+}, Cr^{3+}, Fe^{3+}, etc.), and A^{n-} represent interlayer anions(such as $\mathrm{NO_3}^{-}$, $\mathrm{CO_3}^{2-}$ and $\mathrm{SO_4}^{2-}$) [146, 147]. The structures of LDHs are shown in Fig. 10. Due to the diversity of cations and interlayer anions, LDHs have large interlayer spacing, so they are easy to exfoliate, and easy to combine with other materials to achieve specific functional designs. LDHs can be produced naturally or synthesized in the laboratory. At present, the main methods for preparing LDHs include co-precipitation, urea hydrolysis, ion exchange, hydrothermal and electrodeposition. The co-precipitation method is the most important preparation method of LDHs. By adjusting the pH values, temperature, solution concentration and precipitation time during the precipitation process, the control of the nucleation process of LDH materials can be realized [148]. The hydrothermal method is also often used in the preparation of LDHs materials. Compared with the co-precipitation method, the synthesized LDHs have the advantages of large area, good crystallinity, uniform shape and fine particles [149]. At the same time, the LDHs prepared by the hydrothermal method have a narrower bandgap (~ 2.6 eV) and structural advantages, which can be better used in photocatalysis [150].

At present, LDHs have shown great potential in the fields of supercapacitors, secondary batteries and catalysis. By regulating the M^{2+} and M^{3+} cations, the energy bandgap of LDHs ranges from 2.0 to 3.4 eV, which can improve the absorption of visible light, and generally does not introduce additional carrier recombination centers. The chemical composition of the inorganic compound layer and the intercalation layer of LDHs is highly tunable, which can effectively control the position of the catalytic active site, the activation mode of the photocatalytic reaction and the product selectivity. With the decrease of the number of LDHs layers, the thickness decreases continuously, which shortens the migration paths of photogenerated electrons and holes, and can effectively inhibit the recombination of photogenerated electrons and holes [151]. Li et al. briefly introduced the influence of the structural features of LDHs on the photocatalytic process and clarified the flexible and tunable properties of LDHs [152]. Based on the structural tunability of LDHs, researchers have carried out many studies on their

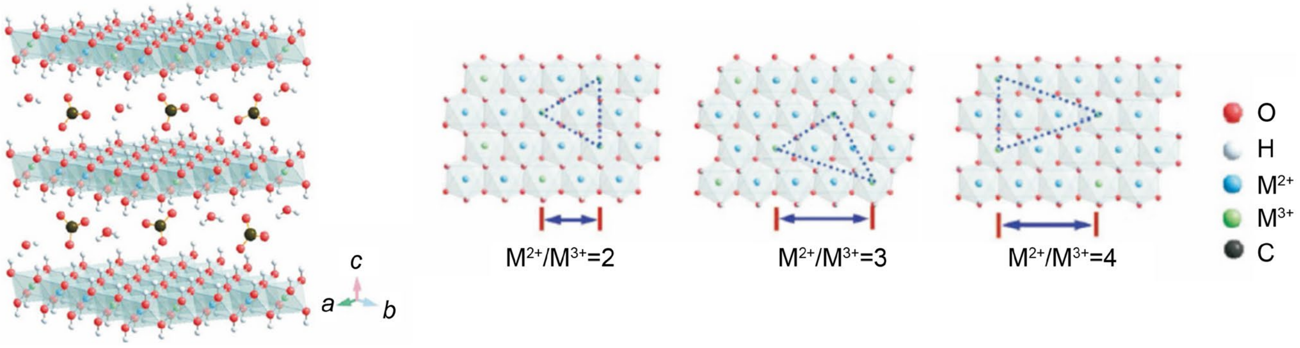

Fig. 10 Schematic diagram of the structure of LDH. Reproduced with permission from Ref. [147]. Copyright 2019, John Wiley and Sons

ion composition. Starukh et al. prepared Zn-Al LDHs [153]. The results show that the photocatalytic activity of Zn-Al-LDHs for MB degradation under UV light originates from the existence of ZnO phase, and the content of ZnO can be adjusted by changing the Zn/Al ratio and heating temperature. Thus, its photocatalytic activity can be regulated. In addition to adjusting the composition of metal ions, Su et al.'s study showed that ZnAl-LDHs with different anions showed different photocatalytic nitrogen reduction activities, which means that the performance of LDHs can also be adjusted by adjusting the interlayer anions [154].

2.2.8 MXenes

MXenes are a new type of ultrathin 2D nanomaterials with great application potential, which contain a large number of transition metal carbides and carbonitrides. MXenes were discovered and synthesized by Gogotsi's group and Barsoum's group in 2011 [155]. Unlike graphene and phosphorene, which have natural 3D precursors of graphite and BP, respectively, MXenes have no direct 3D precursors in nature. In contrast, MXenes multilayer flakes are usually produced by selective removal of the A layer in the MAX phase [156]. The specific process is to use selective etching to etch the A atomic layer in the MAX phase to weaken the bonding between the layers, and then peel off the single-layer nanosheets by intercalation peeling or ultrasonic-assisted liquid phase peeling, and stably dispersed in a specific solvent [157–159]. Since the precursor of this new ultrathin 2D material comes from the MAX phase of the ternary layered ceramic material and exhibits properties similar to graphene, after unifying the names of the MAX phase and graphene, the newly discovered materials are named MXenes [160]. The general formula of the MAX phase is $M_{n+1}AX_n$, where "M" refers to an early transition metal, "A" refers to a main group element, "X" means C or N, and $n = 1–4$. Compared with the single-atom structure of graphene and the metallic bond between C–C, the M and X atoms of MXenes, and the covalent bond between M and X, make MXenes more stable and more diverse than graphene [161]. The general formula of MXenes after removing the A layer is $M_{n+1}X_nT_x$, where T represents the surface functional groups (–O, –OH and –F), and x is the number of surface functional groups. Studies have shown that surface functional groups are related to the electronic state of MXenes. MXenes without functional groups exhibit metallic properties, while it with functional groups exhibit semiconducting properties, making it more widely used [162].

The most widely used preparation method for MXenes is wet chemical etching, and fluorine-containing compounds such as hydrofluoric acid were first used for etching. Later, with the research on fluorine-free etching methods, electrochemical etching methods, alkali etching methods, and molten salt etching methods were also proposed one after another. Generally speaking, the MXenes obtained by etching have a stacked accordion morphology (Fig. 11a), and further intercalation and exfoliation are required to obtain single-layer MXenes [163]. At present, the main peeling methods are ultrasonic exfoliation method, mechanical exfoliation method, intercalation exfoliation method and so on. Wei et al. reviewed the etching methods and layering methods of MXenes, and discussed their advantages and disadvantages [164].

Since its discovery in 2011, researchers have predicted more than 100 possible MXenes compositions through theoretical calculations, of which more than 40 MXenes have been successfully prepared experimentally. As shown in Fig. 11b, in addition to the most studied $M_3X_2T_x$ system, three typical MXenes systems have also been synthesized: M_2XT_x, $M_4X_3T_x$, and $M_5X_4T_x$. Among them, the research based on Ti_3C_2 is the most extensive [165]. The 2D planar topology endows MXenes nanosheets with a large surface area, and its layered structure makes it easy to carry other materials to form nanocomposite photocatalysts, enhance light absorption, and obtain better photocatalytic performance. Since the excellent synergy between TiO_2 and MXenes can effectively improve the electrical conductivity, electron mobility, and carrier separation efficiency of the system, the TiO_2/MXenes system has been extensively studied. Chen et al. synthesized Ti_3C_2/TiO_2 nanosheets with HF as auxiliary agent [166]. The Schottky barrier at the interface of Ti_3C_2/TiO_2 effectively hinders the electron backflow of TiO_2 (Fig. 11c). At the same time, the (001) crystal face of TiO_2 with higher catalytic activity is exposed by using HF as an auxiliary agent, which improves the photocatalytic activity of Ti_3C_2/TiO_2 nanosheets. Ti_3C_2/TiO_2 composite photocatalysts can also be successfully prepared by *in-situ* oxidation or self-assembly [167, 168]. In addition to composites with TiO_2, MXenes materials have also been extensively studied in other composite systems. Zuo et al. prepared layered 2D-Bi_2MoO_6@2D-MXene nanocomposites [169]. The photocatalytic activity of the composites for water splitting is 7.9 times higher than that of pristine Bi_2MoO_6. The analysis showed that there are two reasons for the enhanced photocatalytic activity. On the one hand, the composite structure inhibits the agglomeration of Bi_2MoO_6 nanosheets and increases its specific surface area, and on the other hand, the formed Schottky heterojunction can promote charge transport and hinder carrier recombination (Fig. 11d). Liu et al. successfully prepared a 2D/2D Schottky junction of Ti_3C_2/g-C_3N_4 by ultrasonic irradiation, which accelerated the charge separation [170]. g-C_3N_4 loaded with Ti_3C_2 exhibited excellent photocatalytic activity in nitrogen fixation, CO_2 reduction and degradation.

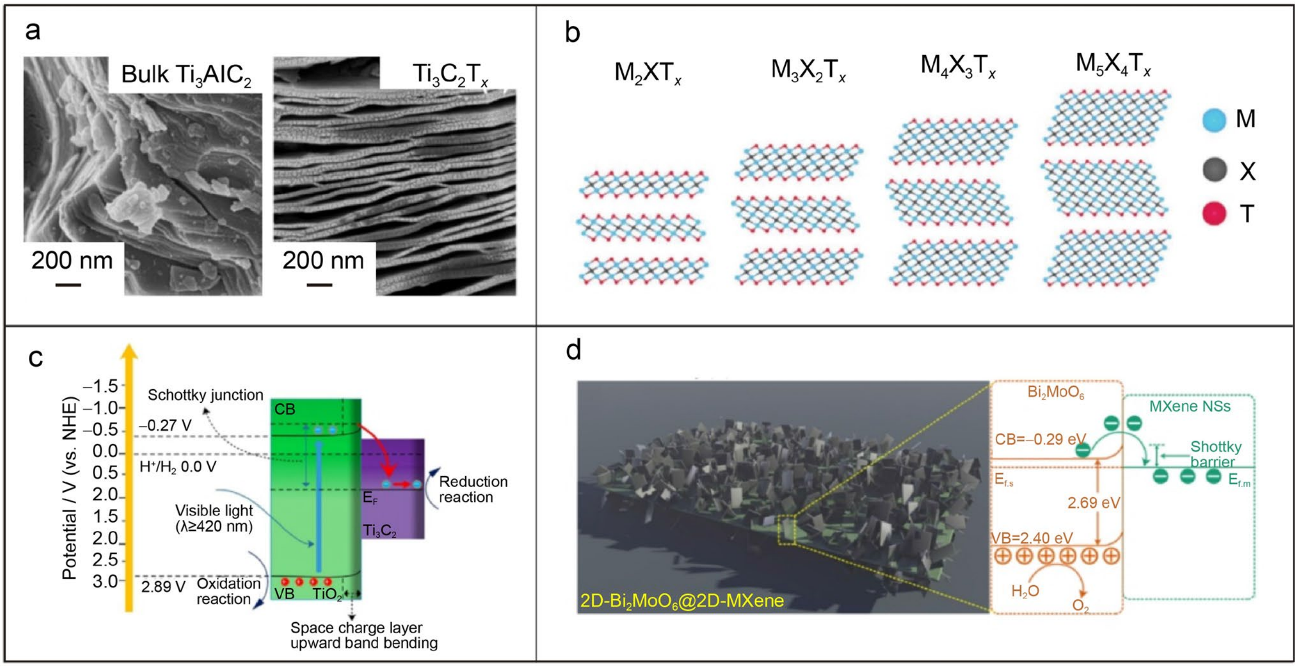

Fig. 11 **a** Field emission scanning electron microcopy images of bulk Ti_3AlC_2 and Ti_3AlC_2 after HF treatment. Reproduced with permission from Ref. [163]. Copyright 2022, ACS Publications. **b** Structural diagrams of the four kinds of MXenes. Reproduced with permission from Ref. [165]. Copyright 2022, Elsevier. **c** The charge-transfer process in the Ti_3C_2/TiO_2 system. Reproduced with permission from Ref. [166]. Copyright 2020, Elsevier. **d** Schematic diagram of the reaction mechanism of 2D-Bi_2MoO_6@2D-Mxene. (NSs: nanosheets) Reproduced with permission from Ref. [169]. Copyright 2020 Elsevier

3 Main factors affecting photocatalysis

In general, photocatalytic material properties and photocatalytic reaction conditions are the two main factors affecting the photocatalytic performance. This paper mainly discusses the influencing factors of the material itself, such as energy band structure, morphology, and crystal face, and further explains the unique influence of these influencing factors in the 2D nanomaterial system.

3.1 Band structure of photocatalysts

In the photocatalytic process, the core reaction process is: when light is irradiated on the photocatalyst, the catalyst absorbs light energy to generate electrons (e^-) with reducing ability and holes (h^+) with oxidative ability. e^- and h^+ further react with the system to generate free radicals, which reduce or oxidize substances in the environment such as H_2O, pollutants, heavy metal ions, and CO_2. This process is closely related to the energy band structure of the photocatalyst. On the one hand, the positions of the semiconductor photocatalysts CB and VB determine their redox capacity, that is, the more negative CB, the stronger the reduction capacity; the more positive VB, the stronger the oxidation capacity. In other words, the wider the forbidden band of the semiconductor photocatalyst, the stronger is its redox capacity [171]. On the other hand, the photoresponse range of semiconductor photocatalysts is also related to its forbidden bandwidth, as shown in Eq. (1):

$$E_g = 1240/\lambda\,(\mathrm{eV}) \tag{1}$$

E_g is the forbidden bandwidth of the semiconductor, and λ is the wavelength. The narrower the forbidden bandwidth, the wider the light absorption range, and the easier it is to be excited by light. According to this equation, the visible-light response range of the semiconductor photocatalytic material can be roughly estimated. The wavelength of 400–700 nm is the visible range. According to Eq. (1), the semiconductor photocatalyst that can respond to visible light has a bandgap range of about 1.77–3.1 eV. Therefore, in order to better respond to the visible-light range and improve the practical application potential of the photocatalyst, the bandgap of the photocatalyst should be selected in 3.1 eV or less.

Hydrogen production from water splitting is one of the main applications of photocatalytic technology. The water splitting process is closely related to the energy band of the photocatalyst. Figure 12 is a schematic diagram of the energy of photocatalytic water splitting when pH = 0. Protons are reduced by e^- in CB to generate hydrogen, while h^+ left in VB oxidizes water molecules to oxygen. In order to realize the whole water splitting reaction, two points must

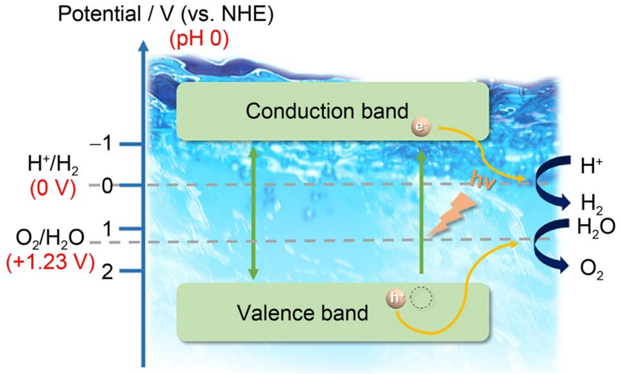

Fig. 12 Schematic diagram of the energy of photocatalytic water splitting

be satisfied: (i) the CBM is more negative than the reduction potential (0 eV) of H^+ to H_2, (ii) the VBM is larger than the oxidation potential of H_2O to O_2 (+ 1.23 eV). To satisfy the above two conditions, the minimum theoretical bandgap for driving water splitting is 1.23 eV. In theory, the bandgap of the semiconductor photocatalyst should be designed between 1.23 and 3.1 eV to ensure visible-light activity while overcoming the energy consumption of the water splitting reaction. In fact, some additional kinetic overpotentials are likely to be required to drive the electron transfer process in practical applications, and hydrogen evolution reaction (HER) and OER at reasonable reaction rates, semiconductors with bandgaps less than 1.6 eV will be limited by it [97]. At present, common semiconductors used for photocatalytic hydrogen production include TiO_2, ZnO, transition metal compounds (such as ZrO_2, CdS, and WO_3) and composite oxides with a layered perovskite structure. Since the energy band of 2D materials is very sensitive to external effects, it is an important research direction for photocatalysts to peel off traditional bulk semiconductor materials to prepare 2D materials.

Starting from the basic principles of photocatalysis, it can be known that the regulation of the bandgap is an extremely important modification method in photocatalysis. Many influencing factors and modification methods in photocatalysis basically change the bandgap of semiconductor catalysts, thereby changing the photocatalytic performance. Based on the semiconductor properties, its photocatalytic performance can be altered by tuning the VB, CB, and simultaneous tuning of the two. The methods for adjusting the bandgap of semiconductor materials include: thickness adjustment, element doping, heterojunction, external electric field, and strain engineering. Among them, for 2D materials with a layered structure, thickness adjustment is a very important mean of regulation, and many studies have proved that the bandgap change is strongly correlated with the thickness. We will go into more details in Sect. 4.

3.2 Catalyst morphology

The effect of material morphology on its properties is significant. In addition to the inherent morphology of the material, the catalysts can also design hollow structures [172], core–shell structures [173] and interlayer layered structures [174], showing flower-like [175], spherical [176] and other morphologies. The acquisition of different morphologies depends on their preparation methods, reaction times, and temperatures. Lu et al. synthesized CeO_2 materials with different morphologies by hydrothermal method and template method and have good applications in biological sterilization [177]. Figure 13a shows the transmission electron microscope (TEM) images of CeO_2 nanorods (NRs), nanocubes (NCs), nanosheets (NSs), hollow spheres (HSs), and mesoporous CeO_2 (m-CeO_2). Based on the area of the X-ray photoelectron spectroscopy (XPS) pattern, it is calculated that the CeO_2 nanorods have a higher concentration of Ce^{3+} and oxygen vacancies (Fig. 13b–d). Benefiting from this feature, CeO_2 nanorods have the most excellent tetracycline (TC) degradation performance (Fig. 13e, f). Free radical trapping experiments reveal that h^+ and superoxide radicals ($\cdot O_2^-$) play a major role in the degradation of TC (Fig. 13g). Liu et al. prepared TiO_2 with different morphologies (porous structure, flower-like nanospheres, and granular) by solvothermal method [178]. TiO_2 with a porous structure exhibits better catalytic activity due to the unsaturated coordinated Ti atoms and the highest concentration of oxygen vacancies, as well as the good adsorption properties brought about by the high specific surface area and low pore size. The above experiments show that it is necessary to study the different morphologies of the same material. The difference in morphology will create different surface states, showing different surface defects, adsorption properties, specific surface area, etc.

Due to the flexible and adjustable structure of 2D materials, the design of their morphology is easier than that of bulk materials. The commonly used methods are hydrothermal method and template method. The hydrothermal method can effectively prepare photocatalysts with different morphologies by changing the reaction conditions and reagents. The template method can design a more complicated specific shape through template induction.

When discussing the difference in morphology of 2D materials, the discussion of specific surface area is necessary. Generally speaking, the larger the specific surface area, the better the adsorption performance of the photocatalyst and the more active sites, so the catalytic performance is also better. In particular, the inherent layered structure of 2D nanomaterials can naturally lead to a large specific surface area, so that most of the active centers are exposed on the surface [179]. Du et al. prepared nanomesh B/O co-doped graphitic carbon nitride (BO-C_3N_4

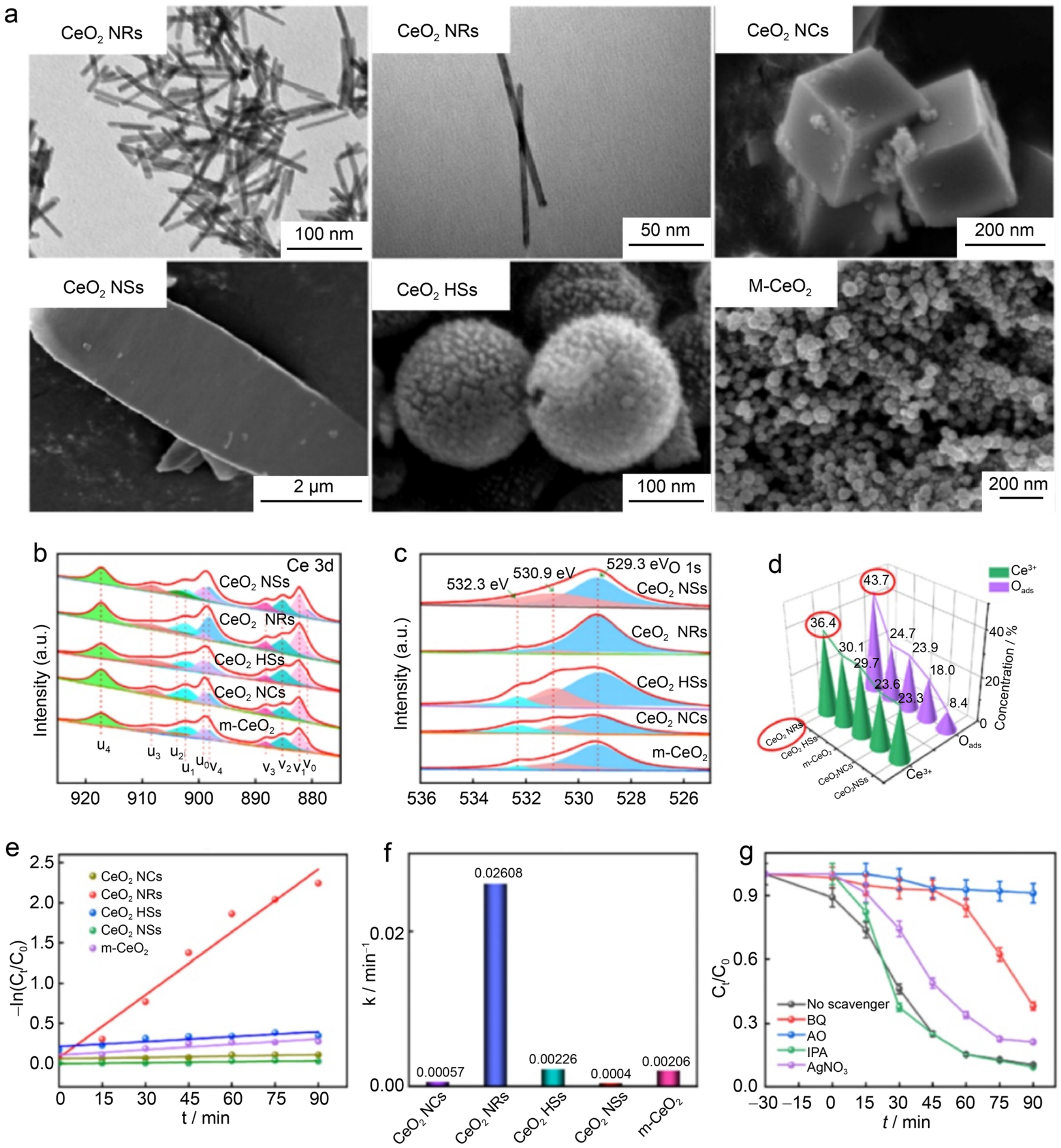

Fig. 13 **a** The TEM images of CeO_2 with different morphology. XPS spectra of synthesized CeO_2 samples, **b** Ce 3*d*, **c** O1*s*. **d** The Ce^{3+}/O_{ads} concentrations of CeO_2 with different morphologies. **e** The reaction kinetic curves of TC degraded by CeO_2 sample. **f** The kinetic rate constant TC degraded by CeO_2 sample. **g** The free radical trapping experiments of CeO_2 NRs. (BQ: benzoquinone. AO: ammonium oxalate. IPA: isopropanol) Reproduced with permission from Ref. [177]. Copyright 2023, Elsevier

nanomesh) [180]. The hydrogen production rate of BO-C_3N_4 nanomesh under visible-light irradiation is nearly 28 times higher than that of bulk g-C_3N_4. This is due to the unique 2D porous nanomesh structure, which enables BO-C_3N_4 to obtain a surface area of up to 160.58 $m^2 \cdot g^{-1}$. Liu et al. constructed a porous SnO_2 precursor with obvious photocatalytic activity [181]. Then, using In_2O_3 as a sensitizer to increase the specific surface area of the porous SnO_2 matrix, the specific surface area of the porous SnO_2 was increased by 3 times, and the photocatalytic performance was 1.94 times that of the original porous SnO_2.

However, some scholars hold different views. Some studies have pointed out that the photocatalytic activity of the material may not be related to the specific surface area. Li et al. synthesized graphitic carbon nitride with low specific surface area by silica template method, and its photocatalytic activity was improved compared with the high specific surface area graphitic carbon nitride synthesized by traditional method [182]. Studies have shown that this is because the synthesized low specific surface area graphitic carbon nitride has more free electrons and a lower recombination rate of carriers. In contrast, the size of the specific surface area is not the main factor affecting the photocatalytic performance.

The above studies show that it is a feasible method to improve the photocatalytic performance by changing the morphology of the catalyst and increasing its specific surface area. However, it cannot be simply assumed that the specific surface area of the material must be positively correlated with the improvement of the photocatalytic performance. The changes in the catalytic process at the microscopic level caused by the specific surface area should be further explored, which in turn guides the design of catalyst morphology and structure.

3.3 The structure of crystal face

Photocatalytic reactions generally occur on the surface of photocatalysts, so the reaction process is closely related to the surface atomic structure [183]. Since different crystal faces of photocatalysts naturally have different atomic arrangements, they can further affect key steps in photocatalytic reactions such as adsorption, desorption, and electron transfer processes. The research on TiO_2 single crystal surface regulation published by Yang et al. in 2008 is the most representative work on semiconductor crystal surface regulation [184]. Its research found that the concentration of F ions can precisely control the exposure ratio of (001) crystal planes, significantly reduce the surface activation energy of (001) crystal planes, and promote the growth of (001) crystal planes. This work demonstrates the feasibility of finely tuned crystal planes. Subsequent studies have shown that by adjusting the concentration of specific ions, changing the pH values, adding surfactants, etc., specific crystal faces can be effectively exposed to further improve the photocatalytic performance of the system. Nowadays, facet engineering has become a common means of photocatalyst regulation. At present, the active crystal planes of some typical 2D materials have been identified, such as Li et al. synthesized WO_3 thin films with different exposure ratio (002) planes by a simple hydrothermal method [185]. The proportion of each crystal plane of different WO_3 samples was calculated by X-ray diffraction (XRD) spectrum (Fig. 14a), and the layer spacing corresponding to (002) crystal plane was also observed in TEM spectrum (Fig. 14b). Through a series of characterizations such as current density–voltage curve (J–V curve) (Fig. 14c), electrochemical impedance spectroscopy (EIS) (Fig. 14d) and Mott–Schottky plots (M–S plots) (Fig. 14e), it was found that with the increase of the (002) plane exposure rate, the separation of photogenerated carriers was promoted and the photoelectrochemical (PEC) performance was improved. Hu et al. prepared MoS_2 nanosheets with higher activity (100) surface concentration at lower pH values, and the photocatalytic performance was effectively improved [186]. CdS with exposed (002) crystal faces also showed better performance in catalyzing hydrogen evolution [187]. The regulation of specific crystal planes can also control the thickness of 2D materials. Guan et al. used polyvinyl pyrrolidone (PVP) as an active agent to synthesize ultrathin BiOCl nanosheets with a thickness of 2.7 nm, while the thickness of BiOCl nanosheets without PVP was 30 nm [188]. The generation of ultrathin nanosheets is due to the deposition of PVP on the bottom and top (001) planes, preventing the growth of the longitudinal planes (Fig. 14f). TEM images and atomic force microscopy (AFM) revealed its crystal planes and thickness (Fig. 14g, h). Ultrathin BiOCl nanosheets show superior RhB degradation activity (Fig. 14i). Figure 14j, k reveals the distribution of defects in the samples, triple Bi^{3+} oxygen vacancy dominates in ultrathin BiOCl nanosheets, while isolated Bi vacancies dominates in BiOCl nanoplates.

Compared with traditional materials, 2D materials require more complex crystal facet engineering due to their 2D anisotropic growth and thermodynamic factors. In general, there are two factors influencing the formation of specific crystal planes: thermodynamic and kinetic driving forces. From a thermodynamic point of view, the material facets exposed to the lowest surface energy will eventually be preserved. Kinetically, the slowest growing facets will eventually be preserved. Therefore, how to find a balance between the minimum energy exposure surface and the minimum total area is the challenge that the crystal plane engineering of 2D materials needs to face. In other words, researchers need to think about how to expose specific crystal faces while maintaining the ultrathin atomic thickness unique to 2D materials [189].

3.4 Crystal structure

The same material has different crystal structures due to different atomic arrangements. Different crystal structures have different forbidden bandwidths, so they will show different catalytic properties. The choice of crystal structure of photocatalytic materials is also an important factor to improve their catalytic properties. Taking TiO_2 as an example, TiO_2 has three crystal structures: anatase, rutile and brookite. Among them, the most common structures are anatase and rutile. The forbidden bandwidths of anatase-type TiO_2 and rutile-type TiO_2 are 3.2 eV and 3.0 eV, respectively, so anatase-type TiO_2 has stronger redox ability. At the same time, anatase TiO_2 has a larger specific surface area, more lattice defects, and higher separation efficiency of electron–hole pairs, thus possessing stronger photocatalytic performance [190]. MoS_2 is a typical material with different crystal structures leading to different photocatalytic properties. 1T-MoS_2 brings better photocatalytic performance

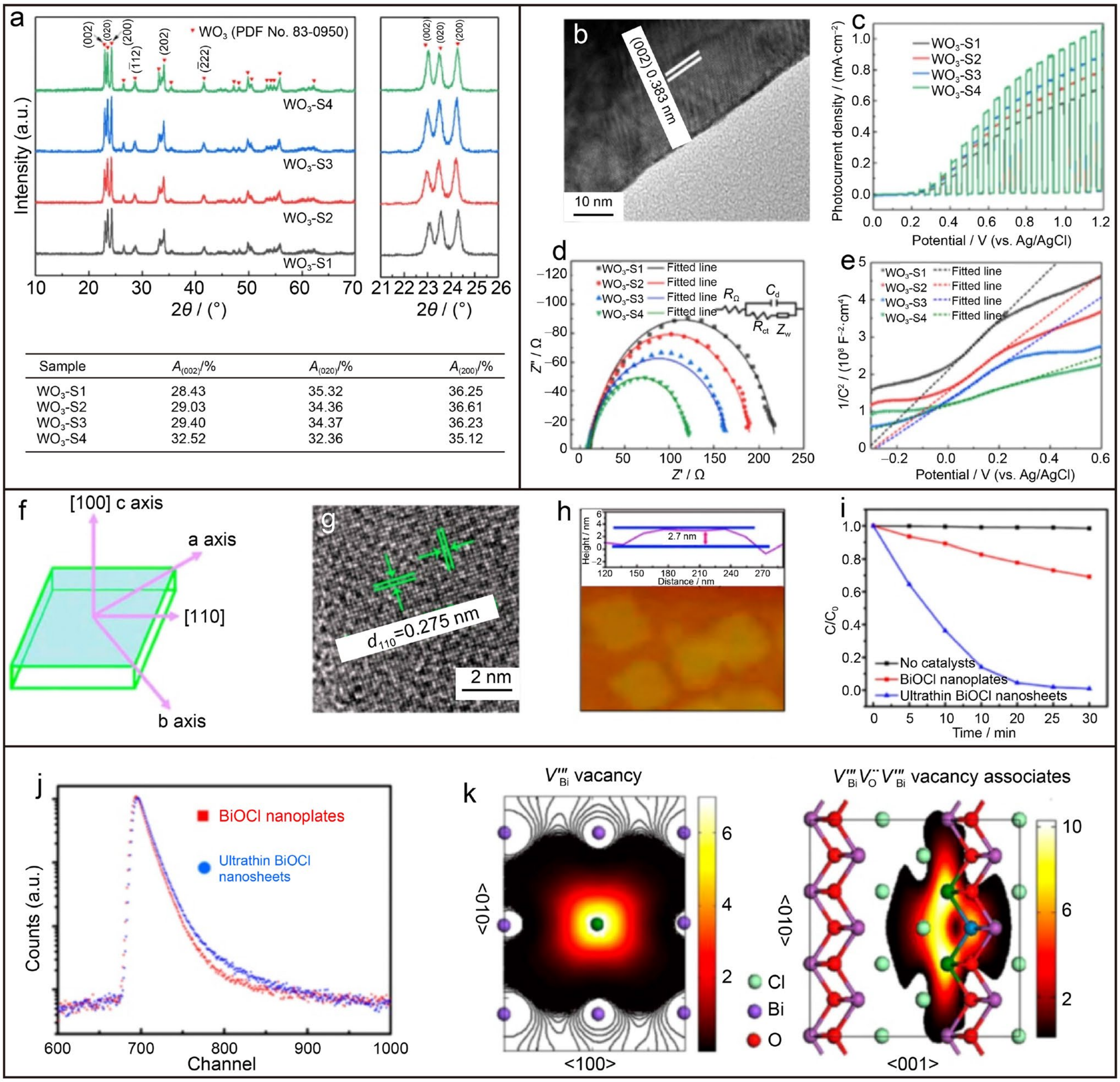

Sample	$A_{(002)}$/%	$A_{(020)}$/%	$A_{(200)}$/%
WO$_3$-S1	28.43	35.32	36.25
WO$_3$-S2	29.03	34.36	36.61
WO$_3$-S3	29.40	34.37	36.23
WO$_3$-S4	32.52	32.36	35.12

Fig. 14 **a** XRD patterns and calculated crystal facet ratios of different WO$_3$ samples. **b** The TEM image of WO$_3$-S4. **c** The J–V curve of different WO$_3$ samples. **d** The EIS of different WO$_3$ samples. **e** The M–S plots of different WO$_3$ samples. Reproduced with permission from Ref. [185]. Copyright 2023, Elsevier. **f** Schematic illustration of the crystal orientation of the nanosheet. **g** The high resolution transmission electron microscopy (HRTEM) images of the ultrathin BiOCl nanosheet. **h** The atomic force microscopic image of the ultrathin BiOCl nanosheet. **i** The RhB degradation curve. **j** The positron annihilation spectroscopy. **k** The positron lifetime spectrum. Reproduced with permission from Ref. [188]. Copyright 2013, ACS Publications

than 2H-MoS$_2$ due to the significantly lower charge-transfer resistance. Meanwhile, the active sites of 1T-MoS$_2$ are distributed in a large number in the plane, rather than in the edge zone as in 2H-MoS$_2$. However, since the 1T phase is not stable enough in nature, it will spontaneously transform into the 2H phase. How to utilize the 1T phase with better catalytic performance is one of the research focuses of MoS$_2$ catalytic application. At present, intercalation of alkali metal ions, heteroatom doping and laser beam irradiation are considered to be effective methods for phase modulation [191]. Among them, the hydrazine hydrate-induced phase transition method is a simple and effective method. Li et al. regulated and synthesized a stable 1T-MoS$_2$ phase by hydrazine hydrate without obvious transformation within 3 months, and its conductivity was 700 times that of 2H-MoS_2 [192]. Jia et al. easily adjusted the ratio of 1T phase to 2H phase of MoS_2 by simply adjusting the amount of hydrazine hydrate, and the obtained MoS_2 had a small Tafel slope with 56.6 mV·dec^{-1} [101]. However, the current research on the photocatalytic performance of 1T-MoS_2 has not yet obtained satisfactory results. 1T-MoS_2 is usually used as a co-catalyst in photocatalysis to enhance the photocatalytic performance, which benefits from its metallicity. Liu et al. prepared a 1T/2H-MoS_2 mixed phase loaded TiO_2 nanorod system by a hydrothermal method [193]. The system exhibited excellent performance in the photocatalytic hydrogen evolution process. Mixed phase MoS_2 exhibits better co-catalyst performance than Pt. Through Perdew–Burke–Ernzerhof (PBE) calculation (Fig. 15), it can be seen that due to the embedding of 1T-MoS_2 layer, the mixed phase MoS_2 exhibits conductor characteristics, which is helpful for the catalytic hydrogen evolution reaction on TiO_2.

For 2D nanomaterial photocatalysts, the crystal structure is also a significant influencing factor in their photocatalytic applications. Due to the strong correlation between the geometric properties and performance of 2D nanomaterials, by controlling the thickness of 2D nanomaterials, the crystal structure can be adjusted, so that different bandgap widths, electronic properties, etc. can be obtained on the same material. Huang et al. selectively destroyed the hydrogen bonds between g-C_3N_4 layers to adjust the crystal structure of g-C_3N_4, and obtained layer plane ordered porous carbon nitride (LOP-CN) [194]. The photocatalytic hydrogen production performance of LOP-CN is 7.4 times that of pristine g-C_3N_4. Studies have shown that the improvement of photocatalytic performance is due to the long-range atomic order layer plane brought by the new crystal structure, which improves the diffusion length of electrons in the plane, thereby enhancing the charge separation ability. Meanwhile, the broken interlayer hydrogen bonds lead to the formation of a large number of slit holes, providing more active sites.

3.5 Catalyst defect

Defects in materials can generally be divided into intrinsic defects, electron defects and hole defects, and the intrinsic defects are mainly caused by the deviation of the stoichiometric ratio of the material itself. Material defects can affect photocatalysts in several ways. On the one hand, it affects the band structure of the catalyst. Defects will introduce new energy levels in the energy band structure of semiconductor photocatalysts, thereby shortening the forbidden band width and enhancing the absorption ability of visible light. On the other hand, due to the existence of defects, the adsorption of H_2O and O_2 is enhanced, which can further generate a large number of active free radicals, thereby improving the photocatalytic performance. At the same time, the defects can serve as electron-trapping centers, which are beneficial

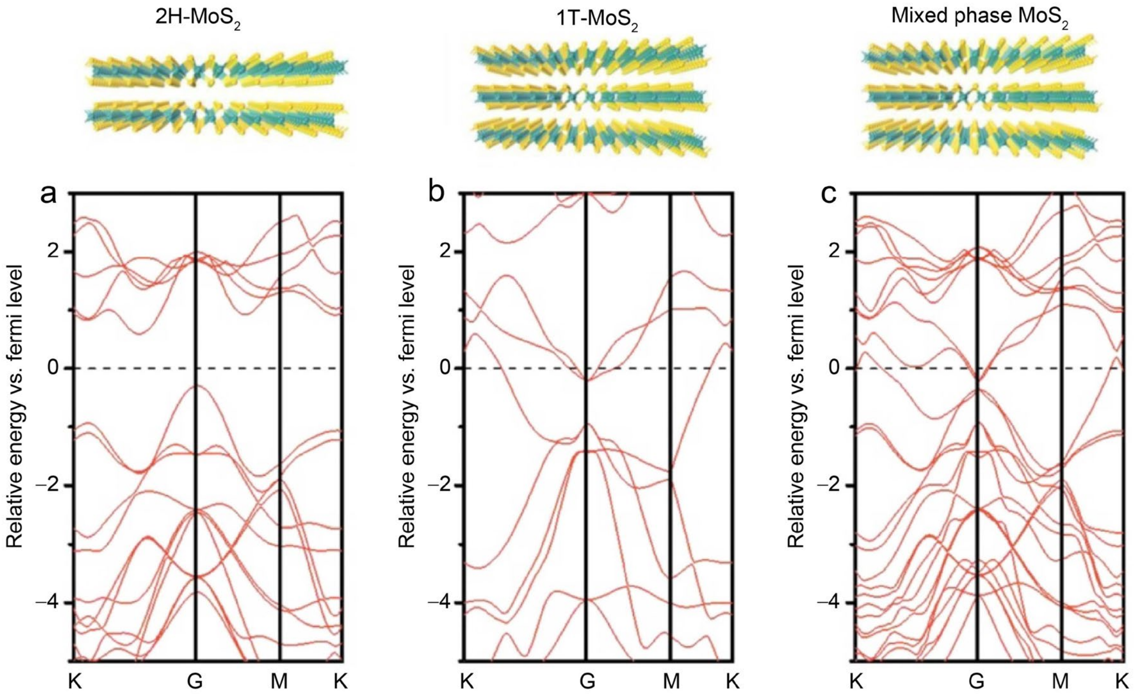

Fig. 15 PBE calculated band structures of **a** 2H-MoS_2, **b** 1T-MoS_2, and **c** mixed phase MoS_2. Reproduced with permission from Ref. [193]. Copyright 2019, Elsevier

to the separation of electron–hole pairs and improve the photocatalytic performance [195]. In conclusion, the purposeful introduction of defects can enhance the performance of photocatalysts. Due to the reduction of its thickness, the local atomic structure of 2D nanomaterials is significantly different from that of bulk materials, such as coordination number, bond length, bond angle, and surface atomic disorder, so it is easy to form more surface defects [196]. Therefore, for 2D nanomaterials, it is necessary to study the effect of surface defects on the photocatalytic performance. As an effective modification method for photocatalysts, defect engineering has been extensively studied, and the details will be further introduced in Sect. 4.5 of this paper.

4 Main modification methods and their mechanisms

4.1 Elemental doping

Most of the semiconductor photocatalysts are n-type semiconductors, and they all have a special energy band structure different from that of metals or insulating substances: there is a forbidden band between the VB and the CB. The relationship between the light absorption wavelength range of the semiconductor and the bandgap can be expressed by the above-mentioned Eq. (1)

The absorption wavelength range of commonly used wide-bandgap semiconductors are mostly in the ultraviolet region. For example, TiO_2 is a typical material that can only respond to ultraviolet light due to the wide bandgap. Since light absorption is an important process in photocatalytic reactions, the widening of the visible-light response range is of great significance for the practical application of photocatalytic technology. By shortening the bandgap, the photoresponse range can be effectively broadened. Studies have shown that by doping metal or non-metal elements, the bandgap of the photocatalyst can be effectively adjusted, its energy band structure can be changed, and the photoresponse range of the catalyst can be broadened [197]. At the same time, the introduction of impurity elements can also effectively enhance the concentration of carriers. As effective electron acceptors, metal ions can become photogenerated electron capture sites and hinder the recombination of electron holes [198]. In conclusion, doping can improve the photocatalytic performance of materials in multiple dimensions. Next, the mechanism of metal element doping and non-metal element doping will be introduced in detail to understand the role of doping in bandgap regulation.

The doping of metal elements has been studied for a long time and is more mature. The main principle is to change the light absorption range by the introduction of impurity energy levels. Figure 16a, b is schematic diagrams of metal element doping. The introduction of donor level and acceptor level enables electrons not only to be excited from the VB to the CB, but also to transition from donor level to the CB, or from the VB to acceptor level. The change in the forbidden bandgap allows semiconductors to absorb visible light. The type of element and the position of doping are the factors that affect the catalytic activity. Common metal atom dopings include Fe [199], Ni [200], Mn [201], Ag [202], Au [203], and Pt [204]. Tonda et al. prepared Fe-doped g-C_3N_4 nanosheets, which had a 7 times higher degradation rate of RhB than bulk g-C_3N_4 [205]. Shah et al. prepared Mn-doped $BiFeO_3$ nanofilms (Mn-BFO) [206]. The oxygen evolution activity of Mn-BFO under visible-light irradiation is significantly improved compared to pure BFO. Bandgap studies show that the bandgap of Mn-BFO can be tuned from 2.1 to 1.36 eV by changing the doping amount of Mn, thereby broadening its optical response range. Qin et al. prepared Ag-doped g-C_3N_4 [207]. Under visible-light irradiation, Ag-g-C_3N_4 exhibits good photocatalytic hydrogen evolution activity, and the highest hydrogen evolution rate is 3.62 times that of the pure phase.

The doping of non-metallic elements can also change the energy band structure, but unlike metallic elements, it does not introduce new energy levels, but shortens the energy band. The specific process is shown in Fig. 16c. Common

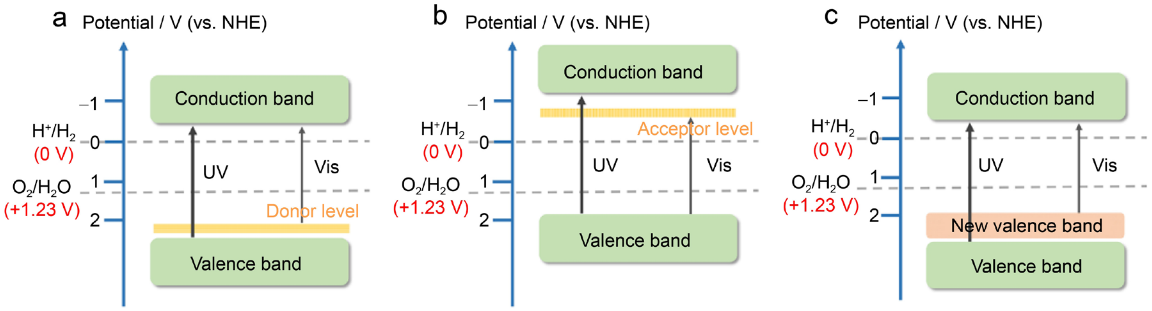

Fig. 16 **a** Doping of metal elements to introduce the donor energy level. **b** Doping of metal elements to introduce the acceptor energy level. **c** Doping with non-metallic elements shortens the energy band

non-metallic elements used for doping are N, B, O, P, S, etc. The doping of non-metal elements compared to metallic elements can well avoid the effect of thermochemical instability on the photocatalytic activity. Thus, doping method with non-metal elements is more widely used. For example, the reason for the better photocatalytic performance of N-doped TiO_2 can be simply explained as follows: N-doping forms a state in the bandgap that can absorb visible light, and N-doping induces oxygen vacancies, thereby enhancing the photocatalytic performance [208]. Wang et al. prepared S-doped g-C_3N_4 (Fig. 17a) [209]. By doping element S, the bandgap of g-C_3N_4 is narrowed from 2.7 to 2.63 eV (Fig. 17b), the photoresponse range is broadened to 475 nm, and the photocatalytic reduction of CO_2 shows more outstanding performance. Kong et al. prepared N-doped ZnO/g-C_3N_4 composites [210]. Compared with pure g-C_3N_4, ZnO and composite ZnO/g-C_3N_4, N-ZnO/g-C_3N_4 degrades MB and phenol better under visible-light irradiation. The studies showed that one of the reasons for the improvement of photocatalytic performance is the change of the energy band structure and the improvement in stability brought by doping N.

In summary, it can be seen that element doping is an effective mean to narrow the bandgap of photocatalysts, and the narrowed bandgap can broaden the visible-light absorption range. In addition to metal doping and non-metal doping, co-doping is also widely used as a doping method, and the synergistic effect between two different elements also has a profound impact on the performance of semiconductor catalysts [203, 211]. Currently, there is no research on controllable bandgap narrowing, and the bandgap change caused by element doping is still an unquantifiable thing.

Usually, doping is achieved by introducing dopants containing corresponding elements during the preparation process or post-treatment process of the semiconductor material precursor. Dopants can be liquid, solid or gaseous. Taking N element doping as an example, the common doping method is hydrothermal method using ammonia solution (such as formamide and ammonia water), calcination of precursors containing nitrogen elements, or nitriding materials in NH_3 atmosphere. The element type, element position, doping concentration and doping solubility are the main influencing factors in the doping process. The doping solubility refers to the solubility of the dopant in the host material. In general, solubility is limited due to interactions between elements. Even the maximum solubility sometimes fails to achieve effective photocatalytic performance. In addition to selecting elements with higher solubility, appropriate post-treatments such as annealing, pressurization, and thermal cycling can also increase doping solubility [212, 213]. However, the current solubility enhancement methods have problems such as cumbersome process and unclear mechanism, which need to be further explored and discussed. It is worth looking

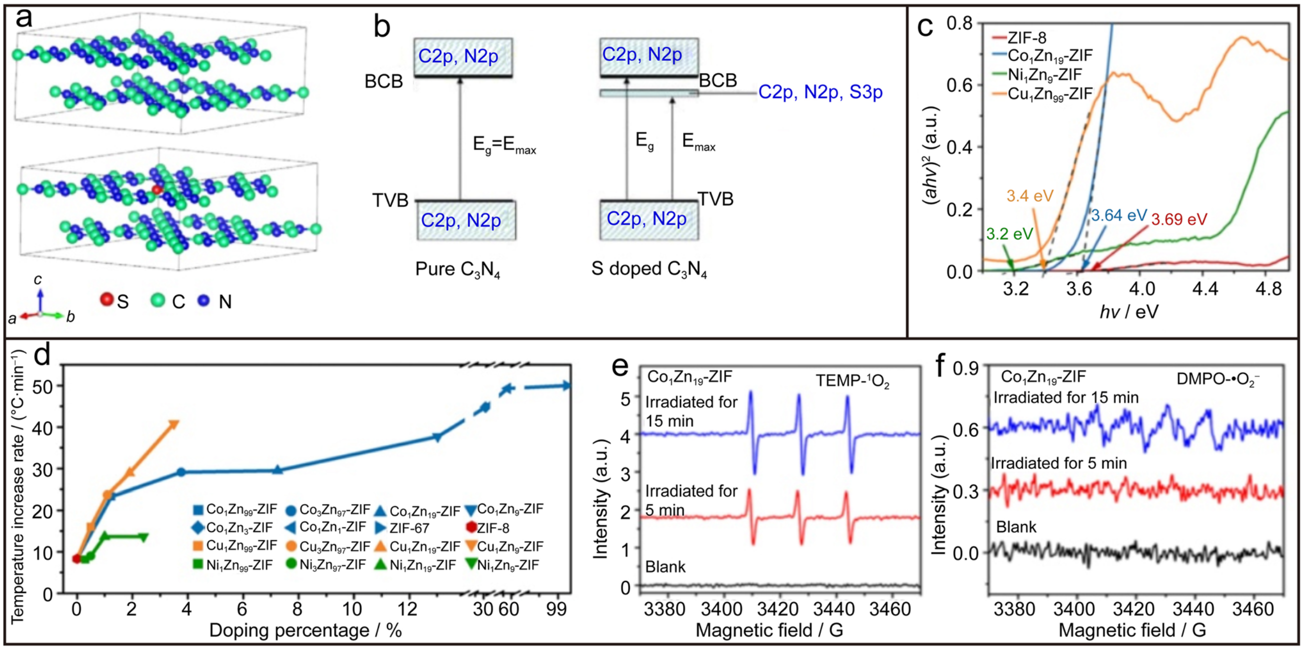

Fig. 17 **a** Unit cell of pure C_3N_4 and sulfur-doped C_3N_4. **b** Schematic diagram of the band structures of pure g-C_3N_4 (left) and S-doped g-C_3N_4 (right). (BCB: bottom of CB. TVB: top of VB) Reproduced with permission from Ref. [209]. Copyright 2015, Elsevier. **c** The Tauc plots of different samples. **d** Photo-induced temperature rise rates of different samples. **e** The electron paramagnetic resonance (EPR) spectra of 2,2,6,6-tetramethylpiperidinyl (TEMP-$^1O_2$) for Co_1Zn_{19}-ZIF. **f** The EPR spectra of 5,5-dimethyl-1-pyrroline N-oxide (DMPO-O_2^-) for Co_1Zn_{19}-ZIF. Reproduced with permission from Ref. [214]. Copyright 2023, Elsevier

forward to that, compared with bulk surface doping, 2D nanomaterials have the characteristic of thin thickness. The doping process of 2D materials requires only a small diffusion depth to form uniform doping, which is more conducive to adjusting the electronic structure, light absorption and improving photocatalytic activity, and can significantly change its physicochemical properties. In general, doping alone cannot effectively improve the visible-light response, and the defects caused by doping may also become the recombination sites of electrons and holes, which has a negative effect on the photocatalytic performance. The direction to solve this problem is to explore the mechanism of doping more deeply through the combination of various characterization methods and computational simulations.

The study of element types and doping concentration in the doping process is very necessary to explore the catalytic mechanism of the system. Li et al. studied the doping of ZIF-8 with different concentrations of different metal ions (Co^{2+}, Ni^{2+}, Cu^{2+}) [214]. All doped ZIFs have narrowed bandgap and enhanced light-harvesting and photogenerated carrier separation efficiencies (Fig. 17c). As the concentration increases, the photothermal conversion efficiency gradually increases, which is conducive to its application in sterilization (Fig. 17d). The introduction of Co sites makes the photoactive oxygen change from a single oxygen state ($^1O_2$) to multiple oxygen states ($^1O_2$ and $\cdot O_2^-$), which can better participate in the sterilization. Therefore, Co^{2+} with a doping concentration of 5% has the highest bactericidal efficiency on *Escherichia coli* (Fig. 17e, f).

In addition to the study of bandgap changes and surface active sites, the researchers also conducted an in-depth study of the carrier dynamics through transient absorption spectroscopy, revealing the role of doping in the carrier dynamics. For example, Zhao et al. prepared 0.6% Re-doped monolayer MoS_2 [215]. Using transient absorption spectroscopy, it is characterized that the average exciton lifetime of undoped MoS_2 is 22 ps, while the exciton lifetime of Re-MoS_2 is as low as 1 ps. This work reveals the effect of Re impurities on the catalytic performance of native MoS_2 in terms of carrier dynamics. It is worth noting that the excitons in the 2D material system are more stable than other materials, which is more conducive to the in-depth exploration of optoelectronic technology. The dark excitons that cannot be detected because they do not interact with light can be observed in 2D material systems [216].

4.2 Noble metal deposition

Studies have shown that by depositing noble metals on semiconductor photocatalysts, a "junction", the Schottky junction, can be constructed between the semiconductor photocatalyst and the noble metal, thereby controlling the directional flow of electrons to improve the separation efficiency of carriers [217, 218]. In addition, the local surface plasmon resonance (LSPR) effect of noble metals can also effectively promote the absorption of light by semiconductor photocatalysts. Its mechanism is shown in Fig. 18a. Metal nanostructures with LSPR effect, when the oscillation frequency of electrons is consistent with the frequency of incident light waves, a strong resonant absorption peak will appear [219]. Hot electrons are generated during the decay of the oscillation, and the injection of hot electrons into the CB of adjacent semiconductors will contribute to the improvement of photocatalytic performance. Figure 18b reveals the injection mechanism of hot electrons in different cases [220]. In order to explore how the LSPR effect acts on the photocatalytic process and the formation of the Schottky junction, the researchers carried out many experimental investigations. Fang et al. prepared Ag nanoparticles (NPs)-doped $BiVO_4$ photonic crystal inverse opal (Ag/io-$BiVO_4$) [221]. The photocurrent density of Ag/io-$BiVO_4$ is 4.7 times higher than that of the disordered samples without Ag NPs. In the degradation of MB, Ag/io-$BiVO_4$ also showed the most excellent activity. With the in-depth exploration of the photocatalytic mechanism, compared with d-$BiVO_4$, the enhanced photocatalytic activity of Ag/io-$BiVO_4$ can be explained from the following three aspects. First, due to the slow light effect, the interaction between io-$BiVO_4$ and light-matter is enhanced, and the absorption intensity of light is higher than that of d-$BiVO_4$ (Fig. 18c). Second, the absorption range of the electronic bandgap of $BiVO_4$ coincides with the LSPR wavelength of Ag NPs (Fig. 18d), which facilitates the generation of carriers. The incident monochromatic photon-electron conversion efficiency test (IPCE test) also confirmed this (Fig. 18e). Finally, the Schottky junction constructed between Ag and io-$BiVO_4$ realizes the effective separation of carriers. Its formation mechanism is shown in Fig. 18f. When Ag NPs are in contact with $BiVO_4$, free electrons are redistributed on the interface until the Fermi level reaches an equilibrium state and cause upward bending of the semiconductor band edge, so a Schottky barrier is formed between Ag and $BiVO_4$. Ag acts as an electron trap, which helps the effective separation of electron–hole pairs. At present, Ag, Au, Pd, Pt, etc. are commonly used in noble metal deposition. The modification method of noble metal deposition is also widely applicable to a variety of material systems [222–224]. Same as doping, the photocatalytic activity of the material is related to the type of precious metal, the amount of deposition and the preparation method. Excessive deposited noble metals may also become the recombination center of carriers, hindering the separation of photogenerated carriers, thereby reducing the photocatalytic activity.

In general, the deposition of noble metals can be achieved by wet chemical method, physical vapor deposition, photodeposition, and atomic layer deposition (ALD). Among

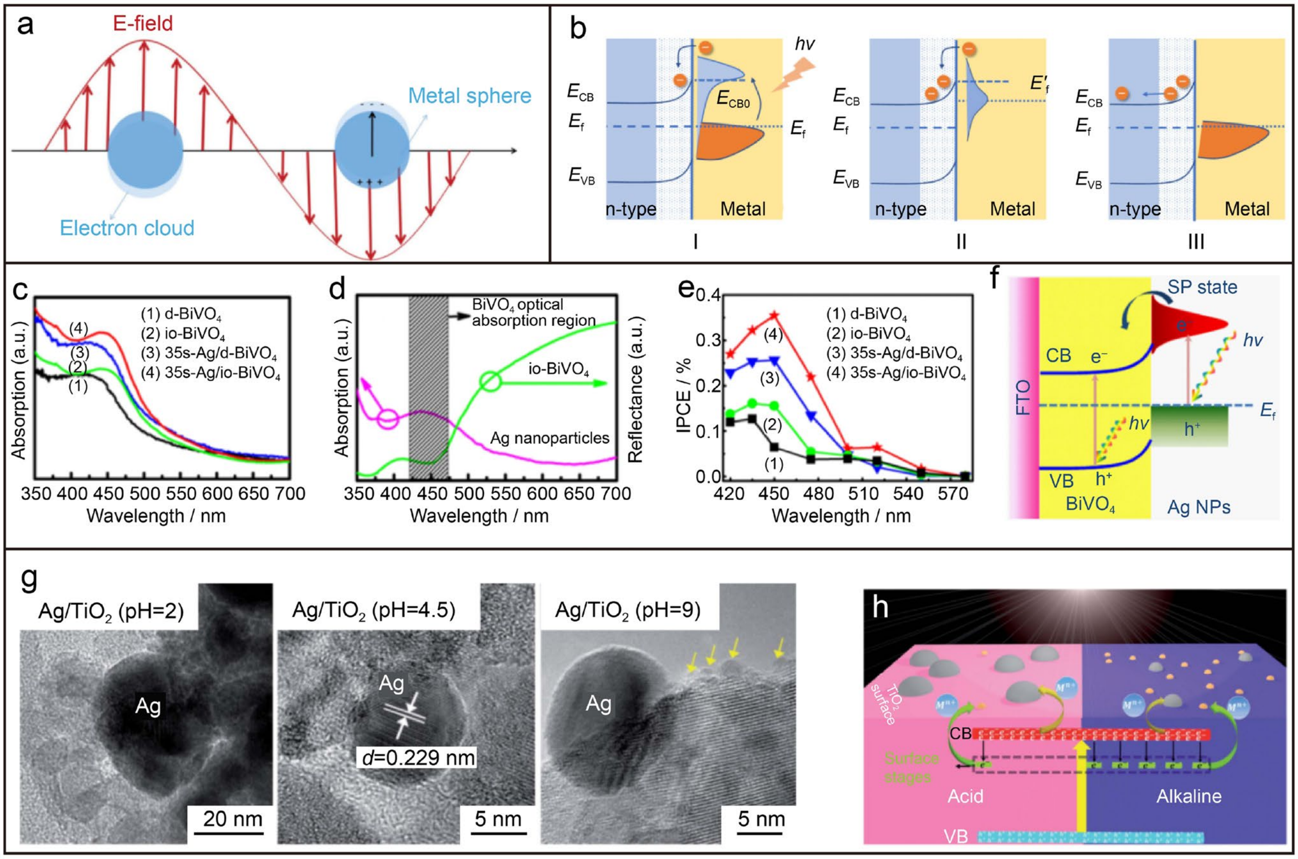

Fig. 18 **a** Schematic diagram of LSPR. Reproduced with permission from Ref. [219]. Copyright 2014, ACS Publications. **b** Schematic illustration of the hot-electron-injection effect: excitation of the electrons from thermal equilibrium to a high-energy state upon absorbing photons and injection of the electrons to the CB of the semiconductor (I). Redistribution of electron energy and formation of a Fermi–Dirac distribution at a high-temperature Fermi level after the injection of the electrons (II). Restoration of the standard electron distribution with electrons and holes flowing to different regions in the semiconductor (III). Reproduced with permission from Ref. [220]. Copyright 2015, John Wiley and Sons. **c** The absorption spectra of different BiVO$_4$ samples. **d** The absorption spectrum of the Ag NPs and the reflectance spectrum of the io-BiVO$_4$ sample. **e** The IPCE spectra of different BiVO$_4$ samples. **f** The schematic diagram of Schottky junction of Ag/BiVO$_4$. Reproduced with permission from Ref. [221]. Copyright 2016, AIP Publishing. (FTO: F-doped tin oxide) **g** The HRTEM images of different Ag/TiO$_2$ samples. **h** The schematic diagram of the formation mechanism of Ag NPs different sizes. Reproduced with permission from Ref. [226]. Copyright 2020, Royal Society of Chemistry

them, the wet chemical method is easy to operate. Noble metals are deposited by deposition, wet impregnation, drying, heat treatment, etc. In order to avoid the occurrence of agglomeration during the deposition process, low concentrations of metal precursors should usually be selected. In alkaline reagents, due to the negative charge on the surface of metal oxides, noble metal cations can be attracted and deposited by electrostatic interaction, so this method is very suitable for the deposition of noble metals on the surface of metal oxides [225]. Photodeposition is also a common method of noble metal deposition. Its basic process is to use photogenerated electrons and holes to reduce the noble metal ions adsorbed on the semiconductor surface, so as to achieve noble metal deposition at specific active sites. It is a method that can accurately design noble metal deposition sites [226]. ALD technology is a new vapor deposition method. The basic process is to expose the base material to the vapor phase metal precursor and deposit it layer by layer. The advantage of this method is that the composition and thickness of the noble metal atomic film can be controlled to the atomic level, and it is a potential preparation method for exploring the deposition of single-atom noble metals and improving the utilization rate of noble metals. However, due to the high vacuum environment and expensive preparation price, ALD technology cannot be put into mass production [227]. During noble metal deposition, proper noble metal size and distribution also play a key role in the photocatalytic performance. Since noble metals usually have a more negative Fermi level than host materials, their growth process is fast, and they often have large sizes or uneven distribution during deposition process. Huang et al. changed the surface state of TiO$_2$ by adjusting the pH values, and studied its effect on the deposition of noble metals by Photodeposition [226]. When the pH values was low, the size of the deposited Ag Nps was larger than 10 nm, and when the pH values was 9, the small size Ag Nps of 0.5–2.0 nm appeared (Fig. 18g). As Fig. 18h shown, the formation of small-sized Ag NPs may be due to that some of photoelectrons are trapped by –OH under alkaline conditions during the electron transition to CB. Both photoelectrons located at CB and trapped by –OH can perform reductive deposition of Ag ions. Since the photoelectrons trapped by –OH have smaller energy and area than those on CB, smaller Ag NPs are generated. TiO_2 deposited by large-sized Ag NPs showed better photocatalytic hydrogen evolution activity. In summary, the size and distribution of noble metals are related to the nucleation and growth process regulated by the surface state and charge, and the size has a significant impact on the photocatalytic performance.

Strictly speaking, the Schottky junction formed by the recombination of noble metal and semiconductor is essentially a kind of heterojunction. Compared with the heterojunction constructed by semiconductors and semiconductors, it has obvious rectification properties, which can adjust the current shape, form a Schottky barrier at the interface, leave the negative charges on the metal, and separate the positive charges in the semiconductor, so as to effectively separate the carriers. At the same time, due to the metal-specific LSPR effect, when visible light irradiates the metal surface, the free electrons on the metal surface are resonated by the light wave, which will enhance the oscillating electric field around it, causing the electrons to be easily excited, thereby improving the catalysis efficiency. Due to the above characteristics, noble metal deposition has great research significance in regulating the photocatalytic performance of semiconductor catalysts.

4.3 Heterojunction

In addition to the noble metal deposition method mentioned above, which can effectively solve the problem of the fast electron–hole recombination speed of 2D nanomaterials, the construction of heterojunctions is also one of the most widely used strategies to solve this problem. As shown in Fig. 19a, heterojunctions can be basically divided into three categories. In type I, the CB and VB of semiconductor B are higher than A, holes in the VB of B can be transferred to the VB of A, and electrons in the CB can be transferred to the CB of A. But such heterojunctions did not promote separation of photogenerated carriers. There are two different mechanistic explanations for type II heterojunctions. One view is that holes in the VB of A can be transferred to the VB of B, and electrons in the CB of B can be transferred to the CB of A. Electrons are enriched in the CB of A, while holes are enriched in the VB of B, so that electron–hole pairs can be effectively separated. Another point of view is that the electrons in the CB of A may directly recombine with the holes in the VB of B, leaving the holes in the VB of A and the electrons in the CB of B to play a photocatalytic role. The most popular Z-type heterojunction theory in recent years. Type III can be regarded as another Z-type heterojunction, where electrons in the CB of A recombine with holes in the VB of B, thereby separating electron–hole pairs [228].

Heterojunctions composed of 2D materials and other semiconductor interfaces of different dimensions can integrate their respective advantages. For example, when 2D materials are composited with 0D materials, they can exist as good base materials, so that the 0D materials can be dispersed more uniformly. At the same time, the heterogeneous interfaces have various forms and a large number of active sites, which can effectively improve the catalytic performance. 2D materials are composited with 1D materials, and their heterointerfaces can capture photons and utilize sunlight more efficiently, thereby improving catalytic performance. The heterostructure of 2D materials and 2D materials has many special catalytic advantages due to its unique face-to-face contact structure. The close face-to-face contact creates a high specific surface area, strong coupling effect, and promotes current carrying. At the same time, due to the electron tunneling effect, the charge transport path is shortened and the transfer speed is accelerated [229, 230]. Therefore, rational design of heterojunctions between 2D materials and different materials is an effective means to synthesize excellent photocatalysts. Liu et al. prepared a 2D/0D photocatalyst composited with carbon nanodots (CQDs) and ultrathin g-C_3N_4(UCN) nanosheets [231] (Fig. 19b). CQDs/g-C_3N_4 exhibited excellent hydrogen evolution photocatalytic activity under visible-light irradiation. Figure 19c demonstrates the role of the heterojunction in the CQDs/g-C_3N_4 composite system. When illuminated by visible light, the electrons in g-C_3N_4 are transferred into the CQDs, which facilitates the charge separation. At the same time, CQDs have a narrow bandgap that can respond to visible light and provide electrons to the CB of g-C_3N_4, which broadens the visible-light absorption region of the system. Finally, CQDs absorb long-wavelength visible light and emit short-wavelength light, which can excite g-C_3N_4 to generate more carriers. Li et al. fabricated 2D/1D heterojunctions by assembling MoS_2 nanosheets onto ultralong TiO_2 nanofibers [232] (Fig. 19d). This heterostructure shows excellent photocatalytic hydrogen generation activity, which is approximately 24 times higher than that of pure TiO_2. As shown in Fig. 19e, band bending occurs between the interface of TiO_2 nanofibers and MoS_2 nanosheets, which facilitates photogenerated electron transfer to MoS_2 and enhances the photocatalytic activity. Fu et al. prepared ultrathin 2D/2D WO_3/g-C_3N_4 composite heterojunction photocatalysts [233]

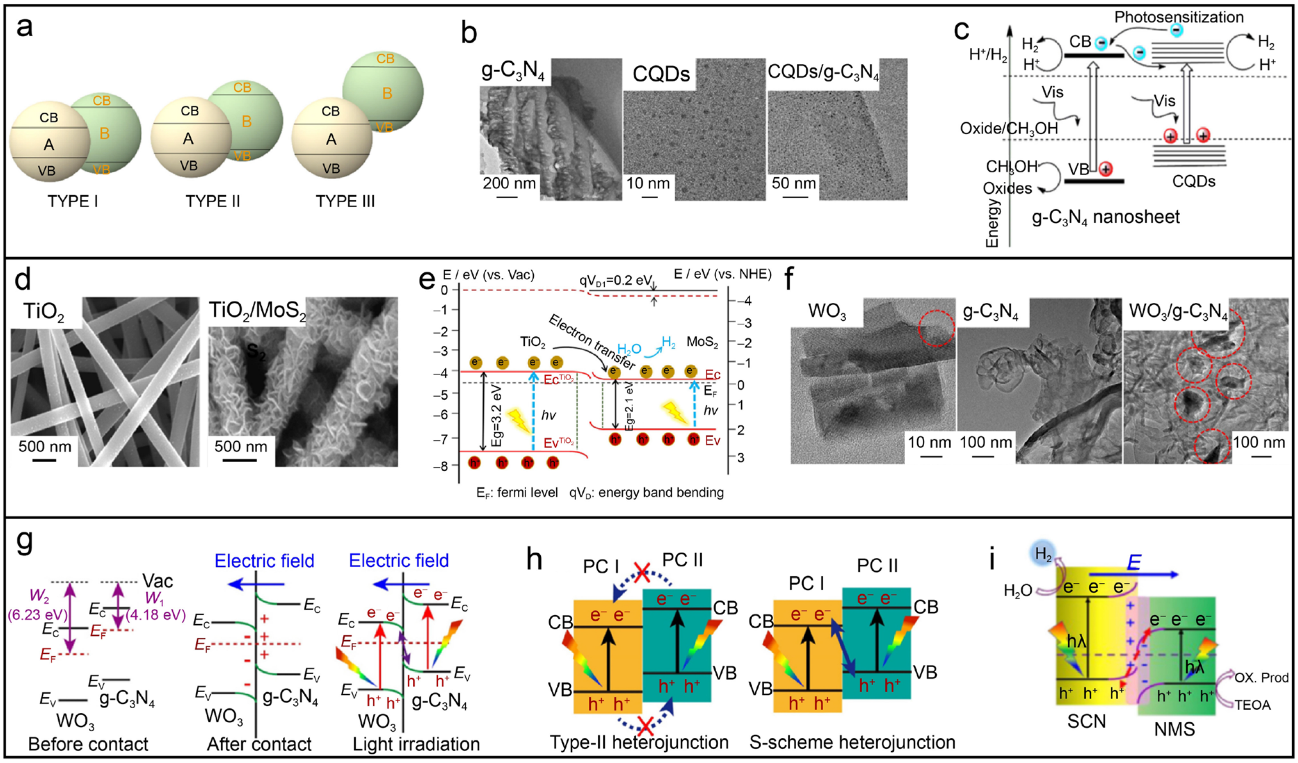

Fig. 19 **a** Schematic diagram of three heterojunction structures. **b** TEM images of g-C_3N_4, CQDs, and CQDs/g-C_3N_4. **c** Schematic diagram of the photocatalytic mechanism of UCN/CQDs. Reproduced with permission from Ref. [231]. Copyright 2016, Elsevier. **d** SEM images of pure TiO_2 nanofibers and TiO_2/MoS_2 composite nanofibers. **e** The band structures of TiO_2/MoS_2 heterostructure. Reproduced with permission from Ref. [232]. Copyright 2020, Elsevier. **f** TEM images of WO_3 nanosheets, g-C_3N_4 nanosheets and WO_3/g-C_3N_4 samples. **g** The band structures of pure g-C_3N_4 and WO_3 before bonding (left), the internal electric field and band-edge bending of the WO_3/g-C_3N_4 interface after bonding (middle), and the schematic diagram of the S-heterojunction charge-transfer process between WO_3 and g-C_3N_4 under illumination (right). **h** the Schematic illustration of type II heterojunction and S-scheme heterojunction. Reproduced with permission from Ref. [233]. Copyright 2019, Elsevier. **i** Schematic illustration of NMS/SCN S-scheme heterojunction. (TEOA: Triethanolamine) Reproduced with permission from Ref. [234]. Copyright 2021, Elsevier

(Fig. 19f). The ultrathin layered heterojunction (Fig. 19g) makes it easier for photogenerated electrons and holes to transfer to the surface of the photocatalyst, which improves the surface photocatalytic rate and exhibits better hydrogen production activity than pure g-C_3N_4 and WO_3. Meanwhile, the heterojunction constructed in this study is a new stepped (S-scheme) heterojunction. Its structure is similar to the type II heterojunction, but the electron transport mode is different, which improves the disadvantage of the weakened carrier oxidation ability in the type II heterojunction. As shown in Fig. 19h, since electrons in CB and holes in VB of the two semiconductors are difficult to transfer due to Coulomb repulsion, and the Coulomb attraction between CB and VB of the same semiconductor hinders the transfer process, the transfer mechanism of the traditional type II heterojunction is thermodynamically unfavorable for the occurrence of photocatalytic oxidation and reduction reactions, which has obvious limitations. The S-type heterojunction can realize the elimination of electrons and holes between CB and VB through the internal electric field between the two semiconductors. Finally, the holes in the VB of semiconductor I and the electrons in the CB of semiconductor II are left to participate in the photocatalytic reaction. Obviously, this system will be more conducive to the separation of photogenerated carriers. Chen et al. also constructed S-type heterojunctions of S-doped g-C_3N_4 (SCN) and N-doped MoS_2 (NMS), and the obtained S-g-C_3N_4/N-MoS_2 photocatalyst has excellent photocatalytic hydrogen evolution performance [234]. The mechanism of charge transfer and separation in S-type heterojunction photocatalysts is shown in Fig. 19i. Under the action of the internal electric field directed from the SCN to the NMS, the holes on the VB of the SCN and the electrons on the CB of the NMS are eliminated, and finally the electrons on the CB of the SCN and the holes on the VB of the NMS are left to participate in subsequent reactions.

Whether it is a Schottky junction constructed by noble metal deposition or a heterojunction constructed between semiconductors, the essential regulation mechanism is to regulate the bandgap structure of the photocatalyst to better promote the transfer of photogenerated carriers. It is not difficult to see that there are two key aspects in the design of photocatalyst heterojunctions, one is to build a suitable two-semiconductor interlaced energy band structure, and the other is to provide an ideal interface for charge separation.

4.4 Thickness adjustment

As mentioned in Sect. 3 of this paper, the morphology of the photocatalyst is different, and its surface area, the number of exposed active sites, the contact area between the catalyst and the reactant, and the adsorption performance of the reactant will be different. Compared with bulk materials, the ultrathin thickness of 2D nanomaterials can provide more active sites and make full use of sunlight. At the same time, the charge transport path can be shortened and the photocatalytic activity can be significantly improved. Many experiments have confirmed that by changing the thickness of the material, it is possible to obtain much higher catalytic performance than the bulk material. That is, adjustment of thickness is an effective means of modification. Ping et al. exfoliated the bulk g-C_3N_4 into g-C_3N_4 nanosheets with a thickness of about 2 nm by thermal oxidation etching, and its photocatalytic activity was significantly improved [235]. This is due to the increased specific surface area after thickness reduction and the quantum confinement effect of ultrathin nanosheets, which enhances the electron transport rate and prolongs the carrier lifetime. In addition to the significant increase in specific surface area, the CB of g-C_3N_4 shifts to a more negative position during the thickness reduction process, making it have a better reducing ability. This will benefit its application in reducing CO_2. Song et al. prepared g-C_3N_4 with different thicknesses by high-temperature exfoliation [236]. As the calcination time increased, the thickness of the obtained g-C_3N_4 became thinner. UV–Vis diffuse reflectance spectroscopy (DRS) spectra indicated that the bandgap of g-C_3N_4 increases with decreasing thickness (Fig. 20a). As shown in Fig. 20b, a more negative CB position would be beneficial for the application of g-C_3N_4 in CO_2 reduction. The experimental characterization results also confirmed this point (Fig. 20c). During experiments, the thickness of 2D materials is usually characterized using

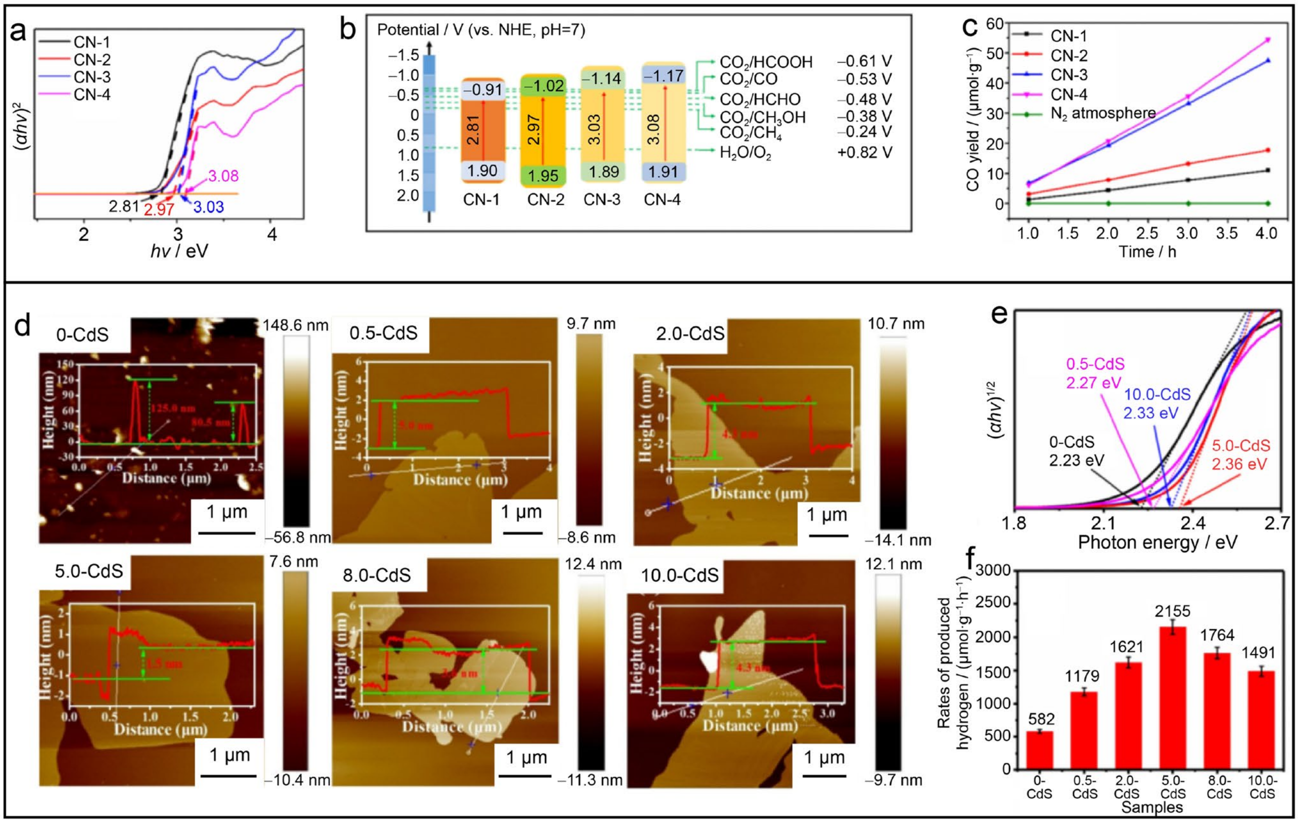

Fig. 20 **a** Tauc plots of different CN samples. **b** Bandgap structure of different CN samples and the reduction potential of some CO_2-derived products. **c** Photocatalytic performance of different CN samples. Reproduced with permission from Ref. [236]. Copyright 2022, Elsevier. **d** AFM images and height cutaway views of different CdS samples. **e** Kubelka–Munk function vs. photon energy curves of different CdS samples. **f** Rates of photocatalytic produced hydrogen of different CdS samples. Reproduced with permission from Ref. [237]. Copyright 2018, Elsevier

AFM. As shown in Fig. 20d, CdS nanosheets with different thicknesses from 1.5 to 5.0 nm were characterized by AFM. Benefiting from the shorter charge transport distance and more negative CB edge (Fig. 20e) brought about by the smaller thickness, the thinnest CdS nanosheet at 1.5 nm has the most excellent catalytic hydrogen evolution performance [237] (Fig. 20f). In addition to thickness, AFM can characterize roughness and surface morphology. Due to the influence of possible attachments on the material and the influence of the substrate itself, the thickness of the material measured by AFM will generally be thicker. Due to equipment limitations, AFM can only characterize small pieces of 2D materials, and the characterization takes a long time, making it impossible to quickly characterize large-area 2D materials. In addition to AFM, the thickness of 2D materials can also be characterized by optical reflection contrast, Raman spectroscopy, photoluminescence, optical interference effects and other methods, which were reviewed in detail by Jin and Yu [238].

4.5 Defect engineering

During the exfoliation of the material from the bulk to the nanosheet, the internal atoms are exposed on the surface of the material, and various defects are inevitably formed. Fortunately, for catalytic processes, the creation of defects is not a disadvantage. Appropriate defects can help build new energy bands and increase active sites, thereby regulating electron capture. Defect engineering is an effective way to improve the light absorption performance of catalysts. By constructing defects, the efficiency of electron–hole separation is enhanced, and the light absorption region is also enlarged. In some experiments, even its photoresponse range was extended to the entire visible-light region. In addition to single defects that can improve catalytic performance, there are also interactions between defects. If this synergy can be exploited, the overall photocatalytic efficiency can also be improved. Due to the layered structure of 2D materials, most of the defects generated in the material are surface defects rather than bulk defects in bulk materials. This feature avoids the disadvantage of bulk defects becoming carrier recombination centers, and more shows the side that is helpful for photocatalysis. Wang et al. prepared an oxygen vacancy (OV)-rich ultrathin sulfur-doped BiOBr nanosheet with excellent 4-chlorophenol degradation performance [239]. As shown in Fig. 21a, there exists a sub-band at 0.38 eV below the CBM. The partial density of states (PDOS) further reveals that the sub-band is composed of Bi 6p state and S 2p state, and the Bi 6p state mainly originate from the Bi atoms nearest to the OVs (Fig. 21b). That is, this sub-band is generated by the synergy between oxygen vacancies and sulfur doping. Figure 21c shows how the sub-bands participate in the degradation process. The generation of sub-bands effectively narrows the bandgap and improves the visible-light absorption capacity. Niu et al. obtained porous g-C_3N_4 (CN) with a large number of defects (CNQ) by a simple heat treatment in air (Fig. 21d) [240]. As shown in Fig.21e, compared with pristine g-C_3N_4, the bandgaps of CNQ samples are all reduced, implying the generation of new sub-bands (Fig. 21f). The new peak at 2,175 cm^{-1} in the FTIR spectrum corresponds to the appearance of the cyano group (–CN) that can disrupt the stacking structure and cause layer fluctuations (Fig. 21g). Figure 21h, i reveals the appearance of NVs after rapid thermal treatment. The above characterizations confirmed that the appearance of –CN and NVs caused by heat treatment was the cause of the structural changes.

In the investigation of the electronic structure changes caused by defects, the calculation of the DOS by DFT is an effective method to explore the influence of defects. Figure 21j is the DOS calculation for pristine h-BN, h-BN with boron vacancies, h-BN with NVs, and h-BN with oxygen-filled nitrogen vacancy [241]. The analysis shows that pristine h-BN has a wide bandgap of 5.42 eV, which is not conducive to the photoresponse. The band structure of h-BN with boron vacancies has changed greatly, and the mid-gap states has expanded beyond the Fermi level, making it an excellent electron acceptor similar to p-type semiconductors. Meanwhile, h-BN with NVs and h-BN with oxygen-filled nitrogen vacancy is a good electron donor similar to n-type semiconductors . Research has proved that the ubiquitous defects in materials affect the electrical, thermal, optical, magnetic, acoustic and mechanical properties of materials. The catalytic process is very sensitive to the change of electronic structure, so the introduction of defects is an effective means of catalytic modification. First, defects can form additional energy levels to expand the photoresponse range, and second, defects can affect and change the distribution of catalytic active sites and charge density, thereby changing the catalytic activity of the catalyst. However, due to the complexity and diversity of defects, the concentration, distribution, types of defects, and the interaction between different defects have not been systematically studied. But it is worth looking forward to, with the rapid development of computer technology and material characterization methods, the mechanism of defects in the catalytic process will be further revealed.

4.6 Dye sensitization

Dye sensitization is a method to expand the light absorption range by adsorbing dyes that can absorb various visible light and even near-infrared light on the semiconductor surface. When the dye is irradiated with visible light, electrons on the dye will transition from the ground state to the excited state. When the free electron potential of the excited state

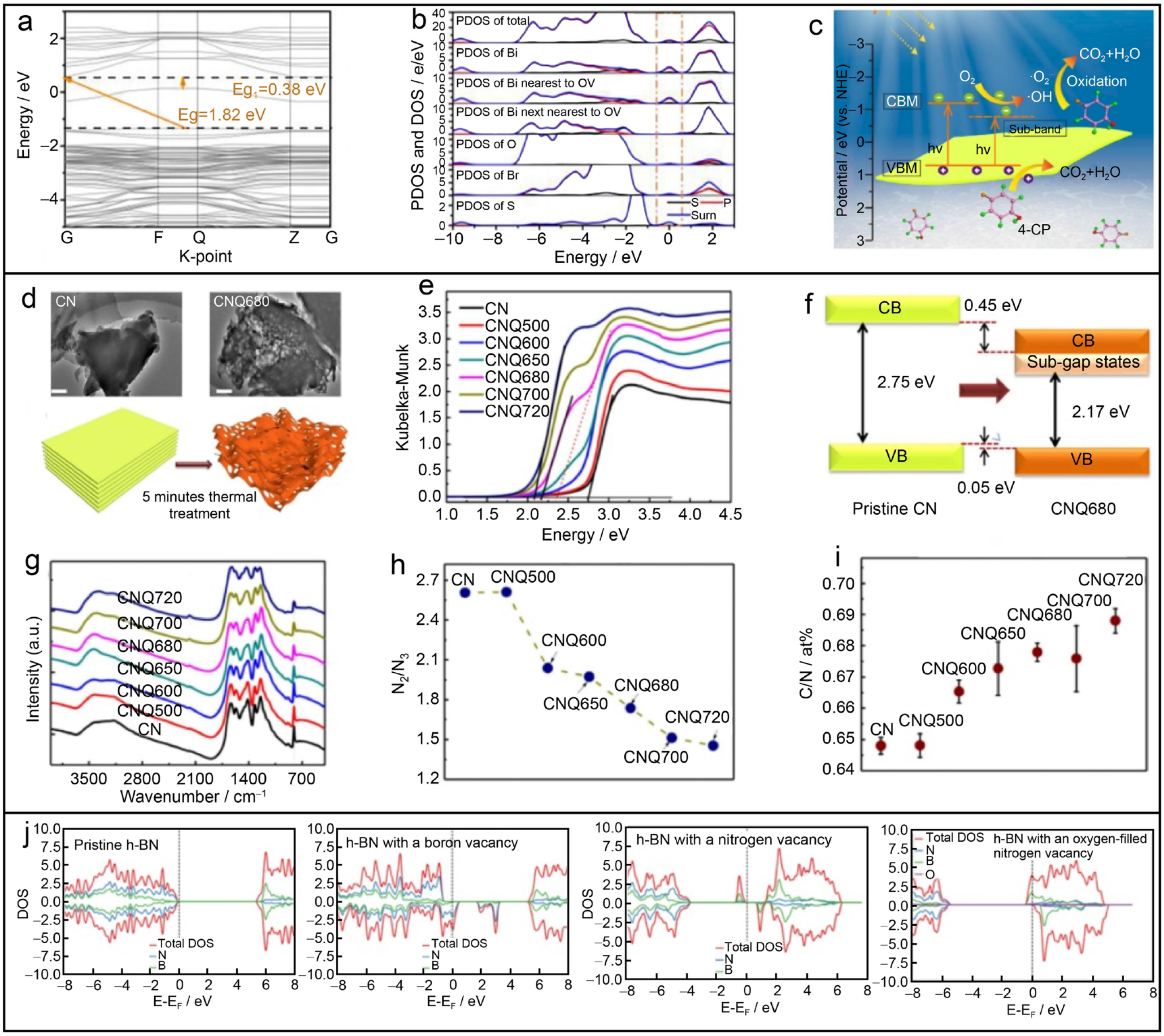

Fig. 21 **a** Band structure of OV-rich ultrathin S-doped BiOBr nanosheet. **b** PDOS of OV-rich ultrathin S-doped BiOBr nanosheet. **c** Schematic diagram of the photocatalytic degradation 4-CP over OV-rich ultrathin S-doped BiOBr nanosheet. Reproduced with permission from Ref. [239]. Copyright 2019, Elsevier. **d** The typical TEM images of CN and CNQ680 and the schematic diagram of the morphology change from CN to CNQ. **e** The converted Kubelka–Munk vs. light energy plots of CN and CNQs. **f** Schematic diagram of band structure change from CN to CNQ680. **g** The FTIR spectra of CN and CNQs. **h** the $(N_{2c})/(N_{3c})$ ratio of CN and CNQs. **i** The C/N ratio of CN and CNQs. Reproduced with permission from Ref. [240]. Copyright 2017, Elsevier. **j** The total and atomic projected DOS analyses of different h-BN samples. Reproduced with permission from Ref. [241]. Copyright 2021, ACS Publications

dye is higher than the potential of the CB of the semiconductor photocatalyst, electrons will be transferred from the dye to the semiconductor and react with O_2 to generate active radicals. At the same time, the dye itself becomes a positive ion radical. The schematic diagram of the reaction process of dye sensitization is shown in Fig. 22a [242]. The unique layered structure of 2D nanomaterials provides convenience for the adsorption of dye sensitizers. At the same time, the changeable structure of 2D nanomaterials has higher flexibility and can better combine with different dyes to expand the range of light absorption and enhanced charge-transfer rate. Li et al. loaded three different dye sensitizers: BY24, BR14, and MB on porous Cu-MOFs, resulting in composites basic yellow 24 (BY24@1), basic red 14 (BR14@1), and MB@1 [243]. It can be seen that the energy bandgaps of the three composites are respectively reduced to 2.19 eV, 2.10 eV and 1.76 eV (Fig. 22b). Due to the significantly enhanced visible-light response range, MB @1 with the narrowest bandgap shows the best catalytic performance. Li et al. found that dye sensitization can effectively inject

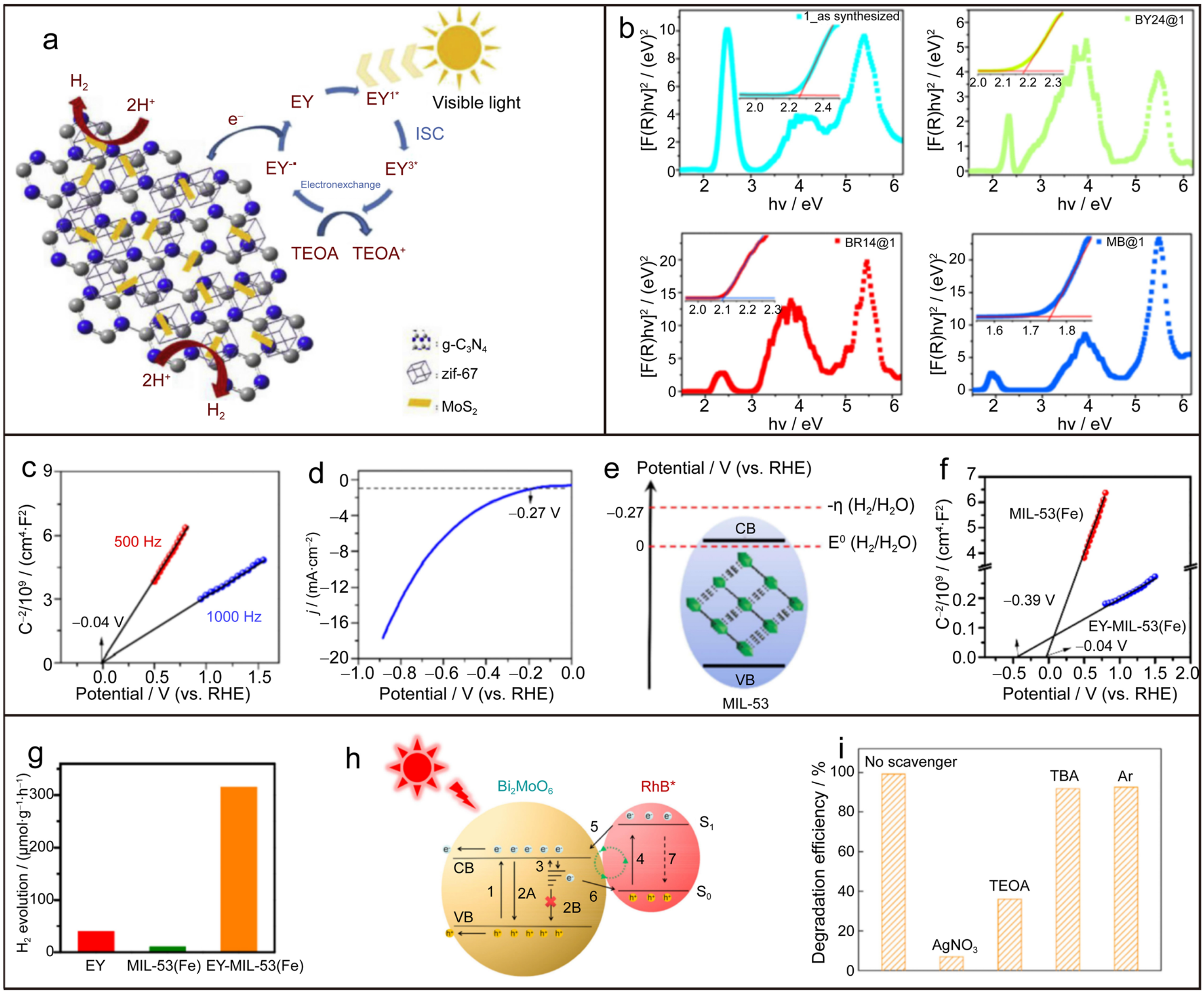

Fig. 22 **a** Schematic diagram of the dye-sensitized electron transfer process. Reproduced with permission from Ref. [242]. Copyright 2018, Elsevier. **b** energy bandgaps of different samples. Reproduced with permission from Ref. [243]. Copyright 2019, Academic Press Inc. **c** M–S plots of MIL-53 (Fe). **d** LSV curve of MIL-53 (Fe) for HER. **e** Illustration of band structure of MIL-53 (Fe). **f** M–S plots of EY-sensitized MIL-53 (Fe). **g** Photocatalytic hydrogen evolution activity of different samples. Reproduced with permission from Ref. [244]. Copyright 2022, Elsevier. **h** The photoexcited charge-transfer processes that may occur in the Bi$_2$MoO$_6$@RhB samples: 1. direct bandgap transition; 2. intrinsic charge recombination; 3. electron trapping/detrapping; 4. intramolecular photoexcitation; 5. interfacial electron injection; 6. interfacial electron recombination; 7. radiationless decay. **i** sacrificial agent experiments over Bi$_2$MoO$_6$@RhB under LED light irradiation. (TBA: tert-Butanol) Reproduced with permission from Ref. [245]. Copyright 2023, Elsevier

electrons into Fe-MOFs (MIL-53), and increase its quasi-Fermi level under light, so that Fe-MOFs can participate in photocatalytic hydrogen evolution [244]. Figure 22c shows that the CBM of MIL-53 is about − 0.04 V, which is in the range of hydrogen evolution potential from the thermodynamic point of view. However, linear sweep voltammetry (LSV) characterization revealed that MIL-53 had an onset overpotential of 0.27 V, implying a kinetic barrier for HER (Fig. 22d). Therefore, as shown in Fig. 22e, the CBM at − 0.04 V cannot provide enough energy for the HER reaction. After the introduction of eosin Y (EY) by dye sensitization, the CBM position was significantly more negative enough to overcome the onset potential of 0.27 V (Fig. 22f). Therefore, EY-MIL-53 has shown significantly better performance than MIL-53 in catalytic hydrogen evolution (Fig. 22g). Wei et al. revealed two contributions to the photocatalytic process by the electrons generated after the dye was excited in the Bi$_2$MoO$_6$@RhB system [245]. One is that electrons are injected into the CB of Bi$_2$MoO$_6$ to participate in the reduction reaction, and the other is to suppress the recombination of carriers in the VB of Bi$_2$MoO$_6$ through the “4–5–6 cycle” shown in Fig. 22h. The sacrificial agent detection experiment found that the degradation activity decreased significantly when $AgNO_3$ which eliminates electrons or triethanolamine (TEOA) which eliminates holes was added. This shows that electrons and holes are directly involved in the process of degrading levofloxacin (Fig. 22i).

In summary, dye sensitization is an effective modification method that can change the bandgap structure, broaden the photoresponse, and help photocatalysts overcome the kinetic barrier by injecting electrons. In the actual experiment process, how to effectively adsorb the dye on the surface of the material is an important process. The rich surface defects of 2D materials allow dyes to be adsorbed on the surface through a simple electrostatic self-assembly process. In order to further obtain better adsorption, the adsorption can also be promoted by means of light or an external electric field.

5 Conclusions and prospects

With the development of industry, environmental and energy challenges emerge one after another, and it is a global issue to explore how to solve these two problems. Photocatalysis has become the most potential technology to solve environmental and energy problems due to its green and low-cost characteristics. As the core medium of photocatalytic technology, semiconductor photocatalyst, how to modify it and improve its photocatalytic performance has become the focus of research.

Traditional semiconductor materials have a large bandgap, narrow light absorption range, and low separation and migration efficiency of photogenerated carriers, which are limited in practical applications and have insufficient reaction sites. 2D nanomaterials play an important role in the field of photocatalysis due to the unique effects brought about by their nanometer size and layered structure, bringing unprecedented opportunities for improving photocatalytic activity. The main modification methods of semiconductor photocatalysts include element doping, noble metal deposition, heterostructure construction, thickness adjustment, defect engineering, and dye sensitization. Due to the sensitivity of 2D nanomaterials to thickness changes, the modification process is more convenient than bulk materials, and the above modification methods can also play a more significant and effective role in 2D nanomaterial systems. The wide variety of 2D nanomaterial families with rich atomic structure and high flexibility also provides more new ideas for designing photocatalysts. However, the practical use of 2D nanomaterials is limited for the following reasons:

(1) 2D nanomaterials have high surface energy, abundant active sites, easy agglomeration and chemical changes, and lack of long-term stability and durability, which limits their practical application;
(2) At present, the production and preparation of 2D photocatalytic nanomaterials mainly centralized in the laboratory, low-cost, environmentally friendly mass production remains challenging;
(3) The relationship between the surface structure of 2D nanomaterials and its photocatalytic activity is close, and the mechanism of the reaction process is complex, which needs to be explored with the help of a large number of microscopic characterization methods.

In the face of nanoscale and low-latitude photocatalysts, which are difficult to observe the microscopic reaction process, researchers can look forward to two directions:

(1) Development of *in-situ* characterization technology. Compared with *ex-situ* characterization technology, *in-situ* characterization technology can intuitively obtain the intermediate process of material changes in the reaction, and obtain information related to transient reactions, such as atomic structure, element arrangement, surface defects, and molecular adsorption. *In-situ* characterization technology is an indispensable means to explore the catalytic mechanism of catalysts. At present, many *in-situ* characterization methods such as *in-situ* infrared, *in-situ* Raman, *in-situ* XPS, and *in-situ* synchrotron radiation techniques have been used in the study of photocatalytic reaction mechanisms, making important contributions to catalyst design. It is foreseeable that in the future, with the proficient analysis of existing *in-situ* characterization techniques and the further development of *in-situ* characterization techniques, the structure of 2D nanophotocatalysts will be accurately understood, and researchers will design and prepare more applicable for practical catalyst systems;
(2) The development of computer simulation technology, such as first-principles calculation and so on. Computer simulation can start from the electronic structure of the material itself, and quantitatively analyze the fundamental relationship between photocatalyst modification methods and performance improvement. With further simulation studies on the four main steps of the photocatalytic reaction: visible-light absorption, carrier separation, carrier transport and redox reaction, researchers can more accurately simulate the theoretically optimal material system, morphology and structure, thus providing guidance for the stable and efficient production of industrial 2D nanophotocatalysts.

In the future, while focusing on catalytic performance and stability, it is necessary to further pay attention to the research on the environmental protection, cost and life of photocatalysts, so that photocatalytic technology can become a powerful means to solve environmental and energy problems. In summary, although there are still some challenges in the application of 2D nanomaterials in the field of photocatalysis, it is undeniable that with the deepening of research, more new 2D photocatalytic nanomaterials will be designed and prepared, and 2D nanophotocatalysts will become the mainstream catalyst in the field of photocatalysis.

Acknowledgements This work was supported by the National Natural Science Foundation of China Youth Program (52204399), the Postdoctoral Research Foundation of China (2021MD703866), the Scientific and Technological Innovation Team Project of Shaanxi Innovation Capability Support Plan (2022TD-30), Youth Innovation Team of Shaanxi Universities (2019-2022), Fok Ying Tung Education Foundation (171101), Natural Science Basic Research Program of Shaanxi Province (2022JQ-478), the Scientific Research Program of Youth Innovation Team of Shaanxi (22JP037), the Science and Technology Project of Universities and Institutes Staff Serving Enterprises in Xi'an (22GXFW0059) and Top Young Talents Project of “Special Support Program for High Level Talents” in Shaanxi Province (2018-2023).

Data availability The raw/proceeded data can be provided from the corresponding authors on the reasonable request.

Declarations

Conflict of interest The authors declare no conflict of interest.

References

1. Zhu D, Zhou Q. Action and mechanism of semiconductor photocatalysis on degradation of organic pollutants in water treatment: a review. Environ Nanotechnol Monit Manag. 2019;12:100255.
2. Kudo A, Miseki Y. Heterogeneous photocatalyst materials for water splitting. Chem Soc Rev. 2009;38(1):253.
3. Loeb SK, Alvarez PJJ, Brame JA, Cates EL, Choi W, Crittenden J, Dionysiou DD, Li QL, Li PG, Quan X, Sedlak DL, Waite TD, Westerhoff P, Kim JH. The technology horizon for photocatalytic water treatment: sunrise or sunset? Environ Sci Technol. 2019;53(6):2937.
4. Lee CM, Palaniandy P, Dahlan I. Pharmaceutical residues in aquatic environment and water remediation by TiO_2 heterogeneous photocatalysis: a review. Environ Earth Sci. 2017;76(17):1.
5. Chairungsri W, Subkomkaew A, Kijjanapanich P, Chimupala Y. Direct dye wastewater photocatalysis using immobilized titanium dioxide on fixed substrate. Chemosphere. 2022;286:131762.
6. Guo SH, Li XH, Li J, Wei BQ. Boosting photocatalytic hydrogen production from water by photothermally induced biphase systems. Nat Commun. 2021;12(1):1343.
7. Wang Z, Li C, Domen K. Recent developments in heterogeneous photocatalysts for solar-driven overall water splitting. Chem Soc Rev. 2019;48(7):2109.
8. Puga AV. Photocatalytic production of hydrogen from biomass-derived feedstocks. Coord Chem Rev. 2016;315:1.
9. Li JL, Zhang M, Guan ZJ, Li QY, He CQ, Yang JJ. Synergistic effect of surface and bulk single-electron-trapped oxygen vacancy of TiO_2 in the photocatalytic reduction of CO_2. Appl Catal B Environ. 2017;206:300.
10. Zhang XD, Kim D, Yan J, Lee LYS. Photocatalytic CO_2 reduction enabled by interfacial S-scheme heterojunction between ultrasmall copper phosphosulfide and g-C_3N_4. ACS Appl Mater Interfaces. 2021;13(8):9762.
11. Hirakawa H, Hashimoto M, Shiraishi Y, Hirai T. Photocatalytic conversion of nitrogen to ammonia with water on surface oxygen vacancies of titanium dioxide. JACS. 2017;139(31):10929.
12. Feng YL, Zhang ZS, Zhao K, Lin SL, Li H, Gao X. Photocatalytic nitrogen fixation: oxygen vacancy modified novel micro-nanosheet structure $Bi_2O_2CO_3$ with band gap engineering. J Colloid Interface Sci. 2021;583:499.
13. Abdelsalam EM, Mohamed YMA, Abdelkhalik S, El Nazer HA, Attia YA. Photocatalytic oxidation of nitrogen oxides (NO_x) using Ag- and Pt-doped TiO_2 nanoparticles under visible light irradiation. Environ Sci Pollut Res. 2020;27:35828.
14. Attia YA, Mohamed YMA, Awad MM, Alexeree S. Ag doped ZnO nanorods catalyzed photo -triggered synthesis of some novel (1H-tetrazol-5-yl)-coumarin hybrids. J Organomet Chem. 2020;919:121320.
15. Fujishima A, Honda K. Electrochemical photolysis of water at a semiconductor electrode. Nature. 1972;238(5358):37.
16. Carey JH, Lawrence J, Tosine HM. Photodechlorination of PCB’s in the presence of titanium dioxide in aqueous suspensions. B Environ Contam Toxicol. 1976;16:697.
17. Schrauzer GN, Guth TD. Photolysis of water and photoreduction of nitrogen on titanium-dioxide. ChemInform. 2002;99(22):7189.
18. Yang T, Peng J, Yun Z, Xuan H, Fu X. Enhanced photocatalytic ozonation degradation of organic pollutants by ZnO modified TiO_2 nanocomposites. Appl Catal B Environ. 2018;221:223.
19. Chen X, Mao SS. Titanium dioxide nanomaterials: synthesis, properties, modifications, and applications. Chem Rev. 2007;107(7):2891.
20. Katal R, Masudy PS, Tanhaei M, Farahani M, Hu JY. A review on the synthesis of the various types of anatase TiO_2 facets and their applications for photocatalysis. Chem Eng J. 2020;384:123384.
21. Hoffmann MR, Martin ST, Choi W, Bahnemann DW. Environmental applications of semiconductor photocatalysis. Chem Rev. 1995;95(1):69.
22. Ren HT, Ge L, Guo Q, Li L, Hu GK, Li JG. The enhancement of photocatalytic performance of $SrTiO_3$ nanoparticles via combining with carbon quantum dots. RSC Adv. 2018;8(36):20157.
23. Fu SL, Chen XH, Liu P. Preparation of CNTs/Cu composites with good electrical conductivity and excellent mechanical properties. Mater Sci Eng A. 2020;771:138656.
24. Lin JX, Huang YJ, Wang S, Chen GH. Microwave-assisted rapid exfoliation of graphite into graphene by using ammonium bicarbonate as the intercalation agent. Ind Eng Chem Res. 2017;56(33):9341.
25. Hou DD, Li K, Ma RJ, Liu QF. Influence of order degree of coaly graphite on its structure change during preparation of graphene oxide. J Materiomics. 2020;6(3):628.
26. Li N, Kong ZZ, Chen XZ, Yang YF. Research progress of novel two-dimensional materials in photocatalysis and electrocatalysis. J Inorg Mater. 2020;35(7):735.
27. Bonaccorso F, Colombo L, Yu G, Stoller M, Tozzini V, Ferrari AC, Ruoff RS, Pellegrini V. Graphene, related two-dimensional crystals, and hybrid systems for energy conversion and storage. Science. 2015;347(6217):1246501.
28. Feng CY, Wu ZP, Huang KW, Ye JH, Zhang HB. Surface modification of 2D photocatalysts for solar energy conversion. Adv Mater. 2022;34(23):2200180.
29. Wang H, Zhang XD, Xie Y. Recent progress in ultrathin two-dimensional semiconductors for photocatalysis. Mater Sci Eng R Rep. 2018;130:1.
30. Di J, Yan C, Handoko AD, Seh ZW, Li HM, Liu Z. Ultrathin two-dimensional materials for photo- and electrocatalytic hydrogen evolution. Mater Today. 2018;21(7):749.

31. Luo B, Liu G, Wang LZ. Recent advances in 2D materials for photocatalysis. Nanoscale. 2016;8(13):6904.
32. Li Y, Gao C, Long R, Xiong Y. Photocatalyst design based on two-dimensional materials. Mater Today Chem. 2019;11:197.
33. Qian WQ, Xu SW, Zhang XM, Li CB, Yang WY, Bowen CR, Yang Y. Differences and similarities of photocatalysis and electrocatalysis in two-dimensional nanomaterials: strategies, traps, applications and challenges. Nano Micro Lett. 2021;13:1.
34. Bakardjieva S, Fajgar R, Jakubec I, Koci E, Zhigunov A, Chatzisymeon E, Davididou K. Photocatalytic degradation of bisphenol A induced by dense nanocavities inside aligned 2D-TiO_2 nanostructures. Cata Today. 2019;328:189.
35. Segovia M, Alegria M, Aliaga J, Celedon S, Ballesteros L, Sotomayor TC, Gonzalez G, Benavente E. Heterostructured 2D ZnO hybrid nanocomposites sensitized with cubic Cu_2O nanoparticles for sunlight photocatalysis. J Mater Sci. 2019;54:13523.
36. Ren JK, Innocenzi P. 2D boron nitride heterostructures: recent advances and future challenges. Small Struct. 2021;2(11):2100068.
37. Feng CY, Tang L, Deng YC, Zeng GM, Wang JJ, Liu YN, Chen ZM, Yu JF, Wang JJ. Enhancing optical absorption and charge transfer: synthesis of S-doped h-BN with tunable band structures for metal-free visible-light-driven photocatalysis. Appl Catal B Environ. 2019;256:117827.
38. Voiry D, Yang J, Chhowalla M. Recent strategies for improving the catalytic activity of 2D TMD nanosheets toward the hydrogen evolution reaction. Adv Mater. 2016;28(29):6197.
39. Cao SW, Low JX, Yu JG, Jaroniec M. Polymeric photocatalysts based on graphitic carbon nitride. Adv Mater. 2015;27(13):2150.
40. Tang RD, Gong DX, Zhou YY, Deng YC, Feng CY, Xiong S, Huang Y, Peng GW, Li L. Unique g-C_3N_4/PDI-g-C_3N_4 homojunction with synergistic piezo-photocatalytic effect for aquatic contaminant control and H_2O_2 generation under visible light. Appl Catal B Environ. 2022;303:120929.
41. Wen M, Wang JH, Tong RF, Liu DN, Huang H, Yu Y, Zhou ZK, Chu PK, Yu XF. A low-cost metal-free photocatalyst based on black phosphorus. Adv Sci. 2019;6(1):1801321.
42. Zhang GH, Zhang XQ, Meng Y, Pan GX, Ni ZM, Xia SJ. Layered double hydroxides-based photocatalysts and visible-light driven photodegradation of organic pollutants: a review. Chem Eng J. 2020;392:123684.
43. Sun DR, Li ZH. Robust Ti- and Zr-based metal-organic frameworks for photocatalysis. Chinese J Chem. 2017;35(2):135.
44. Novoselov KS, Geim AK, Morozov SV, Jiang D, Zhang Y, Dubonos SV, Grigorieva IV, Firsov AA. Electric field effect in atomically thin carbon films. Science. 2004;306(5696):666.
45. Geng DS, Chen Y, Chen YG, Li YL, Li RY, Sun XL, Ye SY, Knights S. High oxygen-reduction activity and durability of nitrogen-doped graphene. Energy Environ Sci. 2011;4(3):760.
46. Li M, Yin B, Gao C, Guo J, Zhao C, Jia C, Guo X. Graphene: preparation, tailoring, and modification. Exploration. 2023;3(1):20210233.
47. Zhu Y, Murali S, Cai W, Li X, Ji WS, Jeffrey RP, Ruoff RS. Graphene and graphene oxide: synthesis, properties, and applications. Adv Mater. 2010;22(35):3906.
48. Zhang J, Yang Y, Huang X, Shan Q, Wu W. Novel preparation of high-yield graphene and graphene/ZnO composite. J Alloys Compd. 2021;875:160024.
49. Huang Y, Shen YY, Qin XL, Wang K. Enhancing visible-light photocatalytic activity by strongly binding flake $BiFeO_3$ nanoparticles on graphene sheets. Micro Nano Lett. 2020;15(11):755.
50. Zhang H, Gu QQ, Zhou YW, Liu SQ, Liu WX, Luo L, Meng ZD. Direct Z-scheme photocatalytic removal of ammonia via the narrow band gap MoS_2/N-doped graphene hybrid catalyst upon near-infrared irradiation. Appl Surf Sci. 2020;504:144065.
51. Yang X, Cui J, Liu X, Zhang Q, Wang D, Ye J, Liu L. Boosting photocatalytic overall water splitting over single-layer graphene coated metal cocatalyst. Appl Catal B Environ. 2023;325:122369.
52. Qiu D, He CL, Lu YX, Li QD, Chen Y, Cui XL. Assembling gamma-graphyne surrounding TiO_2 nanotube arrays: an efficient p-n heterojunction for boosting photoelectrochemical water splitting. Dalton Trans. 2021;50(42):15422.
53. Wu LL, Li QD, Yang CF, Chen Y, Dai ZQ, Yao BY, Zhang XY, Cui XL. Ternary TiO_2/$MoSe_2$/gamma-graphyne heterojunctions with enhanced photocatalytic hydrogen evolution. J Mater Sci Mater Electron. 2020;31(11):8796.
54. Carvalho A, Costa MCF, Marangoni VS, Ng PR, Nguyen TLH, Neto AHC. The degree of oxidation of graphene oxide. Nanomaterials. 2021;11(3):560.
55. Luo ZT, Vora PM, Mele EJ, Johnson ATC, Kikkawa JM. Photoluminescence and band gap modulation in graphene oxide. Appl Phys Lett. 2009;94(11):111909.
56. Yeh TF, Syu JM, Cheng C, Chang TH, Teng H. Graphite oxide as a photocatalyst for hydrogen production from water. Adv Funct Mater. 2010;20(14):2255.
57. Meng AY, Zhang LY, Cheng B, Yu JG. Dual cocatalysts in TiO_2 photocatalysis. Adv Mater. 2019;31(30):1807660.
58. Chen J, Wang MG, Han J, Guo R. TiO_2 nanosheet/NiO nanorod hierarchical nanostructures: p-n heterojunctions towards efficient photocatalysis. J Colloid Interface Sci. 2020;562:313.
59. Fragua DM, Abargues R, Rodriguez CPJ, Sanchez RJF, Agouram S, Martinez PJP. Au-ZnO nanocomposite films for plasmonic photocatalysis. Adv Mater Interfaces. 2015;2(11):1500156.
60. Das A, Malakar P, Nair RG. Engineering of ZnO nanostructures for efficient solar photocatalysis. Mater Lett. 2018;219:76.
61. Kandasamy M, Seetharaman A, Sivasubramanian D, Nithya A, Jothiyenkatachalam K, Maheswari N, Gopalan M, Dillibabu S, Eftekhari A. Ni-Doped SnO_2 nanoparticles for sensing and photocatalysis. ACS Appl Mater Interfaces. 2018;1(10):5823.
62. Zhan HQ, Deng C, Shi XL, Wu CQ, Li XH, Xie ZP, Wang CA, Chen ZG. Correlation between the photocatalysis and growth mechanism of SnO_2 nanocrystals. J Phys D. 2020;53(15):154005.
63. Adhikari S, Sarkar D, Madras G. Highly efficient WO_3-ZnO mixed oxides for photocatalysis. RSC Adv. 2015;5(16):11895.
64. Shen ZG, Zhao ZY, Qian JW, Peng ZJ, Fu XL. Synthesis of WO_{3-x} nanomaterials with controlled morphology and composition for highly efficient photocatalysis. J Mater Res. 2016;31(8):1065.
65. Wang C, Huang ZX. Controlled synthesis alpha-Fe_2O_3 nanostructures for efficient photocatalysis. Mater Lett. 2016;164:194.
66. Wang F, Song LX, Teng Y, Xia J, Xu ZY, Wang WP. Synthesis, structure, magnetism and photocatalysis of alpha-Fe_2O_3 nanosnowflakes. RSC Adv. 2019;9(61):35372.
67. Li N, Zhang W, Wang DL, Li GX, Zhao Y. Synthesis and applications of TiO_2-based nanostructures as photocatalytic materials. Chem Asian J. 2022;17(23):202200822.
68. Sakai N, Ebina Y, Takada K, Sasaki T. Electronic band structure of titania semiconductor nanosheets revealed by electrochemical and photoelectrochemical studies. JACS. 2004;126(18):5851.
69. Liu YF, Yu ZR, Guo SS, Yao LL, Sun RZ, Huang XY, Zhao WR. Photocatalytic nitrogen fixation on transition metal modified TiO_2 nanosheets under simulated sunlight. New J Chem. 2020;44(45):19924.
70. Wang J, Xia Y, Dong Y, Chen R, Xiang L, Komarneni S. Defect-rich ZnO nanosheets of high surface area as an efficient visible-light photocatalyst. Appl Catal B Environ. 2016;192:8.
71. Zhang L, Lian J, Wu L, Duan Z, Jiang J, Zhao L. Synthesis of a thin-layer MnO_2 nanosheet-coated Fe_3O_4 nanocomposite as a magnetically separable photocatalyst. Langmuir. 2014;30(23):7006.

72. Xu WS, Kozawa DC, Zhou YQ, Wang YZ, Sheng YW, Jiang T, Strano MS, Warner JH. Controlling photoluminescence enhancement and energy transfer in WS_2:hBN:WS_2 vertical stacks by precise interlayer distances. Small. 2020;16(3):1905985.
73. Roy S, Zhang X, Puthirath AB, Meiyazhagan A, Bhattacharyya S, Rahman MM, Babu G, Susarla S, Saju SK, Tran MK, Sassi LM, Saadi M, Lai JW, Sahin O, Sajadi SM, Dharmarajan B, Salpekar D, Chakingal N, Baburaj A, Shuai XT, Adumbumkulath A, Miller KA, Gayle JM, Ajnsztajn A, Prasankumar T, Harikrishnan VVJ, Ojha V, Kannan H, Khater AZ, Zhu ZW, Iyengar SA, Autreto PAD, Oliveira EF, Gao GH, Birdwell AG, Neupane MR, Ivanov TG, Taha TJ, Yadav RM, Arepalli S, Vajtai R, Ajayan PM. Structure, properties and applications of two-dimensional hexagonal boron nitride. Adv Mater. 2021;33(44):2101589.
74. Moon S, Kim J, Park J, Im S, Kim J, Hwang I, Kim JK. Hexagonal boron nitride for next-generation photonics and electronics. Adv Mater. 2023;35(4):2204161.
75. Angizi S, Alem SAA, Azar MH, Shayeganfar F, Manning MI, Hatamie A, Pakdel A, Simchi A. A comprehensive review on planar boron nitride nanomaterials: from 2D nanosheets towards 0D quantum dots. Prog Mater Sci. 2022;124:100884.
76. Meng SG, Ye XJ, Ning XF, Xie ML, Fu XL, Chen SF. Selective oxidation of aromatic alcohols to aromatic aldehydes by BN/metal sulfide with enhanced photocatalytic activity. Appl Catal B Environ. 2016;182:356.
77. Zhang J, Tan BY, Zhang X, Gao F, Hu YX, Wang LF, Duan XM, Yang ZH, Hu P. Atomically thin hexagonal boron nitride and its heterostructures. Adv Mater. 2021;33(6):2000769.
78. Wang XY, Liu ZJ, Shi XQ, Jia YF, Zhu GQ, Peng JH, Wang QZ. Optical and photocatalytic characteristics of Se-doped h-boron nitride: experimental assessments and DFT calculations. J Alloys Compd. 2022;909:164791.
79. Zhao G, Wang Z, He WD, Xing YP, Xu XJ. 2D new nonmetal photocatalyst of sulfur-doped h-BN nanosheeets with high photocatalytic activity. Adv Mater Interfaces. 2019;6(7):1900062.
80. He Z, Kim C, Lin LH, Jeon TH, Lin S, Wang XC, Choi W. Formation of heterostructures via direct growth CN on h-BN porous nanosheets for metal-free photocatalysis. Nano Energy. 2017;42:58.
81. Bevilacqua A, Köhler MH, Azevedo S, Baierle RJ. Stability, and optical and electronic properties of ultrathin h-BNC. Phys Chem Chem Phys. 2017;19(7):5629.
82. Li Q, Hou XM, Fang Z, Yang T, Chen JH, Cui XZ, Liang TX, Shi JL. Construction of layered h-BN/TiO_2 hetero-structure and probing of the synergetic photocatalytic effect. Sci China Mater. 2020;63(2):276.
83. Wang T, Liu XQ, Men QY, Ma CC, Liu Y, Liu Z, Huo PW, Li CX, Yan YS. Green synthesis g-C_3N_4 quantum dots loading h-BN for efficient and stable photocatalytic performance. J Mol Liq. 2018;268:561.
84. Yang RJ, Fan YY, Zhang YF, Mei L, Zhu RS, Qin JQ, Hu JG, Chen ZX, Ng YH, Voiry D, Li S, Lu QY, Wang Q, Yu JC, Zeng ZY. 2D transition metal dichalcogenides for photocatalysis. Angew Chem Int Ed. 2023;62(13):202218016.
85. Wang QH, Kalantar ZK, Kis A, Coleman JN, Strano MS. Electronics and optoelectronics of two-dimensional transition metal dichalcogenides. Nat Nanotechnol. 2012;7(11):699.
86. Altavilla C, Sarno M, Ciambelli P. A novel wet chemistry approach for the synthesis of hybrid 2D free-floating single or multilayer nanosheets of MS_2@oleylamine (M=Mo, W). Chem Mater. 2011;23(17):3879.
87. Chhowalla M, Voiry D, Yang JE, Shin HS, Loh KP. Phase-engineered transition-metal dichalcogenides for energy and electronics. Mrs Bull. 2015;40(7):585.
88. Wei ZM, Li B, Xia CX, Cui Y, He J, Xia JB, Li JB. Various structures of 2D transition-metal dichalcogenides and their applications. Small Methods. 2018;2(11):1800094.
89. Rahmanian E, Malekfar R, Pumera M. Nanohybrids of two-dimensional transition-metal dichalcogenides and titanium dioxide for photocatalytic applications. Chem Eur J. 2018;24(1):18.
90. Wang Z, Tang MT, Cao A, Chan K, Nørskov JK. Insights into the hydrogen evolution reaction on 2D transition-metal dichalcogenides. J Phys Chem C. 2022;126(11):5151.
91. Jaramillo TF, Jorgensen KP, Bonde J, Nielsen JH, Horch S, Chorkendorff I. Identification of active edge sites for electrochemical H_2 evolution from MoS_2 nanocatalysts. Science. 2007;317(5834):100.
92. Kang Y, Gong Y, Hu Z, Li Z, Qiu Z. Plasmonic hot electron enhanced MoS_2 photocatalysis in hydrogen evolution. Nanoscale. 2015;7(10):4482.
93. Eftekhari A. Molybdenum diselenide ($MoSe_2$) for energy storage, catalysis, and optoelectronics. Appl Mater Today. 2017;8:1.
94. Li H, Wu J, Yin Z, Zhang H. Preparation and applications of mechanically exfoliated single-layer and multilayer MoS and WSe nanosheets. Acc Chem Res. 2014;47(04):1067.
95. Sang Y, Zhao Z, Zhao M, Hao P, Leng Y, Liu H. From UV to near-infrared, WS_2 nanosheet: a novel photocatalyst for full solar light spectrum photodegradation. Adv Mater. 2015;27(2):363.
96. Manzeli S, Ovchinnikov D, Pasquier D, Yazyev OV, Kis A. 2D transition metal dichalcogenides. Nat Rev Mater. 2017;2(8):17033.
97. Wang Q, Domen K. Particulate photocatalysts for light-driven water splitting: mechanisms, challenges, and design strategies. Chem Rev. 2020;120(2):919.
98. Yang RJ, Mei L, Zhang QY, Fan YY, Shin HS, Voiry D, Zeng ZY. High-yield production of mono- or few-layer transition metal dichalcogenide nanosheets by an electrochemical lithium ion intercalation-based exfoliation method. Nat Protoc. 2022;17(2):358.
99. Rong JS, Ye YP, Cao J, Liu XY, Fan HG, Yang S, Wei MB, Yang LL, Yang JH, Chen YL. Restructuring electronic structure via W doped 1T MoS_2 for enhancing hydrogen evolution reaction. Appl Surf Sci. 2022;579:152216.
100. Shi SP, Gao DQ, Xia BR, Liu PT, Xue DS. Enhanced hydrogen evolution catalysis in MoS_2 nanosheets by incorporation of a metal phase. J Mater Chem A. 2015;3(48):24414.
101. Jia W, Wang X, Lu ZJ, Wu YF, Sheng R, Lv J. Hydrazine hydrate-assisted adjustment of sulfur-rich MoS_2 as hydrogen evolution electrocatalyst. J Alloys Compd. 2021;885:160990.
102. Samadi M, Sarikhani N, Zirak M, Hua Z, Zhang HL, Moshfegh AZ. Group 6 transition metal dichalcogenide nanomaterials: synthesis, applications and future perspectives. Nanoscale Horiz. 2018;3(02):90.
103. Parzinger E, Miller B, Blaschke B, Garrido JA, Ager JW, Holleitner A, Wurstbauer U. Photocatalytic stability of single- and few-layer MoS_2. ACS Nano. 2015;9(11):11302.
104. Shao MM, Shao YF, Ding SJ, Tong R, Zhong XW, Yao LM, Ip WF, Xu BM, Shi XQ, Sun YY, Wang XS, Pan H. Carbonized MoS_2: super-active co-catalyst for highly efficient water splitting on CdS. ACS Sustainable Chem Eng. 2019;7(4):4220.
105. Shah SA, Khan I, Yuan AH. MoS_2 as a co-catalyst for photocatalytic hydrogen production: a mini review. Molecules. 2022;27(10):3289.
106. Li W, Wang L, Zhang Q, Chen Z, Sun M. Fabrication of an ultrathin 2D/2D C_3N_4/MoS_2 heterojunction photocatalyst with enhanced photocatalytic performance. J Alloys Compd. 2019;808:151681.

107. Kou S, Guo X, Xu X, Yang J. TiO_2 on $MoSe_2$ nanosheets as an advanced photocatalyst for hydrogen evolution in visible light. Catal Commun. 2018;106:60.
108. Zhang BQ, Chen JS, Niu HL, Mao CJ, Song JM. Synthesis of ultrathin WSe_2 nanosheets and their high-performance catalysis for conversion of amines to imines. Nanoscale. 2018;10(43):20266.
109. Wang XC, Maeda K, Thomas A, Takanabe K, Xin G, Carlsson JM, Domen K, Antonietti M. A metal-free polymeric photocatalyst for hydrogen production from water under visible light. Nat Mater. 2009;8(1):76.
110. Dong F, Li YH, Wang ZY, Ho WK. Enhanced visible light photocatalytic activity and oxidation ability of porous graphene-like g-C_3N_4 nanosheets via thermal exfoliation. Appl Surf Sci. 2015;358:393.
111. Feng J, Chen TT, Liu SN, Zhou QH, Ren YM, Lv YZ, Fan ZJ. Improvement of g-C_3N_4 photocatalytic properties using the Hummers method. J Colloid Interface Sci. 2016;479:1.
112. Xing YP, Wang XK, Hao SH, Zhang XL, Wang X, Ma WX, Zhao G, Xu XJ. Recent advances in the improvement of g-C_3N_4 based photocatalytic materials. Chin Chem Lett. 2021;32(1):13.
113. Liu YM, Wang JP, Yang P. Photochemical reactions of g-C_3N_4-based heterostructured composites in Rhodamine B degradation under visible light. RSC Adv. 2016;6(41):34334.
114. Peng DL, Wang HH, Yu K, Chang Y, Ma XG, Dong SJ. Photochemical preparation of the ternary composite CdS/Au/g-C_3N_4 with enhanced visible light photocatalytic performance and its microstructure. RSC Adv. 2016;6(81):77760.
115. Zhang W, Zhang Z, Kwon S, Zhang F, Stephen B, Kim KK, Jung R, Kwon S, Chung KB, Yang W. Photocatalytic improvement of Mn-adsorbed g-C_3N_4. Appl Catal B Environ. 2017;206:271.
116. Cao J, Pan C, Ding YB, Li WJ, Lv KL, Tang HQ. Constructing nitrogen vacancy introduced g-C_3N_4 p-n homojunction for enhanced photocatalytic activity. J Environ Chem Eng. 2019;7(2):102984.
117. Wang SC, Wang X, Liu BY, Xiao X, Wang LZ, Huang W. Boosting the photocatalytic hydrogen production performance of graphitic carbon nitride nanosheets by tailoring the cyano groups. J Colloid Interface Sci. 2022;610:495.
118. Bridgman PW. Two new modifications of phosphorus. JACS. 1914;36(7):1344.
119. Lange S, Schmidt P, Nilges T. Au_3SnP_7@black phosphorus: an easy access to black phosphorus. Inorg Chem. 2007;46(10):4028.
120. Xing C, Zhang JH, Jing JY, Li JZ, Shi F. Preparations, properties and applications of low-dimensional black phosphorus. Chem Eng J. 2019;370:120.
121. Lee HU, Lee SC, Won JG, Son BC, Choi SH, Kim YS, Park SY, Kim HS, Lee YC, Lee J. Stable semiconductor black phosphorus (BP)@titanium dioxide (TiO_2) hybrid photocatalysts. Sci Rep. 2015;5(1):8691.
122. Zhu MS, Cai XY, Fujitsuka M, Zhang JY, Majima T. Au/$La_2Ti_2O_7$ nanostructures sensitized with black phosphorus for plasmon-enhanced photocatalytic hydrogen production in visible and near-infrared light. Angew Chem Int Ed. 2017;56(8):2064.
123. Zhou SH, Bao CH, Fan BS, Zhou H, Gao QX, Zhong HY, Lin TY, Liu H, Yu P, Tang PZ, Meng S, Duan WH, Zhou SY. Pseudospin-selective Floquet band engineering in black phosphorus. Nature. 2023;614(7946):75.
124. Favron A, Gaufrès E, Fossard F, Phaneuf LHAL, Tang NYW, Lévesque PL, Loiseau A, Leonelli R, Francoeur S, Martel R. Photooxidation and quantum confinement effects in exfoliated black phosphorus. Nat Mater. 2015;14(8):826.
125. Zhu XJ, Zhang TM, Sun ZJ, Chen HL, Guan J, Chen X, Ji HX, Du PW, Yang SF. Black phosphorus revisited: a missing metal-free elemental photocatalyst for visible light hydrogen evolution. Adv Mater. 2017;29(17):1605776.
126. Velický M, Toth PS. From two-dimensional materials to their heterostructures: an electrochemist's perspective. Appl Mater Today. 2017;8:68.
127. Fan FR, Wang RX, Zhang H, Wu WZ. Emerging beyond-graphene elemental 2D materials for energy and catalysis applications. Chem Soc Rev. 2021;50(19):10983.
128. Yu X, Fautrelle Y, Ren ZM, Li X. PVA-assisted synthesis and characterization of core shell Bi nanobelts. Mater Lett. 2015;161:144.
129. Yang QQ, Liu RT, Huang C, Huang YF, Gao LF, Sun B, Huang ZP, Zhang L, Hu CX, Zhang ZQ, Sun CL, Wang Q, Tang YL, Zhang HL. 2D bismuthene fabricated via acid-intercalated exfoliation showing strong nonlinear near-infrared responses for mode-locking lasers. Nanoscale. 2018;10(45):21106.
130. Hussain N, Liang TX, Zhang QY, Anwar T, Huang Y, Lang JL, Huang K, Wu H. Ultrathin Bi nanosheets with superior photoluminescence. Small. 2017;13(36):1701349.
131. Sun Y, Yuan JJ, Xin Y, Liu GW, Zhang F, Xing F, Fu SG. Broadband saturated absorption properties of bismuthene nanosheets. RSC Adv. 2021;11(55):35046.
132. Hu E, Yao Y, Cui Y, Qian G. Strategies for the enhanced water splitting activity over metal–organic frameworks-based electrocatalysts and photocatalysts. Mater Today Nano. 2021;15(38):100124.
133. Zhao HN, Xing ZP, Su SY, Song SJ, Xu TF, Li ZZ, Zhou W. Recent advances in metal organic frame photocatalysts for environment and energy applications. Appl Mater Today. 2020;21:15.
134. Zou ZH, Wang JL, Pan HR, Li J, Guo KL, Zhao YQ, Xu CL. Enhanced oxygen evolution reaction of defective CoP/MOF-integrated electrocatalyst by partial phosphating. J Mater Chem A. 2020;8(28):14099.
135. Degaga GD, Pandey R, Gupta C, Bharadwaj L. Tailoring of the electronic property of Zn-BTC metal-organic framework via ligand functionalization: an ab initio investigation. RSC Adv. 2019;9(25):14260.
136. Nguyen HL. Metal-organic frameworks can photocatalytically split water-why not? Adv Mater. 2022;34(20):5.
137. Tran NT, Trung LG, Nguyen MK. The degradation of organic dye contaminants in wastewater and solution from highly visible light responsive ZIF-67 monodisperse photocatalyst. J Solid State Chem. 2021;300:8.
138. Peng HJ, Zhu L, Wang YL, Chao HY, Jiang L, Qiao ZP. CdS/ZIF-67 nanocomposites with enhanced performance for visible light CO_2 photoreduction ocr. Inorg Chem Commun. 2020;117:5.
139. Qiu JH, Yang LY, Li M, Yao JF. Metal nanoparticles decorated MIL-125-NH_2 and MIL-125 for efficient photocatalysis. Mater Res Bull. 2019;112:297.
140. Yue K, Zhang XD, Jiang ST, Chen JF, Yang Y, Bi FK, Wang YX. Recent advances in strategies to modify MIL-125 (Ti) and its environmental applications. J Mol Liq. 2021;335:116108.
141. Xu ML, Li DD, Sun K, Jiao L, Xie CF, Ding CM, Jiang HL. Interfacial microenvironment modulation boosting electron transfer between metal nanoparticles and MOFs for enhanced photocatalysis. Angew Chem Int Ed. 2021;60(30):16372.
142. Qi XM, Wu Q, Wang XJ, Li KX, Liu C, Li SJ. Design of UiO-66@$BiOIO_3$ heterostructural composites with remarkable boosted photocatalytic activities in removing diverse industrial pollutants. J Phys Chem Solids. 2021;151:109903.
143. Dong JQ, Han X, Liu Y, Li HY, Cui Y. Metal-covalent organic frameworks (MCOFs): a bridge between metal-organic frameworks and covalent organic frameworks. Angew Chem Int Ed. 2020;59(33):13722.

144. Geng KY, He T, Liu RY, Dalapati S, Tan KT, Li ZP, Tao SS, Gong YF, Jiang QH, Jiang DL. Covalent organic frameworks: design, synthesis, and functions. Chem Rev. 2020;120(16):8814.
145. Fuerte D, Valverde GA, Pintado SM, Díaz U, Sánchez F, Maya EM, Iglesias M. Phenyl extended naphthalene-based covalent triazine frameworks as versatile metal-free heterogeneous photocatalysts. Solar Rrl. 2022;6(2):2100848.
146. Tan L, Wang ZL, Zhao ZF, Song YF. Recent progress on nanostructured layered double hydroxides for visible-light-induced photoreduction of CO_2. Chem Asian J. 2020;15(21):3380.
147. Lv L, Yang ZX, Chen K, Wang CD, Xiong YJ. 2D layered double hydroxides for oxygen evolution reaction: from fundamental design to application. Adv Energy Mater. 2019;9(17):29.
148. Vincente R. Layered double hydroxides: present and future. New York: Nova Science Publishers; 2001. p.115.
149. Xu ZP, Lu GQ. Hydrothermal synthesis of layered double hydroxides (LDHs) from mixed MgO and Al_2O_3: LDH formation mechanism. Chem Mater. 2005;17(5):1055.
150. Cermelj K, Ruengkajorn K, Buffet JC, O'Hare D. Layered double hydroxide nanosheets via solvothermal delamination. J Energy Chem. 2019;35:88.
151. Lu XY, Xue HR, Gong H, Bai MJ, Tang DM, Ma RZ, Sasaki T. 2D layered double hydroxide nanosheets and their derivatives toward efficient oxygen evolution reaction. Nano Micro Lett. 2020;12(1):32.
152. Li C, Jing HH, Wu Z, Jiang DH. Layered double hydroxides for photo(electro)catalytic applications: a mini review. Nanomaterials. 2022;12(19):3525.
153. Starukh G. Photocatalytically enhanced cationic dye removal with Zn-Al layered double hydroxides. Nanoscale Res Lett. 2017;12(1):1.
154. Su SD, Li XM, Tan MY, Zhang X, Wang YY, Duan YZ, Peng J, Luo M. Enhancement of the properties of ZnAl-LDHs for photocatalytic nitrogen reduction reaction by controlling anion intercalation. Inorg Chem Front. 2023;10(3):869.
155. Naguib M, Kurtoglu M, Presser V, Lu J, Niu JJ, Heon M, Hultman L, Gogotsi Y, Barsoum M W. Two-dimensional nanocrystals produced by exfoliation of Ti_3AlC_2. Adv. Mater. 2011;23(37):4248.
156. Pang JB, Mendes RG, Bachmatiuk A, Zhao L, Ta HQ, Gemming T, Liu H, Liu ZF, Rummeli MH. Applications of 2D MXenes in energy conversion and storage systems. Chem Soc Rev. 2019;48(1):72.
157. Allen PK, Straka W, Keith D, Han SB, Reynolds L, Gautam B, Autrey DE. Tuning the magnetic properties of two-dimensional MXenes by chemical etching. Materials. 2021;14(3):9.
158. Natu V, Pai R, Sokol M, Carey M, Kalra V, Barsoum MW. 2D $Ti_3C_2T_z$ MXene synthesized by water-free etching of Ti_3AlC_2 in polar organic solvents. Chem. 2020;6(3):616.
159. Yang YN, Cao ZR, Shi LJ, Wang RR, Sun J. Enhancing the conductivity, stability and flexibility of $Ti_3C_2T_x$ MXenes by regulating etching conditions. Appl Surf Sci. 2020;533:147475.
160. Naguib M, Kurtoglu M, Presser V, Lu J, Niu JJ, Heon M, Hultman L, Gogotsi Y, Barsoum MW. Two-dimensional nanocrystals produced by exfoliation of Ti_3AlC_2. Adv Mater. 2011;23(37):4248.
161. Qin R, Shan G, Hu M, Huang W. Two-dimensional transition metal carbides and/or nitrides (MXenes) and their applications in sensors. Mater Today Phys. 2021;21:100527.
162. Khazaei M, Arai M, Sasaki T, Chung CY, Venkataramanan NS, Estili M, Sakka Y, Kawazoe Y. Novel electronic and magnetic properties of two-dimensional transition metal carbides and nitrides. Adv Funct Mater. 2013;23(17):2185.
163. Ghosh K, Ghosh J, Giri PK. Accordion-like multilayered two-dimensional $Ti_3C_2T_x$ MXenes for catalytic elimination of organic dyes from wastewater via the fenton reaction. ACS Appl Nano Mater. 2022;5(11):16451.
164. Wei Y, Zhang P, Soomro RA, Zhu QZ, Xu B. Advances in the synthesis of 2D MXenes. Adv Mater. 2021;33(39):30.
165. Firouzjaei MD, Karimiziarani M, Moradkhani H, Elliott M, Anasori B. MXenes: the two-dimensional influencers. Mater Today Adv. 2022;13:100202.
166. Chen L, Ye XY, Chen S, Ma L, Wang ZP, Wang QT, Hua NB, Xiao XQ, Cai SG, Liu XH. Ti_3C_2 MXene nanosheet/TiO_2 composites for efficient visible light photocatalytic activity. Ceram Int. 2020;46(16):25895.
167. Liu ZY, Zhou YH, Yang LJ, Yang RC. Green preparation of in-situ oxidized TiO_2/Ti_3C_2 heterostructure for photocatalytic hydrogen production. Adv Powder Technol. 2021;32(12):4857.
168. Zhuang Y, Liu YF, Meng XF. Fabrication of TiO_2 nanofibers/MXene Ti_3C_2 nanocomposites for photocatalytic H_2 evolution by electrostatic self-assembly. Appl Surf Sci. 2019;496:143647.
169. Zuo G, Wang Y, Wei LT, Xie A, Zhao Y. Enhanced photocatalytic water oxidation by hierarchical 2D-Bi_2MoO_6@2D-MXene schottky junction nanohybrid. Chem Eng J. 2020;403:126328.
170. Liu WZ, Sun MX, Ding ZP, Gao BW, Ding W. Ti_3C_2 MXene embellished g-C_3N_4 nanosheets for improving photocatalytic redox capacity. J Alloys Compd. 2021;877:160223.
171. Yan H, Wang XD, Yao M, Yao XJ. Band structure design of semiconductors for enhanced photocatalytic activity: the case of TiO_2. Prog Nat Sci. 2013;23(4):402.
172. Xiao M, Wang ZL, Lyu MQ, Luo B, Wang SC, Liu G, Cheng HM, Wang LZ. Hollow nanostructures for photocatalysis: advantages and challenges. Adv Mater. 2019;31(38):23.
173. Wang DA, Hisatomi T, Takata T, Pan CS, Katayama M, Kubota J, Domen K. Core/shell photocatalyst with spatially separated co-catalysts for efficient reduction and oxidation of water. Angew Chem Int Ed. 2013;52(43):11252.
174. Sun YJ, Xiong T, Dong F, Huang HW, Cen WL. Interlayer-I-doped $BiOIO_3$ nanoplates with an optimized electronic structure for efficient visible light photocatalysis. Chem Commun. 2016;52(53):8243.
175. Gou ZQ, Dai JH, Bai JW. Synthesis of mesoporous Bi_2WO_6 flower-like spheres with photocatalysis properties under visible light. Int J Electrochem Sci. 2020;15(11):10684.
176. Xie H, Le Y. Synthesis of 2D-ordered spherical ZnO films for photocatalysis. Mater Technol. 2020;35(9–10):642.
177. Lu M, Liu M, Wei Y, Xie H, Fan W, Huang J, Hu J, Wei P, Zhang W, Xie Y, Qi Y. Photocatalytic activity and mechanism of cerium dioxide with different morphologies for tetracycline degradation. J Alloys Compd. 2023;936:168273.
178. Liu C, Qin Y, Guo W, Shi YZ, Wang ZW, Yu Y, Wu L. Visible-light-driven photocatalysis over nano-TiO_2 with different morphologies: from morphology through active site to photocatalytic performance. Appl Surf Sci. 2022;580:152262.
179. Sun YF, Gao S, Lei FC, Xie Y. Atomically-thin two-dimensional sheets for understanding active sites in catalysis. Chem Soc Rev. 2015;44(3):623.
180. Du J, Li S, Du Z, Meng S, Li B. Boron/oxygen-codoped graphitic carbon nitride nanomesh for efficient photocatalytic hydrogen evolution. Chem Eng J. 2020;407(9):127114.
181. Liu J, Zhang S, Zhao H. Fabricating visible-light photoactive 3D flower-like BiOCl nanostructures via a one-step solution chemistry method at room temperature. Appl Surf Sci. 2019;479(15):247.
182. Li DX, Masters P, Maschmeyer PT. Photocatalytic hydrogen evolution from silica-templated polymeric graphitic carbon nitride–is the surface area important? ChemCatChem. 2015;7(01):121.

183. Chen SL, Xiong F, Huang WX. Surface chemistry and catalysis of oxide model catalysts from single crystals to nanocrystals. Surf Sci Rep. 2019;74(4):100.
184. Yang HG, Sun CH, Qiao SZ, Zou J, Liu G, Smith SC, Cheng HM, Lu GQ. Anatase TiO_2 single crystals with a large percentage of reactive facets. Nature. 2008;453(7195):638.
185. Li DW, Yu SY, Geng HJ, Zhou W, Mu DD, Liu ST. The (002) exposing facets of WO_3 boosting photocatalytic degradation of nitrobenzene. Appl Surf Sci. 2023;607:154996.
186. Hu WH, Han GQ, Dai FN, Liu YR, Shang X, Dong B, Chai YM, Liu YQ, Liu CG. Effect of pH on the growth of MoS_2 (002) plane and electrocatalytic activity for HER. Int J Hydrog Energy. 2016;41(1):294.
187. Dang YY, Luo L, Wang W, Hu WF, Wen X, Lin KY, Ma BJ. Improving the photocatalytic H_2 evolution of CdS by adjusting the (002) crystal facet. J Phys Chem C. 2022;126(3):1346.
188. Guan M, Xiao C, Zhang J, Fan S, An R, Cheng Q, Xie J, Zhou M, Ye B, Xie Y. Vacancy associates promoting solar-driven photocatalytic activity of ultrathin bismuth oxychloride nanosheets. JACS. 2013;135(28):10411.
189. Li LY, Xia YB, Zeng MQ, Fu L. Facet engineering of ultrathin two-dimensional materials. Chem Soc Rev. 2022;51(17):7327.
190. Parangi T, Mishra MK. Titania nanoparticles as modified photocatalysts: a review on design and development. Comments Inorg Chem. 2019;39(2):90.
191. Lukowski MA, Daniel AS, Meng F, Forticaux A, Li LS, Jin S. Enhanced hydrogen evolution catalysis from chemically exfoliated metallic MoS_2 nanosheets. JACS. 2013;135(28):10274.
192. Li MY, Zhou ZZ, Hu L, Wang SY, Zhou YZ, Zhu RB, Chu XZ, Vinu A, Wan T, Cazorla C, Yi JB, Chu DW. Hydrazine hydrate intercalated 1T-dominant MoS_2 with superior ambient stability for highly efficient electrocatalytic applications. ACS Appl Mater Interfaces. 2022;14(14):16338.
193. Liu YP, Li YH, Peng F, Lin Y, Yang SY, Zhang SS, Wang HJ, Cao YH, Yu H. 2H-and 1T-mixed phase few-layer MoS_2 as a superior to Pt co-catalyst coated on TiO_2 nanorod arrays for photocatalytic hydrogen evolution. Appl Catal B Environ. 2019;241:236.
194. Huang SQ, Xu YG, Ge FY, Tian D, Zhu XW, Xie M, Xu H, Li HM. Tailoring of crystalline structure of carbon nitride for superior photocatalytic hydrogen evolution. J Colloid Interface Sci. 2019;556:324.
195. Meng AY, Teng ZY, Zhang QT, Su CL. Intrinsic defects in polymeric carbon nitride for photocatalysis applications. Chem Asian J. 2020;15(21):3405.
196. Di J, Xiong J, Li HM, Liu Z. Ultrathin 2D photocatalysts: electronic-structure tailoring, hybridization, and applications. Adv Mater. 2018;30(1):1704548.
197. Rohj RK, Hossain A, Mahadevan P, Sarma DD. Band gap reduction in ferroelectric $BaTiO_3$ through heterovalent Cu-Te Co-doping for visible-light photocatalysis. Front Chem. 2021;9:682979.
198. Shao W, Wang H, Zhang XD. Elemental doping for optimizing photocatalysis in semiconductors. Dalton Trans. 2018;47(36):12642.
199. Su R, Bechstein R, Kibsgaard J, Vang RT, Besenbacher F. High-quality Fe-doped TiO_2 films with superior visible-light performance. J Mater Chem A. 2012;22(45):23755.
200. Li JX, Wang DD, Guan RQ, Zhang YJ, Zhao Z, Zhai HJ, Sun ZC. Vacancy-enabled mesoporous TiO_2 modulated by nickel doping with enhanced photocatalytic nitrogen fixation performance. ACS Sustain Chem Eng. 2020;8(49):18258.
201. Li ZJ, Li SY, Davis AH, Hofman E, Leem G, Zheng WW. Enhanced singlet oxygen generation by hybrid Mn-doped nanocomposites for selective photo-oxidation of benzylic alcohols. Nano Res. 2020;13(6):1668.
202. Ishaq T, Yousaf M, Bhatti IA, Ahmad M, Ikram M, Khan MU, Qayyum A. Photo-assisted splitting of water into hydrogen using visible-light activated silver doped g-C_3N_4 & CNTs hybrids. Int J Hydrog Energy. 2020;45(56):31574.
203. Humayun M, Fu QY, Zheng ZP, Li HL, Luo W. Improved visible-light catalytic activities of novel Au/P-doped g-C_3N_4 photocatalyst for solar fuel production and mechanism. Appl Catal A Gen. 2018;568:139.
204. Luo H, Liu Y, Dimitrov SD, Steier L, Guo SH, Li XH, Feng JY, Xie F, Fang YX, Sapelkin A, Wang XC, Titirici MM. Pt single-atoms supported on nitrogen-doped carbon dots for highly efficient photocatalytic hydrogen generation. J Mater Chem A. 2020;8(29):14690.
205. Tonda S, Kumar S, Kandula S, Shanker V. Fe-doped and -mediated graphitic carbon nitride nanosheets for enhanced photocatalytic performance under natural sunlight. J Mater Chem A. 2014;2(19):6772.
206. Shah JH, Shahid A, Idris AM, Rasheed S, Li C. Intrinsic photocatalytic water oxidation activity of Mn-doped ferroelectric $BiFeO_3$. Chinese J Catal. 2021;42(6):945.
207. Qin J, Huo J, Zhang P, Jian Z, Wang T, Zeng H. Improving the photocatalytic hydrogen production of Ag/g-C_3N_4 nanocomposites by dye-sensitization under visible light irradiation. Nanoscale. 2016;8(4):2249.
208. Liu W, Zhao Y, Li H, Liu X, Liu W. Ag deposition on N and B co-doped TiO_2 nanoparticles: an avenue for high-efficiency photocatalytic degradation of dye and hydrocarbons in oil-contaminated wastewater. NANO. 2021;16(4):2150042.
209. Wang K, Li Q, Liu BS, Cheng B, Ho WK, Yu JG. Sulfur-doped g-C_3N_4 with enhanced photocatalytic CO_2-reduction performance. Appl Catal B Environ. 2015;176:44.
210. Kong JZ, Zhai HF, Zhang W, Wang SS, Zhao XR, Li M, Li H, Li AD, Wu D. Visible light-driven photocatalytic performance of N-Doped ZnO/g-C_3N_4 nanocomposites. Nanoscale Res Lett. 2017;12(1):526.
211. Wang DX, Wang S, Li BH, Zhang ZH, Zhang QJ. Tunable band gap of N-V co-doped Ca:TiO_2-B ($CaTi_5O_{11}$) for visible-light photocatalysis. Int J Hydrog Energy. 2019;44(10):4716.
212. Wang W, Tade MO, Shao ZP. Nitrogen-doped simple and complex oxides for photocatalysis: a review. Prog Mater Sci. 2018;92:33.
213. Basavad M, Shokrollahi H, Golkari M. Effect of thermal cycle and Bi/Eu doping on the solubility of Ce in YIG. Ceram Int. 2020;46(12):20144.
214. Li R, Chen TT, Lu JW, Hu HL, Zheng H, Zhu PF, Pan XL. Metal-organic frameworks doped with metal ions for efficient sterilization: enhanced photocatalytic activity and photothermal effect. Water Res. 2023;229:119366.
215. Li YY, Liu QF, Cui QN, Qi ZM, Wu JZ, Zhao H. Effects of rhenium dopants on photocarrier dynamics and optical properties of monolayer, few-layer, and bulk MoS_2. Nanoscale. 2017;9(48):19360.
216. Madeo J, Man MKL, Sahoo C, Campbell M, Pareek V, Wong EL, Al-Mahboob A, Chan NS, Karmakar A, Mariserla BMK, Li XQ, Heinz TF, Cao T, Dani KM. Directly visualizing the momentum-forbidden dark excitons and their dynamics in atomically thin semiconductors. Science. 2020;370(6521):1199.
217. Hu HH, Qian DG, Lin P, Ding ZX, Cui C. Oxygen vacancies mediated in-situ growth of noble-metal (Ag, Au, Pt) nanoparticles on 3D TiO_2 hierarchical spheres for efficient photocatalytic hydrogen evolution from water splitting. Int J Hydrog Energy. 2020;45(1):629.
218. Zheng XN, Li Y, Yang J, Cui SH. Z-Scheme heterojunction Ag/NH_2-MIL-125(Ti)/CdS with enhanced photocatalytic activity

for ketoprofen degradation: mechanism and intermediates. Chem Eng J. 2021;422:12.
219. Qiu JJ, Wei WD. Surface plasmon-mediated photothermal chemistry. J Phys Chem C. 2014;118(36):20735.
220. Zhang P, Wang T, Gong JL. Mechanistic understanding of the plasmonic enhancement for solar water splitting. Adv Mater. 2015;27(36):5328.
221. Fang L, Nan F, Yang Y, Cao D. Enhanced photoelectrochemical and photocatalytic activity in visible-light-driven Ag/$BiVO_4$ inverse opals. Appl Phys Lett. 2016;108(9): 093902.
222. Shi WY, Song YY, Zhang XL, Duan D, Wang HY, Sun ZB. Nanoporous Pt/TiO_2 nanocomposites with greatly enhanced photocatalytic performance. JCCS. 2018;65(11):1286.
223. Shi Y, Li L, Xu Z, Guo F, Li Y, Shi W. Synergistic coupling of piezoelectric and plasmonic effects regulates the Schottky barrier in Ag nanoparticles/ultrathin g-C_3N_4 nanosheets heterostructure to enhance the photocatalytic activity. Appl Surf Sci. 2023;616:156466.
224. Cui XF, Zhou Y, Wu J, Ling S, Zhao LJ, Zhang JL, Wang JW, Qin W, Zhang YG. Controlling Pt co-catalyst loading in a WO_3 quantum dot and MoS_2 nanosheet composite Z-scheme system for enhanced photocatalytic H_2 evolution. Nanotechnology. 2020;31(18):185701.
225. Gao C, Wang J, Xu HX, Xiong YJ. Coordination chemistry in the design of heterogeneous photocatalysts. Chem Soc Rev. 2017;46(10):2799.
226. Huang L, Liu X, Wu HC, Wang XL, Wu HM, Li RG, Shi LY, Li C. Surface state modulation for size-controllable photodeposition of noble metal nanoparticles on semiconductors. J Mater Chem A. 2020;8(40):21094.
227. Zhang FF, Zhu YL, Lin Q, Zhang L, Zhang XW, Wang HT. Noble-metal single-atoms in thermocatalysis, electrocatalysis, and photocatalysis. Energy Environ Sci. 2021;14(5):2954.
228. Moniz SJA, Shevlin SA, Martin DJ, Guo ZX, Tang JW. Visible-light driven heterojunction photocatalysts for water splitting: a critical review. Energy Environ Sci. 2015;8(3):731.
229. Liu Y, Weiss NO, Duan XD, Cheng HC, Huang Y, Duan XF. Van der Waals heterostructures and devices. Nat Rev Mater. 2016;1(9):17.
230. Jariwala D, Marks TJ, Hersam MC. Mixed-dimensional van der Waals heterostructures. Nat Mater. 2017;16(2):170.
231. Liu Q, Chen T, Guo Y, Zhang Z, Fang X. Ultrathin g-C_3N_4 nanosheets coupled with carbon nanodots as 2D/0D composites for efficient photocatalytic H_2 evolution. Appl Catal B Environ. 2016;193:248.
232. Li YK, Zhang P, Wan DY, Xue C, Zhao JT, Shao GS. Direct evidence of 2D/1D heterojunction enhancement on photocatalytic activity through assembling MoS_2 nanosheets onto super-long TiO_2 nanofibers. Appl Surf Sci. 2020;504:144361.
233. Fu J, Xu Q, Low J, Jiang C, Yu J. Ultrathin 2D/2D WO_3/g-C_3N_4 step-scheme H_2 production photocatalyst. Appl Catal B Environ. 2019;243:556.
234. Chen YL, Su FY, Xie HQ, Wang RP, Ding CH, Huang JD, Xu X, Ye LQ. One-step construction of S-scheme heterojunctions of N-doped MoS_2 and S-doped g-C_3N_4 for enhanced photocatalytic hydrogen evolution. Chem Eng J. 2021;404:126498.
235. Ping N, Zhang L, Gang L, Cheng H. Graphene-like carbon nitride nanosheets for improved photocatalytic activities. Adv Funct Mater. 2012;22(22):4763.
236. Song XH, Wang M, Liu WT, Li X, Zhu Z, Huo PW, Yan YS. Thickness regulation of graphitic carbon nitride and its influence on the photocatalytic performance towards CO_2 reduction. Appl Surf Sci. 2022;577:151810.
237. Bie CB, Fu JW, Cheng B, Zhang LY. Ultrathin CdS nanosheets with tunable thickness and efficient photocatalytic hydrogen generation. Appl Surf Sci. 2018;462:606.
238. Jin Y, Yu K. A review of optics-based methods for thickness and surface characterization of two-dimensional materials. J Phys D. 2021;54(39):393001.
239. Wang Q, Liu ZQ, Liu DM, Wang W, Zhao ZW, Cui FY, Li GB. Oxygen vacancy-rich ultrathin sulfur-doped bismuth oxybromide nanosheet as a highly efficient visible-light responsive photocatalyst for environmental remediation. Chem Eng J. 2019;360:838.
240. Niu P, Qiao M, Li Y, Huang L, Zhai T. Distinctive defects engineering in graphitic carbon nitride for greatly extended visible light photocatalytic hydrogen evolution. Nano Energy. 2017;44:73.
241. Salavati-fard T, Wang B. Significant role of oxygen dopants in photocatalytic PFCA degradation over h-BN. ACS Appl Mater Interfaces. 2021;13(39):46727.
242. Wang ZJ, Jin ZL, Wang GR, Ma BZ. Efficient hydrogen production over MOFs (ZIF-67) and g-C_3N_4 boosted with MoS_2 nanoparticles. Int J Hydrog Energy. 2018;43(29):13039.
243. Li Q, Fan L, Zhang LH, Li Y, Chen CX, Zhao RT, Zhu W. Boosting and tuning the visible photocatalytic degradation performances towards reactive blue 21 via dyes@MOF composites. J Solid State Chem. 2019;269:465.
244. Li SM, Wu F, Lin RB, Wang J, Li CX, Li ZQ, Jiang J, Xiong YJ. Enabling photocatalytic hydrogen production over Fe-based MOFs by refining band structure with dye sensitization. Chem Eng J. 2022;429:132217.
245. Wei S, Fan S, Zhang M, Ren J, Jia B, Wang Y, Wu R, Fang Z, Liang Q. Dye-sensitized Bi_2MoO_6 for highly efficient photocatalytic degradation of levofloxacin under LED light irradiation. Mater Today Sustain. 2023;21:100311.